NTNU

Norwegian University of
Science and Technology

Multiscale Modelling of Elastic Parameters

Kari Børset

Master of Science in Physics and Mathematics
Submission date: May 2008
Supervisor: Helge Holden, MATH

Norwegian University of Science and Technology
Department of Mathematical Sciences

Problem Description

In modelling the behaviour of physical parameters in the vicinity of a borehole, many new tools and workflows must be developed. StatoilHydro Research Centre Trondheim develops workflows integrating knowledge on the cm-scale from geology into the mathematical modelling of subsurface properties.

This results in complex geometries that are representative for the observed geology in the sub surface, on which mathematical models for physical parameters must be applied. StatoilHydro has developed a code for upscaling elastic moduli, making it possible for the first time to be able to quantify geometric and other effects from small scale geology. The code itself is not limited to any scale, and can be integrated into numerous other workflows.

Challenges to be solved in this work includes integrating knowledge in rock mechanics and reservoir engineering. The mathematical similarities between elasticity and permeability will be pursued. The upscaling procedure will yield a 21-element general elasticity tensor, for which workflows need to be developed to ensure applicability. There is a need of comparing the general elasticity tensors to tensors with 5 degrees of freedom arising from existing Backus upscaling, which is basically the only previous tool available for elasticity upscaling. Voigt and Reuss bonds are analogs to harmonic and geometric means in permeability upscaling, and a comparison with those upscaling procedures will similary be pursued.

Assignment given: 14. January 2008
Supervisor: Helge Holden, MATH

Preface

This master's thesis is the result of my work for Master of Science in Industrial Mathematics, TMA4910, at the Norwegian University of Science and Technology. My formal supervisor at the Department of Mathematical Sciences has been Prof. Helge Holden.

I was introduced to the upscaling topic during summer 2007 when I had a summer job at StatoilHydro's Research Centre at Rotvoll, Trondheim. In my specialization project, which was also done here, I dealt with upscaling too, more precisely permeability upscaling. Even though this thesis is not a direct continuation of the specialization project, I have undoubedly benefited from working with a similar topic before, especially when it comes to the background theory.

To my knowledge, elasticity upscaling which incorporate fine scale geology has not been done earlier. Therefore it has been difficult to find published data to compare with the results I have obtained and also to know which effects to look for. Furthermore, due to the limited access to previous work on the topic, at no point during the work did I know exactly what would be the outcome of this thesis. This is also why the thesis have several different "branches" without an obvious governing idea.

The work is carried out at StatoilHydro's Research Centre at Rotvoll, Trondheim under guidance of Håvard Berland and Alf Birger Rustad. I would like to thank Håvard for his cooperative way of helping me both in finding the path for my work and to discuss problems when I got stuck. I thank Alf for benevolently explaining topics related to both upscaling and rock physics even though I know he really did not have time. I would also like to thank everyone else at Rotvoll who have assisted in some way, either by answering any of my questions, discussed complicated topics or provided data and articles, especially Kjetil Nordahl who has supplied many of the models and the data I have used.

Trondheim, May 2008 Kari Børset

Abstract

Petrophysical properties in general and elasticity in particular have heterogeneous variations over many length scales. In a reservoir model, on which one for example can simulate fluid flow, seismic responses and resisitivity, it is necessary that the petrophysical parameters represent all these variations, even though the model is at a scale to coarse to capture all these properties in detail. Upscaling is a technique to bring information from one scale to a coarser in a consistent manner. Thus one upscaled model can be seen as homogeneous with a set of effective properties for its scale.

For elastic properties, upscaling has traditionally been done by different volume weighted averaging methods such as Voigt, Reuss or Backus averages which utilize limited or no information about the geology of the rock. The objective here is to do upscaling based on a technology where geological information is taken into account.

This thesis considers different aspects governing elasticity upscaling in general and general geometry upscaling in particular. After the theory part it considers verification of the general geometry method and the implementation of this, projection of an elasticity tensor onto a certain symmetry and visualization of elastic moduli. Next the importance of including geological information is studied and upscaling is done on examples of realistic reservoir models. Finally elasticity upscaling utilized in a bottom-up approach to model 4D seismic is considered.

Contents

Chapter 1

Introduction

Geological structures occur at many different length scales [1]. One knows that for fluid flow, geological structures at all length scales can be important, therefore it is natural to assume that seismic waves could also be affected by features at many different scales. Ideally reservoir models should regard geological characteristics at all length scales. However, such a model would be to big for computations. One solution to this is to discretize with respect to scale by identifying the most important scales. The representative elementary volume concept (REV) is used to identify these scales. Within each REV, the physical properties in question, such as elastic modulus and density, are assumed constant. Figure 1 shows an example of models at different scales in a reservoir from pore scale, at which the models can be on the size of a sugar lump, to models which are several kilometers long.

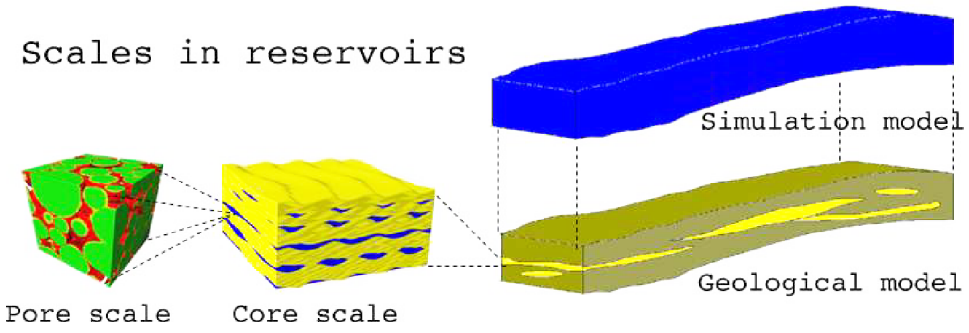

Figure 1: *Various scales in a reservoir.*

In order to utilize information from many different scales simulta-

neously, one needs a tool to bring these together in a consistent manner. This can be done by upscaling the small scale information by using different homogenization techniques.

In this thesis, upscaling of elastic parameters by utilizing a method based on homogenization theory is considered. One possible application of this is for example forward modelling of 4D seismic which can be used in history matching or for comparison to sonic logs. Given models at all scales, one can compute the effective wave velocities at seismic scale for adjustments done at pore scale. If one for example knows the elastic parameters as function of the fluid saturations on pore scale, these could be upscaled to seismic scale and compared with sonic log data in order to determine the reservoir fluid saturations.

In one particular upscaling step, one has a composition of cells where the physical parameters are assumed constant in each cell. Such a composition represents a certain geometry which imitates a geological feature for example a special deposition pattern. One question is whether the geometry is important for the effective physical parameters, or if these are equal for all compositions with the same volume fractions of each rock type. In the latter case a much cheaper upscaling could be done by some kind of wolume weighted average. This is addressed in chapter 7.

An elastic modulus has 81 components. Due to equilibrium of the medium and thermodynamical laws, only 21 of these are independent. Symmetries in the compositions of the rocks may result in even fewer independent components yielding different symmetries of the elastic moduli. The most general symmetry with 21 free components is called triclinic. The upscaled result will nearly always be triclinic either due to the model just being close to the higher symmetry or due to numerical errors. To establish the existence of higher symmetries, projections of the elasticity tensor onto the symmetries isotropy (directional independence) and transverse isotropy (layering symmetry) are presented in chapter 5.

It may be hard to interpret a general elastic modulus directly, especially if it has 21 free components. A perhaps more intuitive way to express it is in terms of corresponding wave velocities. Thus, to ease interpretation of the moduli in this thesis, visualizations of the corresponding wave velocities in both 3D and 2D are considered in chapter 6.

Chapter 3 presents traditional upscaling methods such as Voigt, Reuss and Backus averaging and the methology based on mathe-

matical homogenization used here for upscaling of general geometries. The correctness of the general geometry method is verified in chapter 4.

In chapter 8 and 9 upscaling is utilized on real reservoir models, i.e. on models which are built by a geologist based on an actual reservoir. Chapter 8 deals with models at lithofacies scale but fine scale elastic parameters are not related to a particular reservoir. Chapter 9 considers channel infill facies models where the fine scale properties originate from a sonic log. Here the channel infill facies is the scale above lithofacies, i.e. the cells in a channel infill facies model are at lithofacies scale.

An important purpose of upscaling elastic properties in a reservoir, is to use the result to determine the amounts of hydrocarbon reserves within the reservoir. One utilization of the upscaling could be to do forward seismic modelling by adjusting fluid properties at cell scale, upscale to find the corresponding effective moduli and use this to predict the seismic velocities. An example of one step of how this can be done is presented in chapter 10.

Chapter 2

Background theory

2.1 Seismology and rock physics

In the oil industry, seismology is one of the most important geophysical fields to find and monitor petroleum reservoirs. The methodology is to send elastic waves through the subsurface and analyze the reflections of these that emerge to the surface again. To interpret these reflection data into knowledge of the geological structures in which the waves have travelled, one needs a physical model that describes how waves act in different media.

A material is defined as continuous if it contains no empty spaces and its properties can be described by spatially continuous functions. Rock is a collection of minerals, which again consist of atoms. Most rocks, especially sedimentary rocks which are common in petroleum reservoirs, contain pores. However, at a scale larger than the atomic and larger than grain scale, rocks can be considered to have no voids [8] and instead porosity is introduced as a physical parameter. Also, the properties are assumed continuous at this scale and hence rock is considered continuous. Rock formations built up of different rock types can be described as piecewise continuous regions separated by interfaces where the physical properties are discontinuous.

Deformations in rocks due to seismic waves are often assumed to be linearly elastic. The definition of an elastic medium is that after deformation, it returns to equilibrium. For linearly elastic materials, the relationship between force and deformation is linear. The linearity assumption is valid when forces, deformation and the gradients of deformation are small. These assumptions are good enough for

most rock formations when they are exposed to seismic waves [8].

If at each point the physical properties, for example wave velocity, of a material are equal in all directions, the material is denoted isotropic, while in the opposite case, it is denoted anisotropic. In rock physics, different rocks are often assumed isotropic for simplicity and in lack of software to handle anisotropy. The isotropy assumption is valid for non viscous liquids and approximately valid at a macroscopic scale for some rock formations.

If the physical properties of a material are equal at all points, the material is homogeneous. Otherwise it is denoted heterogeneous.

The isotropy and homogeneity characterizations of a material are independent and should not be confused with each other.

2.2 Generalized Hooke's law

Many of the physical quantities in this thesis are described in terms of tensors. A tensor is a mulitilinear differential form, invariant with respect to a group of permissible coordinate transformations in n-space [4]. Tensors with orthonormal bases are called cartesian tensors. Tensors can be represented by algebraic structures, i.e. a zero order tensor can be represented by a scalar, a first order tensor by a vector, a second order tensor by a matrix and so on. Note however that a matrix not necessarily is a representation of a second order tensor or that a vector is not necessarily a first order tensor. A second order tensor T with components T_{ij} $i = 1, ..., m,\ j = 1, ..., n$ can also be represented by a vector V by for example

$$V = \begin{pmatrix} T_{11} & ... & T_{1n} & ... & T_{m1} & ... & T_{mn} \end{pmatrix}^T.$$

If a tensor has a certain symmetry, the representation only needs as many components as the number of independent components in the tensor. Second and fourth order tensors enter Hooke's law. Due to symmetries these are represented by vectors and matrices respectively.

A seismic wave is local particle motions in the material that propagate through space. The internal forces in the medium that restore equilibrium after an external force has disrupted the particle positions are called stresses. A nice definition of stress is given by [13], "Stress, defined as force per unit area, is a measure of the intensity of the total internal forces acting within a body across imaginary internal surfaces, as a reaction to external applied forces and body

forces." A way of envisioning this is to consider the particle in the position at which the stress acts. By describing the particle as a volume, the stress can be described as a set of surface forces acting on a volume element. Two and two opposite faces of this volume element are perpendicular to three unit vectors spanning the space (not necessary perpendicular to each other). The different stress components are shown in figure 2. The stress acting on each of

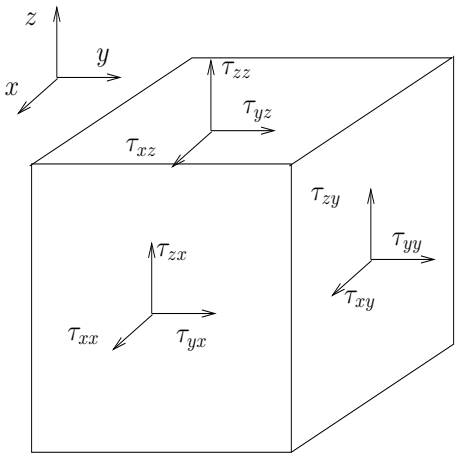

Figure 2: *The stress acting on a volume element.*

these face pairs is in general not perpendicular to the faces and is described by a three component vector. In total a nine component second order tensor is needed to describe the stress at each point,

$$\tau = \begin{pmatrix} \tau_{xx} & \tau_{xy} & \tau_{xz} \\ \tau_{yx} & \tau_{yy} & \tau_{yz} \\ \tau_{zx} & \tau_{zy} & \tau_{zz} \end{pmatrix},$$

where τ_{ij} is the i-component of the stress vector acting on the surface perpendicular to the j-direction.

For a medium in equilibrium, the stress tensor must be symmetric [8],

$$\tau_{ij} = \tau_{ji},$$

hence there are six independent stress components and by using

Voigt notation [14], the stress can be represented by a vector

$$\tau = \begin{pmatrix} \tau_{xx} \\ \tau_{yy} \\ \tau_{zz} \\ \tau_{yz} \\ \tau_{xz} \\ \tau_{xy} \end{pmatrix} = \begin{pmatrix} \sigma_1 \\ \sigma_2 \\ \sigma_3 \\ \sigma_4 \\ \sigma_5 \\ \sigma_6 \end{pmatrix}. \tag{1}$$

When a material is subject to force, for example if a wave propagates through a material, the particles are moving relative to each other, i.e. the material deforms. The deformability of the material can be described by a nine component strain tensor consisting of relative displacements within the material. If $\boldsymbol{u}(\boldsymbol{x}, t)$ is the displacement at time t for the particle in position $\boldsymbol{x}$ before the wave was transmitted, i.e. at time $t = 0$, the deformability of the material is given by

$$e = \begin{pmatrix} e_{xx} & e_{xy} & e_{xz} \\ e_{yx} & e_{yy} & e_{yz} \\ e_{zx} & e_{zy} & e_{zz} \end{pmatrix},$$

where

$$e_{ij} = \frac{1}{2}\left(\frac{\partial u_i}{\partial x_j} + \frac{\partial u_j}{\partial x_i}\right). \tag{2}$$

From this it follows that strain is displacement per length unit thus dimensionless. This is illustrated in figure 3. Since $e_{ij} = e_{ji}\ \forall i, j$, there are only six independent strain components and strain can be represented by a six component vector,

$$\varepsilon = \begin{pmatrix} e_{xx} \\ e_{yy} \\ e_{zz} \\ 2e_{yz} \\ 2e_{xz} \\ 2e_{xy} \end{pmatrix} = \begin{pmatrix} \varepsilon_1 \\ \varepsilon_2 \\ \varepsilon_3 \\ \varepsilon_4 \\ \varepsilon_5 \\ \varepsilon_6 \end{pmatrix}. \tag{3}$$

The factor 2 which is multiplied to the off diagonals in this definition can be motivated by Hooke's law in Voigt notation given in equation (8).

The generalized Hooke's law,

$$\tau = \mathbb{C}\, e, \tag{4}$$

descibes the linear relationship between stress and strain. Since both stress, τ, and strain, e, are second order tensors, $\mathbb{C}$ must be a

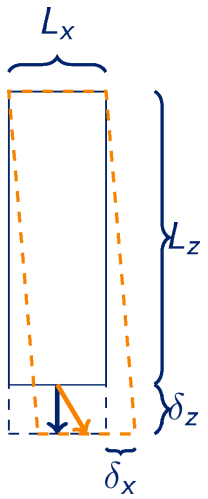

Figure 3: *Example of displacement of a volume element. Here the strain component* e_{xz} *is given by* $e_{xz} = \frac{1}{2}\left(\frac{\delta_z}{L_x} + \frac{\delta_x}{Lz}\right)$.

fourth order tensor with elements $[c_{ijkl}]_{i,j,k,l=1}^{3}$, thus Hooke's law can be written

$$\tau_{ij}(\boldsymbol{x}, t) = \sum_k \sum_l c_{ijkl}(\boldsymbol{x}) e_{kl}(\boldsymbol{x}, t) \tag{5}$$

on component form where $\boldsymbol{x}$ is spatial localization and t is the time. The tensor $\mathbb{C}$ is called the stiffness tensor, or elastic modulus. For elastic media, $\mathbb{C}$ is independent of time. The symmetries in stress, $\tau_{ij} = \tau_{ji}$, and strain, $e_{kl} = e_{lk}$, result in corresponding symmetries in $\mathbb{C}$,

$$\begin{aligned} e_{kl} = e_{lk} &\Rightarrow c_{ijkl} = c_{ijlk} \\ \tau_{ij} = \tau_{ji} &\Rightarrow c_{ijkl} = c_{jikl}. \end{aligned}$$

From thermodynamics one obtains one additional symmetry [2],

$$c_{ijkl} = c_{klij},$$

and the total number of independent components in $\mathbb{C}$ are 21 in the most general case. The symmetry from thermodynamics is equivalent to requiring that the wave speeds are non-negative. Thus, by using Voigt notation [14], $\mathbb{C}$ can be represented as a 6×6 symmetric matrix $\mathbf{C}$ with components C_{IJ},

$$C_{IJ} = c_{ijkl} = c_{klij} = C_{JI}, \tag{6}$$

$$\begin{aligned} I &= i\delta_{ij} + (9 - i - j)(1 - \delta_{ij}), \\ J &= k\delta_{kl} + (9 - k - l)(1 - \delta_{kl}), \end{aligned} \tag{7}$$

where δ_{ij} is the Kronecher-delta. Hooke's law can thus be expressed as

$$\sigma_I = \sum_J C_{IJ}\varepsilon_J. \tag{8}$$

Throughout this thesis, the elastic modulus on tensor form will be denoted $\mathbb{C}$ with components c_{ijkl} while the matrix representation of this will be denoted $\mathbf{C}$ with components C_{IJ}.

2.3 Wave velocities

Newton's equation of motion, force equals mass times acceleration, leads to the wave equation [8]

$$\rho(\boldsymbol{x})\frac{\partial^2 u_i(\boldsymbol{x},t)}{\partial t^2} = \sum_j \frac{\partial \tau_{ij}(\boldsymbol{x},t)}{\partial x_j}.$$

Combining this with Hooke's law given in equation (5) yields

$$\rho(\boldsymbol{x})\partial_t^2 u_i(\boldsymbol{x},t) = \sum_j \partial_{x_j}\left(\sum_k\sum_l c_{ijkl}(\boldsymbol{x})\partial_{x_l}u_k(\boldsymbol{x},t)(\boldsymbol{x},t)\right)$$

where ρ is the density and $\partial_x = \frac{\partial}{\partial x}$. For a homogeneous medium, $\mathbb{C}$ and ρ are independent of spatial position and the equation become

$$\rho\partial_t^2 u_i(\boldsymbol{x},t) = \sum_j\sum_k\sum_l c_{ijkl}\partial_{x_j}\partial_{x_l}u_k(\boldsymbol{x},t)(\boldsymbol{x},t). \tag{9}$$

If $\boldsymbol{u}$ is the velocity field and $\boldsymbol{U}$ is the polarization vector, the kth component of $\boldsymbol{u}$ can be written as

$$u_k = U_k\,\mathrm{e}^{-\mathrm{i}\omega\left(t-\sum_j \frac{n_j x_j}{V(\boldsymbol{n})}\right)}.$$

Here ω is the angular frequency, $V(\boldsymbol{n})$ is the wave propagation velocity and $\boldsymbol{n}$ is a unit vector in the wave propagation direction. Substituting this into the wave equation (9) results in the Christoffel equation

$$\sum_k \left(\Gamma_{ik} - \rho V^2\delta_{ik}\right)U_k = 0 \tag{10}$$
$$\Gamma_{ik} = \sum_{j,l} c_{ijkl}n_j n_l.$$

Hence ρV^2 are the eigenvalues of the Christoffel matrix Γ and the polarization vectors $\mathbf{U} = [U_k]_{k=1}^3$ are the corresponding eigenvectors. Together these defines an eigenvalue-eigenvector problem,

$$\Gamma \, \mathbf{U} = \begin{pmatrix} 0 & 0 & 0 \end{pmatrix}^T$$

For practical calculations D is defined such that

$$D^T = \begin{pmatrix} n_1 & 0 & 0 & 0 & n_3 & n_2 \\ 0 & n_2 & 0 & n_3 & 0 & n_1 \\ 0 & 0 & n_3 & n_2 & n_1 & 0 \end{pmatrix}.$$

Then Γ is equal to

$$\Gamma = D^T \mathbf{C} D \tag{11}$$

in Voigt notation.

Since D is a 6×3 matrix and $\mathbf{C}$ is a 6×6 matrix, Γ is a 3×3 matrix. Thus one gets 3 eigenvalues ρV^2 yielding 3 different wave velocities, thus there are three waves propagating in direction $\begin{pmatrix} n_1 & n_2 & n_3 \end{pmatrix}^T$. From (10) one sees that the Christoffel matrix Γ is symmetric, thus the three eigenvectors (polarization vectors) will be mutually orthogonal [8]. The wave with polarization along the propagation direction is called the P wave (for pressure wave), while the two others with polarization perpendicular to the propagation direction are called S waves (for shear waves).

2.4 Symmetries

The most general elasticity tensor is called triclinic and has 21 independent components,

$$\begin{pmatrix} c_{11} & c_{12} & c_{13} & c_{14} & c_{15} & c_{16} \\ c_{12} & c_{22} & c_{23} & c_{24} & c_{25} & c_{26} \\ c_{13} & c_{23} & c_{33} & c_{34} & c_{35} & c_{36} \\ c_{14} & c_{24} & c_{34} & c_{44} & c_{45} & c_{46} \\ c_{15} & c_{25} & c_{35} & c_{45} & c_{55} & c_{56} \\ c_{16} & c_{26} & c_{36} & c_{46} & c_{56} & c_{66} \end{pmatrix},$$

and Hooke's law (8) becomes

$$\begin{pmatrix}\sigma_1\\ \sigma_2\\ \sigma_3\\ \sigma_4\\ \sigma_5\\ \sigma_6\end{pmatrix} = \begin{pmatrix}c_{11} & c_{12} & c_{13} & c_{14} & c_{15} & c_{16}\\ c_{12} & c_{22} & c_{23} & c_{24} & c_{25} & c_{26}\\ c_{13} & c_{23} & c_{33} & c_{34} & c_{35} & c_{36}\\ c_{14} & c_{24} & c_{34} & c_{44} & c_{45} & c_{46}\\ c_{15} & c_{25} & c_{35} & c_{45} & c_{55} & c_{56}\\ c_{16} & c_{26} & c_{36} & c_{46} & c_{56} & c_{66}\end{pmatrix}\begin{pmatrix}\varepsilon_1\\ \varepsilon_2\\ \varepsilon_3\\ \varepsilon_4\\ \varepsilon_5\\ \varepsilon_6\end{pmatrix}.$$

If the material has some kind of symmetry, the number of independent components is reduced.

2.4.1 Isotropy

The highest symmetry possible is called isotropy and in this case the stiffness tensor has only two independent components. There exists several different parameters to describe an isotropic material, some of the most common being bulk and shear moduli (K and μ), Lamè's λ parameter, Young's modulus (E), Poisson's ratio (ν) and P wave modulus (M). Any pair of these parameters describes the elasticity tensor of isotropic materials and the relationship between them are given in table 1.

	(λ,μ)	(E,ν)	(K,μ)
K	$\lambda+\frac{2\mu}{3}$	$\frac{E}{3(1-2\nu)}$	K
E	$\mu\frac{3\lambda+2\mu}{\lambda+\mu}$	E	$\frac{9K\mu}{3K+\mu}$
λ	λ	$\frac{E\nu}{(1+\nu)(1-2\nu)}$	$K-\frac{2\mu}{3}$
μ	μ	$\frac{E}{2+2\nu}$	μ
ν	$\frac{\lambda}{2(\lambda+\mu)}$	ν	$\frac{3K-2\mu}{2(3K+\mu)}$
M	$\lambda+2\mu$	$\frac{1-\nu}{(1+\nu)(1-2\nu)}$	$K+\frac{4\mu}{3}$

Table 1: Relation between the different elasticity parameters for isotropic materials.

In terms of λ and μ, the elastic modulus is given as

$$\begin{pmatrix}\lambda+2\mu & \lambda & \lambda & 0 & 0 & 0\\ \lambda & \lambda+2\mu & \lambda & 0 & 0 & 0\\ \lambda & \lambda & \lambda+2\mu & 0 & 0 & 0\\ 0 & 0 & 0 & \mu & 0 & 0\\ 0 & 0 & 0 & 0 & \mu & 0\\ 0 & 0 & 0 & 0 & 0 & \mu\end{pmatrix}. \tag{12}$$

Solving the Christoffel equations for an isotropic elasticity tensor yields eigenvalues μ and $\lambda + 2\mu$ where μ has multiplicity 2 for all directions. This means that the two S-waves coincide and the wave velocities in an isotropic medium is independent of propagation direction. The velocities are given by

$$V_P = \sqrt{\frac{\lambda + 2\mu}{\rho}} \qquad (13)$$
$$V_S = \sqrt{\frac{\mu}{\rho}}$$

for the P and S waves respectively.

The isotropy assumption is widely used in reservoir modelling. This is because many materials are approximately isotropic at a macroscopic scale, but also for its simplicity.

2.4.2 Transverse isotropy

Another common symmetry used is transverse isotropy, often referred to as TI. These are materials where the physical parameters are isotropic along horizons, i.e. it has a unique symmetry axis around which rotations does not change the physical properties. This is for example the case for rocks which are composed by perfect layers of isotropic rocks.

In the upper crust of the earth, different substances are transported around due to glacier movements, rivers and winds and the different sediments are deposited in sedimentary basins. A basin can contain layers of different sediments due to different minerals being transported at different times. Over time these layers can be cemented and become sedimentary rock types. A great part of the underburden in the north sea are made up by such processes and therefore often have a structure where different rock types occurs in horizontal layers. As will be presented in section 3.2, the elastic moduli of horizontal layered mediums can be found by Backus averaging, which results in TI symmetric elastic moduli with symmetry axis be perpendicular to the layers. Therefore the symmetry axis of TI mediums are often in, or close to, the vertical direction.

The elastic moduli for transversely isotropic mediums have 5 inde-

pendent components and has the form

$$\begin{pmatrix} c_{11} & c_{11}-2c_{66} & c_{13} & 0 & 0 & 0 \\ c_{11}-2c_{66} & c_{11} & c_{13} & 0 & 0 & 0 \\ c_{13} & c_{13} & c_{33} & 0 & 0 & 0 \\ 0 & 0 & 0 & c_{44} & 0 & 0 \\ 0 & 0 & 0 & 0 & c_{44} & 0 \\ 0 & 0 & 0 & 0 & 0 & c_{66} \end{pmatrix} \tag{14}$$

when the symmetry axis is parallel to the z-direction.

The wave velocities in a TI medium are given by

$$\begin{aligned} V_P(\theta) &= \sqrt{\frac{C_{11}\sin^2(\theta)+C_{33}\cos^2(\theta)+C_{44}+\sqrt{M(\theta)}}{2\rho}} \\ V_{SV}(\theta) &= \sqrt{\frac{C_{11}\sin^2(\theta)+C_{33}\cos^2(\theta)+C_{44}-\sqrt{M(\theta)}}{2\rho}} \\ V_{SH} &= \sqrt{\frac{C_{66}\sin^2(\theta)+C_{44}\cos^2(\theta)}{\rho}} \\ M(\theta) &= \left[(C_{11}-C_{44})\sin^2(\theta)-(C_{33}-C_{44})\cos^2(\theta)\right]^2 \\ &\quad +(C_{13}+C_{44})\sin^2(2\theta) \end{aligned} \tag{15}$$

where θ is the angle between the symmetry axis and the direction of propagation [9]. This symmetry class is throughout this thesis referred to as TI.

2.4.3 Other symmetries

Isotropic and TI are two of the most common symmetries in reservoir modelling and are the two considered in this thesis. Other symmetries are for example cubic, trigonal and rhombic (orthotropic).

2.5 Norm of an elastic tensor

Since the elastic modulus, $\mathbb{C}$, is a fourth order tensor and the 6×6 matrix C is just a way of representing this, all norms used here deal with the tensor, i.e. a weighting is done on each term in C according to the number of occurrences this term has in the tensor.

The Euclidean distance (Frobenius norm) are for example given by

$$\|\mathbb{C}\|_F^2 = \sum_{i,j,k,l=1}^{3} c_{ijkl}^2 \tag{16}$$

$$= \sum_{i,j=1}^{3} C_{ij}^2 + 2\sum_{i=1}^{3}\sum_{j=4}^{6} C_{ij}^2 + 2\sum_{i=4}^{6}\sum_{j=1}^{3} C_{ij}^2 + 4\sum_{i,j=4}^{6} C_{ij}^2$$

$$= \sum_{i,j=1}^{3} C_{ij}^2 + 4\sum_{i=1}^{6}\sum_{j=4}^{6} C_{ij}^2 \tag{17}$$

where C_{ij} are the elements of $\mathbf{C}$.

2.6 Orthogonal rotation of tensors

Due to plate tectonically movements of the earth's upper crust, volcanoes and earthquakes, layers do not always have to be horizontal aligned, see e.g. [11] or [12]. This is also the case for other geological features, they can occur in many different orientations.

If one knows the stiffness tensor for a certain geological feature, say layered mediums, then one can find the stiffness tensor for tilted layers by rotating the known tensor according to a change in basis.

A rotation can be defined by a 3×3 matrix A with components

$$A_{ij} = (\boldsymbol{n}_i', \boldsymbol{n}_j) \tag{18}$$

where $\boldsymbol{n}_i'$, $i = 1, 2, 3$ are the basis vectors of the new coordinate system and $\boldsymbol{n}_j$, $j = 1, 2, 3$ are the basis vectors of the old coordinate system and $(\cdot, \cdot)$ is the inner product.

Let $\boldsymbol{u} = [u_i]_{i=1}^3$ be a first order tensor given in the basis $\{n_1, n_2, n_3\}$ and $\boldsymbol{u}' = [u_i']_{i=1}^3$ be the same tensor given in the basis $\{n_1', n_2', n_3'\}$. These can be written in terms of the basis vectors,

$$\boldsymbol{u} = \sum_j u_j \boldsymbol{n}_j$$

$$\boldsymbol{u}' = \sum_j u_j' \boldsymbol{n}_j'.$$

The component of a vector in a certain direction is equal to the inner product of the vector and a unit vector in that direction. Hence the

jth component of a vector in a certain basis is equal to the inner product between the vector and the jth basis vector,

$$\begin{aligned} u_j &= (\boldsymbol{u}, \boldsymbol{n}_j) = \left(\boldsymbol{u}', \boldsymbol{n}_j\right) \\ u'_j &= \left(\boldsymbol{u}, \boldsymbol{n}'_j\right) = \left(\boldsymbol{u}', \boldsymbol{n}'_j\right), \end{aligned}$$

thus one has that

$$\begin{aligned} \boldsymbol{u} &= \sum_j (\boldsymbol{u}, \boldsymbol{n}_j)\, \boldsymbol{n}_j \\ \boldsymbol{u}' &= \sum_j \left(\boldsymbol{u}, \boldsymbol{n}'_j\right) \boldsymbol{n}'_j \\ u'_j &= \left(\boldsymbol{u}, \boldsymbol{n}'_j\right) = \left(\sum_k (\boldsymbol{u}, \boldsymbol{n}_k)\boldsymbol{n}_k, \boldsymbol{n}'_j\right) \\ &= \sum_k (\boldsymbol{u}, \boldsymbol{n}_k)\left(\boldsymbol{n}_k, \boldsymbol{n}'_j\right) = \sum_k A_{jk} u_k \\ \Rightarrow \boldsymbol{u}' &= A\boldsymbol{u} \end{aligned}$$

For a second order tensor σ and a first order tensor $\boldsymbol{u}$, the product $\boldsymbol{v} = \sigma\boldsymbol{u}$ is a first order tensor and hence

$$v'_i = \sum_j A_{ij} v_j = \sum_j A_{ij} \sum_k \sigma_{jk} u_k = \sum_j A_{ij} \sum_k \sigma_{jk} \sum_l A_{lk} u'_l.$$

By definition we also have

$$v'_i = \sum_l \sigma'_{il} u'_l,$$

and hence

$$\begin{aligned} \sigma'_{il} &= \sum_j \sum_k A_{ij} \sigma_{jk} A_{lk} \\ \Rightarrow \sigma' &= A\sigma A^T \end{aligned}$$

For a fourth order tensor $\mathbb{C} = [c_{ijkl}]$ and a second order tensor $\mathbf{e} = [e_{kl}]$, the product

$$\sigma = [\sigma_{ij}] = \left[\sum_{kl} c_{ijkl} e_{kl}\right]$$

is a second order tensor and

$$\sigma' = \left[\sigma'_{ij}\right] = \left[\sum_{kl} c'_{ijkl} e_{kl} l\right]$$

defines the rotation. Further

$$\sigma'_{ij} = \sum_{mn} A_{im}\sigma_{mn}A_{jn} = \sum_{mn} A_{im}A_{jn}\sum_{pq} c_{mnpq}e_{pq}$$
$$e_{pq} = \sum_{kl} A_{kp}A_{lq}e'_{kl}$$
$$\sigma'_{ij} = \sum_{mn}\sum_{pq}\sum_{kl} A_{im}A_{jn}A_{kp}A_{lq}e'_{kl},$$

hence

$$\Rightarrow c'_{ijkl} = \sum_{mnpq} A_{im}A_{jn}A_{kp}A_{lq}c_{mnpq} \tag{19}$$

For an elasticity tensor $\mathbf{C}$ represented as shown in equation (7), it can be shown that $\mathbf{C}'$ is given by

$$\mathbf{C}' = \mathbf{K}\mathbf{C}\mathbf{K}^T \tag{20}$$
$$\mathbf{K} = \begin{pmatrix} \mathbf{K}^{(1)} & \mathbf{K}^{(2)} \\ \mathbf{K}^{(3)} & \mathbf{K}^{(4)} \end{pmatrix},$$

where

$$K^{(1)}_{ij} = A^2_{ij}$$
$$K^{(2)}_{ij} = 2A_{i\ mod(j+1,3)}A_{i\ mod(j+2,3)}$$
$$K^{(3)}_{ij} = A_{mod(i+1,3)\ j}A_{mod(i+2,3)\ j}$$
$$K^{(4)}_{ij} = A_{mod(i+1,3)\ mod(j+1,3)}A_{mod(i+2,3)\ mod(j+2,3)} \cdot A_{mod(i+1,3)\ mod(j+2,3)}A_{mod(i+2,3)\ mod(j+2,3)}$$

and

$$mod(i,3) = \begin{cases} i & i \leq 3 \\ i-3 & i > 3 \end{cases}$$

Chapter 3

Upscaling of elastic parameters

Ideally a reservoir model should cover an entire hydrocarbon reservoir and have cells small enough to capture all possible geological features. Such a model could perhaps be $100\ \mathrm{m}$ high and have a horizontal extent of $1\ \mathrm{km}^2$, while one cell in a pore scale model, which is the smallest common modelling scale, can be about $1\ \mathrm{mm}^3$. This model would require 10^{17} cells and running simulation on such large models is not possible given the current processing powers of computers. What one can do instead is to make models at many different scales. Hence one needs some kind of upscaling of the physical properties to bring information from one scale to the next. Examples of different scales are pore scale $\left(\sim 10^{-3}\ \mathrm{m}\right)$, core scale $(\sim 10^{-2}\ \mathrm{m})$, geological scale $(\sim 10\ \mathrm{m})$ and simulation scale $(\sim 1000\ \mathrm{m})$. These are schematically shown in figure 4.

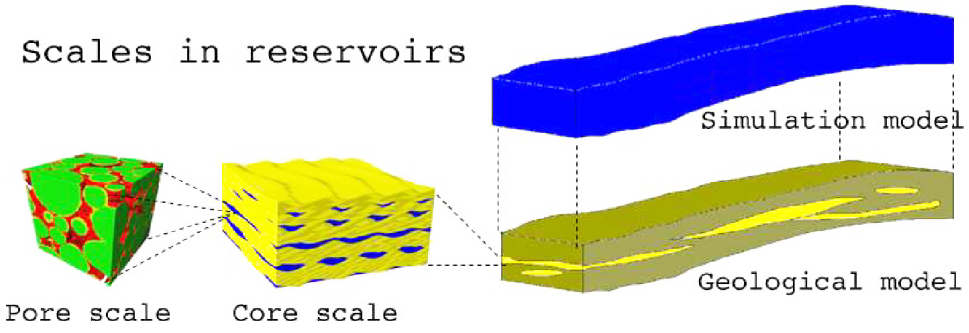

Figure 4: *Various scales in a reservoir.*

Consider a heterogeneous block where the elastic parameters vary throughout the geometry. The velocity of a wave with wave length much smaller than the size of the block will depend on where the wave travels. Assume for example that the yellow material at the bottom of the model in figure 5 is softer than the blue one on top and that the layers are isotropic. Then the wave will travel faster if it travels trough the blue area than in the yellow. A wave with wave length much larger than the size of the layer thickness will on the other hand have a velocity which will be some kind of average of the velocities in the two layers.

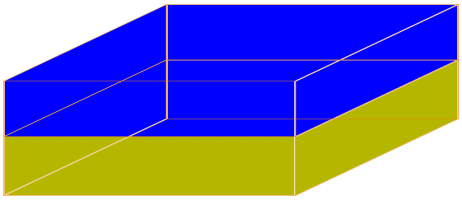

Figure 5: *A simple example formation with two cells*

Upscaling of elastic parameters is based on the idea to find an equivalent homogeneous medium which will have the same wave velocities as the real heterogeneous medium. The upscaling is done in the static limit, i.e. one assumes infinite wave length which for practical purposes means that the results are valid when the wave length is much larger than the typical size of the heterogeneities.

Classical homogenization is a mathematical method to upscale differential equations. An important concept when this theory is applied on porous media is the representative elementary volume, REV. If a physical parameter is constant over an interval of scale, then the volumes representing scales within that interval are REVs. Let u be a real valued function in space with rapidly spacial oscillations which represents a physical quantity. An example is porosity which will oscillate between 0 and 1 according to whether the spatial coordinate is in a void (pore) or not. To smoothen u, one looks at the average of this function over a volume $V(\boldsymbol{x})$ of the size of a REV,

$$\langle u \rangle (x) = \int_{V(\boldsymbol{x})} u(\boldsymbol{y}) dV.$$

While u represent the fine scale physical quantity, $\langle u \rangle$ represent the same physical quantity at coarse scale. As long as $V(\boldsymbol{x})$ is on a REV, $\langle u \rangle$ is constant. This means that when one is on a REV, the volume over which one smoothes the function can change relatively radically without changing the quantity at coarse scale.

For a general rock formation, the effective elastic modulus is dependent on the elastic moduli of the different rock types, on the volume fractions of the different rocks and on the geometry of the rock composition, i.e. of how the various rock types are arranged relatively to each other. Without geometrical information, the best one can do is compute bounds, e.g. Voigt and Reuss, in which the real modulus lies.

For perfectly layered mediums where the different rocks have TI symmetry or higher, the Backus average gives an analytical solution which is based on the effective medium theory presented by Backus.

3.1 Voigt and Reuss averages

In 1928 Voigt approximated the effective elastic moduli by assuming uniform strain throughout the composition and averaging the relations for stress [7]. One year later Reuss proposed averaging the expressions for strain assuming uniform stress. The Voigt and Reuss averages are given as

$$M_V = \sum_i f_i M_i \tag{21}$$

$$M_R = \frac{1}{\sum_i f_i \frac{1}{M_i}}, \tag{22}$$

where $f_i = \frac{V_i}{V}$, i.e. the volume portion of medium i and M is either the bulk or shear modulus.

In the next, it will be proven that the Voigt and Reuss averages are upper and lower bounds for the bulk and shear moduli. The idea behind the proof is taken from [7].

If σ and ε are the fine scale stress and strain, the composition is macroscopically homogeneous and contains a sufficiently large number of cells, the average energy density, stress times strain, has to be equal in terms of the coarse and fine scale parameters, i.e.

$$S^T E = \frac{1}{V} \int \sigma^T \varepsilon \, dV$$

where S and E are the coarse scale stress and strain. $S^T E$ is equal to twice the energy density.

Assume that Hooke's law (8) is valid at fine scale, i.e. $\sigma = c\varepsilon$. Let σ^* be the stress in a fine scale element corresponding to strain E and

ε^* be the strain in a fine scale element caused by the stress S, i.e.

$$\begin{aligned} \sigma^* &= \mathbf{c}\, E \\ S &= \mathbf{c}\, \varepsilon^*. \end{aligned}$$

In terms of σ^*, the the fine scale (double) energy densities, $\sigma^T\varepsilon$, can be written as

$$\begin{aligned} \sigma^T\varepsilon &= 2\sigma^T\varepsilon - \sigma^T\varepsilon + (\sigma^{*T}E - \sigma^{*T}E) + 2(\sigma^T E - \sigma^T E) \\ &= 2\varepsilon^T c\varepsilon - \varepsilon^T c\varepsilon + (E^T cE - E^T cE) + 2(\varepsilon^T cE - \varepsilon^T cE) \\ &= E^T cE + 2\varepsilon^T c\varepsilon - 2E^T c\varepsilon - \varepsilon^T c\varepsilon + \varepsilon^T cE + E^T c\varepsilon - E^T cE \\ &= \sigma^{*T}E + 2\left(\varepsilon^T\sigma - E^T\sigma\right) - \left(\sigma^T\varepsilon - \sigma^T E - \sigma^{*T}\varepsilon + \sigma^{*T}E\right) \\ &= \sigma^{*T}E + 2\left(\varepsilon - E\right)^T\sigma - \left(\sigma - \sigma^*\right)^T\left(\varepsilon - E\right). \end{aligned}$$

Similarily $\sigma^T\varepsilon$ can be written in terms of ε^*

$$\begin{aligned} \sigma^T\varepsilon &= 2\sigma^T\varepsilon - \sigma^T\varepsilon + (S^T\varepsilon^* - S^T\varepsilon^*) + 2(S^T\varepsilon - S^T\varepsilon) \\ &= 2\varepsilon^T c\varepsilon - \varepsilon^T c\varepsilon + (\varepsilon^{*T}c\varepsilon^* - \varepsilon^{*T}c\varepsilon^*) + 2(\varepsilon^{*T}c\varepsilon - \varepsilon^{*T}c\varepsilon) \\ &= \varepsilon^{*T}c\varepsilon^* + 2\varepsilon^T c\varepsilon - 2\varepsilon^{*T}c\varepsilon - \varepsilon^T c\varepsilon + \varepsilon^T c\varepsilon^a st + \varepsilon^{*T}c\varepsilon - \varepsilon^{*T}c\varepsilon^* \\ &= S^T\varepsilon^* + 2\left(\sigma^T\varepsilon - S^T\varepsilon\right) - \left(\sigma^T\varepsilon - \sigma^T\varepsilon^* - S^T\varepsilon + S^T\varepsilon\right) \\ &= S^T\varepsilon^* + 2\left(\sigma - S\right)^T\varepsilon - \left(\sigma - S\right)^T\left(\varepsilon - \varepsilon^*\right). \end{aligned}$$

The scalar product between stress and strain is related to the energy and therefore always positive, hence

$$\begin{aligned} (\sigma - \sigma^*)^T(\varepsilon - E) &= (\varepsilon - E)^T\mathbf{c}(\varepsilon - E) \geq 0 \\ (\sigma - S)^T(\varepsilon - \varepsilon^*) &= (\varepsilon - \varepsilon^*)^T\mathbf{c}(\varepsilon - \varepsilon^*) \geq 0. \end{aligned}$$

This is equivalent to the positive definiteness of the elastic modulus. For the fine scale energy densities one now gets

$$\begin{aligned} \sigma^T\varepsilon &\leq \sigma^{*T}E + 2(\varepsilon - E)^T\sigma \\ \sigma^T\varepsilon &\leq S^T\varepsilon^* + 2(\sigma - S)^T\varepsilon. \end{aligned}$$

which leads to

$$S^T E = \frac{1}{V}\int \sigma^T\varepsilon \, dV \leq \begin{cases} \frac{1}{V}\int \left(\sigma^{*T}E + 2(\varepsilon - E)^T\sigma\right) \, dV \\ \frac{1}{V}\int \left(S^T\varepsilon^* + 2(\sigma - S)^T\varepsilon\right) \, dV. \end{cases}$$

for the average energy density.

It can be shown (see e.g. [3]) that

$$\int (\varepsilon - E)^T \sigma \, dV \equiv 0$$
$$\int (\sigma - S)^T \varepsilon \, dV \equiv 0,$$

hence

$$S^T E \leq \begin{cases} E^T \frac{1}{V} \int \sigma^* dV \\ S^T \frac{1}{V} \int \varepsilon^* dV. \end{cases}$$

By requiring that the coarse scale elastic modulus $\mathbf{C}$ fulfills Hooke's law, $S = \mathbf{C}E$, one gets

$$E^T \mathbf{C} E \leq E^T \left(\frac{1}{V} \int \mathbf{c} \, dV \right) E$$
$$S^T \mathbf{C}^{-1} S \leq S^T \left(\frac{1}{V} \int \mathbf{c}^{-1} dV \right) S$$

The expressions to the right are the energy densities that would be calculated by the Voigt and Reuss theories.

For models built up of piece wise homogeneous rocks, the integral of elastic modulus over the model can be divided into a sum of integrals over each cell in which the elastic modulus is constant,

$$\frac{1}{V} \int \mathbf{c} \, dV = \sum_i \frac{1}{V} \int_{\Omega_i} \mathbf{c}^i \, dV_i = \sum_i \mathbf{c}^i \frac{1}{V} \int_{\Omega_i} dV_i = \sum_i \mathbf{c}^i f_i$$
$$\frac{1}{V} \int \mathbf{c}^{-1} \, dV = \sum_i \frac{1}{V} \int_{\Omega_i} \mathbf{c}^{i-1} \, dV_i = \sum_i \mathbf{c}^{i-1} \frac{1}{V} \int_{\Omega_i} dV_i = \sum_i \mathbf{c}^{i-1} f_i,$$

thus

$$E^T \mathbf{C} E \leq E^T \left(\sum_i \mathbf{c}^i f_i \right) E$$
$$S^T \mathbf{C}^{-1} S \leq S^T \left(\sum_i \mathbf{c}^{i-1} f_i \right) S$$

must hold for all E and S where f_i is the volume fraction of the ith medium.

Assume the composition is macroscopically isotropic with bulk and shear moduli K and μ, i.e. having elastic modulus

$$\mathbf{C} = \begin{pmatrix} K+\frac{4}{3}\mu & K-\frac{2}{3}\mu & K-\frac{2}{3}\mu & 0 & 0 & 0 \\ K-\frac{2}{3}\mu & K+\frac{4}{3}\mu & K-\frac{2}{3}\mu & 0 & 0 & 0 \\ K-\frac{2}{3}\mu & K-\frac{2}{3}\mu & K+\frac{4}{3}\mu & 0 & 0 & 0 \\ 0 & 0 & 0 & \mu & 0 & 0 \\ 0 & 0 & 0 & 0 & \mu & 0 \\ 0 & 0 & 0 & 0 & 0 & \mu \end{pmatrix}$$

and let K_V, μ_V, K_R and μ_R be the bulk and shear moduli computed by the Voigt and Reuss averages respectively.

First let $E = \begin{pmatrix} 1 & 1 & 1 & 0 & 0 & 0 \end{pmatrix}^T$.

$$\begin{aligned} E^T\mathbf{C}E &= 3\left(\left(K+\frac{4}{3}\mu\right)+2\left(K-\frac{2}{3}\mu\right)\right) = 9K \\ E^T\left(\sum_i \mathbf{c}^i f_i\right)E &= 3\left(\sum_i\left[f_i\left(K_i+\frac{4}{3}\mu_i\right)\right]+2\sum_i\left[f_i\left(K_i-\frac{2}{3}\mu_i\right)\right]\right) \\ &= 3\sum_i f_i\left[K_i+\frac{4}{3}\mu_i+2\left(K_i-\frac{2}{3}\mu_i\right)\right] \\ &= 9\sum_i f_i K_i = 9K_V \\ &\Rightarrow K \leq K_V. \end{aligned}$$

Secondly, let $E = \begin{pmatrix} 0 & 0 & 0 & 1 & 1 & 1 \end{pmatrix}^T$ which yields

$$\begin{aligned} E^T\mathbf{C}E &= 3\mu \\ E^T\left(\sum_i \mathbf{c}^i f_i\right)E &= 3\sum_i f_i\mu_i = 3\mu_V \\ &\Rightarrow \mu \leq \mu_V. \end{aligned}$$

Next let $S = \begin{pmatrix} 1 & 1 & 1 & 0 & 0 & 0 \end{pmatrix}^T$. The compliance $\mathbf{C}^{-1}$ is given as

$$\mathbf{C}^{-1} = \begin{pmatrix} \frac{1}{9K}+\frac{1}{3\mu} & \frac{1}{9K}-\frac{1}{6\mu} & \frac{1}{9K}-\frac{1}{6\mu} & 0 & 0 & 0 \\ \frac{1}{9K}-\frac{1}{6\mu} & \frac{1}{9K}+\frac{1}{3\mu} & \frac{1}{9K}-\frac{1}{6\mu} & 0 & 0 & 0 \\ \frac{1}{9K}-\frac{1}{6\mu} & \frac{1}{9K}-\frac{1}{6\mu} & \frac{1}{9K}+\frac{1}{3\mu} & 0 & 0 & 0 \\ 0 & 0 & 0 & \frac{1}{\mu} & 0 & 0 \\ 0 & 0 & 0 & 0 & \frac{1}{\mu} & 0 \\ 0 & 0 & 0 & 0 & 0 & \frac{1}{\mu} \end{pmatrix},$$

and one gets

$$
\begin{aligned}
S^T\mathbf{C}^{-1}S &= 3\left(\left(\frac{1}{9K}+\frac{1}{3\mu}\right)+2\left(\frac{1}{9K}-\frac{1}{6\mu}\right)\right)=\frac{1}{K}\\
S^T\left(\sum_i \mathbf{c}^{i-1}f_i\right)S &= 3\left(\sum_i\left[f_i\left(\frac{1}{9K_i}+\frac{1}{3\mu_i}\right)\right]\right.\\
&\qquad \left.+\,2\sum_i\left[f_i\left(\frac{1}{9K_i}-\frac{1}{6\mu_i}\right)\right]\right)\\
&= 3\sum_i\left[\frac{1}{9K_i}+\frac{1}{3\mu_i}+2\left(\frac{1}{9K_i}-\frac{1}{6\mu_i}\right)\right]\\
&= \sum_i f_i\frac{1}{K_i}=\frac{1}{K_R}\\
&\Rightarrow \frac{1}{K}\le\frac{1}{K_R}\Rightarrow K\ge K_R
\end{aligned}
$$

Finally let $S=\begin{pmatrix}0 & 0 & 0 & 1 & 1 & 1\end{pmatrix}^T$.

$$
\begin{aligned}
S^T\mathbf{C}^{-1}S &= 3\frac{1}{\mu}\\
S^T\left(\sum_i \mathbf{c}^{i-1}f_i\right)S &= 3\sum_i f_i\frac{1}{\mu_i}=3\frac{1}{\mu_R}\\
&\Rightarrow \frac{1}{\mu}\le\frac{1}{\mu_R}\Rightarrow \mu\ge\mu_R
\end{aligned}
$$

From the preveious one now has that

$$
\begin{aligned}
K_R\le K\le K_V\\
\mu_R\le\mu\le\mu_V,
\end{aligned}
$$

thus the Voigt and Reuss averages defines upper and lower bounds for the true bulk and shear moduli.

3.1.1 Upper and lower bounds

For some models the Reuss and Voigt averages are close, for example if the contrasts between the different rock types are small and the model is close to isotropy at the macroscopic scale. Since upscaling techniques which take general geometric information into account, such as the method to be presented in section 3.3, requires both time and computer power, one may in some cases want to use

a simpler upscaling, such as Voigt, Reuss or the average of these two called Voigt-Reuss-Hill. The latter of these, Voigt-Reuss-Hill, have no other physical meaning other than that since one knows that Voigt and Reuss defines the upper and lower bounds, this minimizes the error if one do not have any information about where the true value lies. To check if it is necessary to do a more precise upscaling, one should have some kind of upper and lower bounds of the elasticity also when the elasticity at microscopic scale is not isotropic. Since the elastic modulus is primarily used to compute wave velocities, the bounds C_{Upper} and C_{Lower} are isotropic and represents the maximum and minimum velocities through the material in the static limit (infinite wave length).

For materials which are isotropic at fine scale, upper and lower bounds for the bulk and shear moduli for the effective composition is given by the Voigt and Reuss averages given in equations (21) and (22) respectively [7]. Since $\mu = \rho V_S^2$ and $K = \rho\left(V_P^2 - \frac{4}{3}V_S^2\right)$ (equation (13) and table 1), the Voigt and Reuss bounds can can be written as

$$\begin{aligned}
\mu_V &= \sum_i f_i \mu_i = \sum_i f_i \rho_i V_{i_S}^2 \\
\mu_R &= \frac{1}{\sum_i f_i \frac{1}{\mu_i}} = \frac{1}{\sum_i f_i \frac{1}{\rho_i V_{i_S}^2}} \\
K_V &= \sum_i f_i K_i = \sum_i f_i \rho_i \left(V_{i_P}^2 - \frac{4}{3}V_{i_S}^2\right) \\
K_R &= \frac{1}{\sum_i f_i \frac{1}{K_i}} = \frac{1}{\sum_i f_i \frac{1}{\rho_i\left(V_{i_P} - \frac{4}{3}V_{i_S}^2\right)}}
\end{aligned}$$

In non-isotropic rock types, there are two different shear waves (in isotropic materials these coincide). The wave velocities V_{SV}, V_{SH} and

V_P are in general direction dependent and one has that

$$\begin{aligned}
\hat{\rho}V_S^2 &\leq \sum_i f_i \rho_i \max(V_{i_S})^2 = \mu_{Upper} \\
\hat{\rho}V_S^2 &\geq \frac{1}{\sum_i f_i \frac{1}{\rho_i \min(V_{i_S})^2}} = \mu_{Lower} \\
\hat{\rho}\left(V_P^2 - \frac{4}{3}V_S^2\right) &\leq \sum_i f_i \rho_i \max\left(V_{i_P}^2 - \frac{4}{3}V_{i_S}^2\right) = K_{Upper} \\
\hat{\rho}\left(V_P^2 - \frac{4}{3}V_S^2\right) &\geq \frac{1}{\sum_i f_i \frac{1}{\rho_i \min\left(V_{i_P}^2 - \frac{4}{3}V_{i_S}^2\right)}} = K_{Lower}.
\end{aligned} \tag{23}$$

where the min and max are over all possible directions and over both S waves. K_{Upper}, μ_{Upper}, K_{Lower} and μ_{Lower} thus define bulk and shear moduli of *imaginary isotropic materials* that represents the upper and lower limits for wave speed velocity. Note that for a certain rock composition, the velocities do not neccessarily have to be equal to these for any direction since the bounds take all internal orientations of the internal cells into consideration.

Rocks modelled at cell scale are assumed either isotropic or TI symmetric in this thesis, therefore these two symmetries will be considered here. In a TI medium the two shear waves are called SV and SH.

If the ith medium in equation (23) is isotropic, there is no cell-level direction dependence and min and max are equal,

$$\begin{aligned}
\rho_i \max\left(V_{i_S}^2\right) &\equiv \rho_i \min\left(V_{i_S}^2\right) \equiv \mu \\
\rho_i \max\left(V_{i_P}^2 - \frac{4}{3}V_{i_S}^2\right) &\equiv \rho_i \min\left(V_{i_P}^2 - \frac{4}{3}V_{i_S}^2\right) \equiv K + \frac{4}{3}\mu,
\end{aligned}$$

and if it is TI, then $\max\left(V_{i_P}^2 - \frac{4}{3}V_{i_S}^2\right)$, $\min\left(V_{i_P}^2 - \frac{4}{3}V_{i_S}^2\right)$, $\max\left(V_{i_S}^2\right)$ and $\min\left(V_{i_S}^2\right)$ has to be found using the direction dependent TI wave velocities in equtaion (15). To do this, $V_{i_S}^2$ and $V_{i_P}^2 - \frac{4}{3}V_{i_S}^2$ are differentiated with respect to the direction, θ, and set equal to zero to find

the extremal points, i.e.

$$\begin{aligned} \frac{\partial}{\partial\theta}V_{SV}^2(\theta) &= 0 \\ \frac{\partial}{\partial\theta}V_{SH}^2(\theta) &= 0 \\ \frac{\partial}{\partial\theta}\left(V_P^2(\theta) - \frac{4}{3}V_{SV}^2(\theta)\right) &= 0 \\ \frac{\partial}{\partial\theta}\left(V_P^2(\theta) - \frac{4}{3}V_{SH}^2(\theta)\right) &= 0 \end{aligned} \tag{24}$$

where V_P, V_{SV} and V_{SH} are the TI velocities.

Equation (24) is fulfilled for $\theta = n\frac{\pi}{2},\ n \in \mathbb{N}$, but have additional solutions which are harder to find analytically.

For mediums where the anisotropy is weak, the TI wave velocities can be approximated by Thomsen's weak anisotropy approximation,

$$\begin{aligned} V_P(\theta) &\approx \sqrt{\frac{c_{33}}{\rho}}\left(1 + \delta\sin^2(\theta)\cos^2(\theta) + \varepsilon\sin^4(\theta)\right) \\ V_{SV}(\theta) &\approx \sqrt{\frac{c_{44}}{\rho}}\left(1 + \frac{c_{33}}{c_{44}}(\varepsilon - \delta)\sin^2(\theta)\cos^2(\theta)\right) \\ V_{SH}(\theta) &\approx \sqrt{\frac{c_{44}}{\rho}}\left(1 + \gamma\sin^2(\theta)\right) \end{aligned} \tag{25}$$

where

$$\begin{aligned} \varepsilon &= \frac{c_{11} - c33}{2c_{33}} \\ \gamma &= \frac{c_{66} - c44}{2c_{44}} \\ \delta &= \frac{(c_{13} + c_{44})^2 - (c_{33} - c_{44})^2}{2c_{33}(c_{33} - c_{44})}. \end{aligned} \tag{26}$$

ε, γ and δ are called the Thomsen parameters and are indicators of anisotropy. As a rule of thumb, the Thomsen approximation is acceptable if all the Thomsen parameters are below 0.1 in absolute value, i.e. if $|\varepsilon| \leq 0.1$, $|\gamma| \leq 0.1$ and $|\delta| \leq 0.1$.

By comparing the exact TI wave velocities in equation (15) with the Thomsen approximation in (25), it is obviously easier to find the extremal points of Thomsens approximation than of the exact velocities since the derivative of the first will clearly give an easier expression. The remaining extremal θ points are therefore approximated by the extremal points of (25).

The additional approximate extremal θs found by using Thomsen's approximation are

$$\theta \approx \arcsin \pm \sqrt{\frac{\frac{4}{3}\sqrt{\frac{c_{33}}{c_{44}}}(\varepsilon-\delta)-\delta}{2\left(\frac{4}{3}\sqrt{\frac{c_{33}}{c_{44}}}+1\right)(\varepsilon-\delta)}}$$

for $V_P^2 - \frac{4}{3}V_{SV}^2$,

$$\theta \approx \arcsin \pm \sqrt{\sqrt{\frac{c_{44}}{c_{33}}}\frac{4}{3}\frac{\gamma}{\delta+2(\varepsilon-\delta)}}$$

for $V_P^2 - \frac{4}{3}V_{SH}^2$ and

$$\theta \approx \frac{\pi}{4}$$

for V_{SV}^2.

$\max(V_{i_S})$ in equation(23) is now approximately given by

$$\max(V_{i_S}) = \max(V_{i_{SVmax}}, V_{i_{SHmax}})$$

$$V_{i_{SVmax}} = \max \begin{cases} V_{i_{SV}}(0), \\ V_{i_{SV}}\left(\frac{\pi}{2}\right), \\ V_{i_{SV}}\left(\arcsin \sqrt{\frac{\frac{4}{3}\sqrt{\frac{c_{33}}{c_{44}}}(\varepsilon-\delta)-\delta}{2\left(\frac{4}{3}\sqrt{\frac{c_{33}}{c_{44}}}+1\right)(\varepsilon-\delta)}}\right), \\ V_{i_{SV}}\left(\arcsin -\sqrt{\frac{\frac{4}{3}\sqrt{\frac{c_{33}}{c_{44}}}(\varepsilon-\delta)-\delta}{2\left(\frac{4}{3}\sqrt{\frac{c_{33}}{c_{44}}}+1\right)(\varepsilon-\delta)}}\right) \end{cases}$$

$$V_{i_{SHmax}} = \max \begin{cases} V_{i_{SH}}(0), \\ V_{i_{SH}}\left(\frac{\pi}{2}\right), \\ V_{i_{SH}}\left(\arcsin \sqrt{\sqrt{\frac{c_{44}}{c_{33}}}\frac{4}{3}\frac{\gamma}{\delta+2(\varepsilon-\delta)}}\right), \\ V_{i_{SH}}\left(\arcsin -\sqrt{\sqrt{\frac{c_{44}}{c_{33}}}\frac{4}{3}\frac{\gamma}{\delta+2(\varepsilon-\delta)}}\right) \end{cases}$$

and analogous for $\min(V_{i_S})$, $\max\left(V_{i_P} - \frac{4}{3}V_{i_S}\right)$ and $\min\left(V_{i_P} - \frac{4}{3}V_{i_S}\right)$. Here the exact velocity formulas in equation (15) are used, the approximation lies only in the way of finding the θ's.

Since the bounds are approximate, inequality (23) does not hold, but the "bounds" will hopefully give an idea of the speed variation possible with the prevailing volume composition of rock types.

One could improve the bounds by using the extremal θ points found by Thomsen's approximation as starting values in a Newton iteration to find the exact extremal points. This is however out of scope for this thesis.

3.2 Backus averaging

In 1962 Backus presented an analytical formula for the effective elastic modulus for mediums made up by perfect layers of isotropic materials. The theory assume infinite wave length which for practical purposes means that Backus' formula is valid when the wave length is much larger than the thickness of each layer.

Elastic moduli computed with Backus' average are TI symmetric. Consider a material which is made up by perfect layers of TI materials all with symmetry axis perpendicular to the bedding. Then each layer will have an equivalent of layered isotropic materials, i.e. there exists a material made up by isotropic layers with the same effective elastic modulus as the TI layer. Thus the whole model has an equivalent of isotropic layers and there exists an analytical solution.

Backus averaging is based on the effective medium theory, i.e. the effective elastic modulus represents an equivalent homogeneous medium which have the same elastic properties, i.e. give the same wave velocities, as the real medium. Figure 6 illustrates the idea behind effective medium theory. Since the medium here is layered, Backus averaging can be used to find the effective elastic modulus if each layer is isotropic or TI with perpendicular symmetry axis.

The effective stiffness tensor components according to Backus are

$$\begin{aligned}
c_{11} = c_{22} &= \left\langle a - f^2 c^{-1} \right\rangle + \left\langle c^{-1} \right\rangle^{-1} \left\langle f c^{-1} \right\rangle^2 \\
c_{12} = c_{21} &= \left\langle b - f^2 c^{-1} \right\rangle + \left\langle c^{-1} \right\rangle^{-1} \left\langle f c^{-1} \right\rangle^2 \\
c_{33} &= \left\langle c^{-1} \right\rangle^{-1} \\
c_{13} = c_{23} = c_{31} = c_{32} &= \left\langle c^{-1} \right\rangle^{-1} \left\langle f c^{-1} \right\rangle^{-1} \\
c_{44} = c_{55} &= \left\langle d^{-1} \right\rangle^{-1} \\
c_{66} &= \langle m \rangle ,
\end{aligned}$$

where the brackets $\langle \cdot \rangle$ is the volume weighted average of the enclosed properties and a, b, c, d, f and m are the components of the

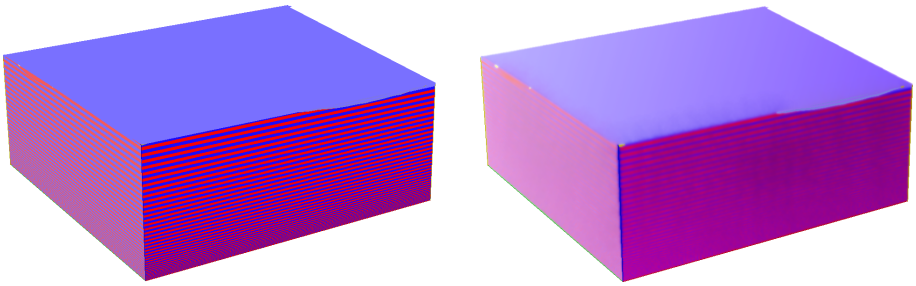

Figure 6: *The idea behind the effective medium theory is to find an equivalent homogeneous medium with the same physical properties as the real heterogeneous one. The model to the right, where fine scale heterogeneities are smoothed away, represents a homogeneous version of the layered heterogeneous medium to the left.*

stiffness tensors for the different layers given as

$$\begin{pmatrix} a & b & f & 0 & 0 & 0 \\ b & a & f & 0 & 0 & 0 \\ f & f & c & 0 & 0 & 0 \\ 0 & 0 & 0 & d & 0 & 0 \\ 0 & 0 & 0 & 0 & d & 0 \\ 0 & 0 & 0 & 0 & 0 & m \end{pmatrix}.$$

If each of the layers are isotropic, the formula above simplifies to

$$\begin{aligned} c_{11} = c_{22} &= \left\langle \frac{4\mu(\lambda+\mu)}{\lambda+2\mu} \right\rangle + \left\langle \frac{1}{\lambda+2\mu} \right\rangle^{-1} \left\langle \frac{\lambda}{\lambda+2\mu} \right\rangle^{2} \\ c_{12} = c_{21} &= \left\langle \frac{2\lambda\mu}{\lambda+2\mu} \right\rangle + \left\langle \frac{1}{\lambda+2\mu} \right\rangle^{-1} \left\langle \frac{\lambda}{\lambda+2\mu} \right\rangle^{2} \\ c_{33} &= \left\langle \frac{1}{\lambda+2\mu} \right\rangle^{-1} \\ c_{13} = c_{23} = c_{31} = c_{32} &= \left\langle \frac{1}{\lambda+2\mu} \right\rangle^{-1} \left\langle \frac{\lambda}{\lambda+2\mu} \right\rangle^{-1} \\ c_{44} = c_{55} &= \left\langle \frac{1}{\mu} \right\rangle^{-1} \\ c_{66} &= \langle \mu \rangle \end{aligned}$$

where λ and μ are given as in (12).

For mediums with non-horizontal layering, the analytical elastic modulus can be found by using tensor rotation (see section 2.6) of the Backus average. First find the effective modulus in a coordinate system where the vertical (n_3) axis is perpendicular to the

layering (Backus average). Then do a basis change of this tensor where the new vertical axis is, in fact, vertical, i.e. $\boldsymbol{n}_3 = \begin{pmatrix} 0 & 0 & 1 \end{pmatrix}$. The form of the resulting tensor will not have the same form as the one presented in (14), but the number of independent coefficients are still 5.

For approximately layered media, Backus averaging is often used as an approximation of the effective elasticity tensor. The usability of this approximation is directly related to how perfect the layering is.

3.3 Upscaling method for general geometries

For general geometries, no known analytical formula exists for an equivalent elasticity tensor. One should take note that periodicity of the medium is a common assumption behind classical homogenization theory and therefore the method will in general give best results for approximately periodic models. This section is mainly taken from [15] and is included for completeness.

3.3.1 Preserving physical expressions

The method is based on preservation of Hooke's law from fine to coarse scale when requiring that the expressions for stress divergence and strain are preserved. If u_i and U_i denote the displacements at fine and coarse scale respectively, one should have

$$\begin{aligned} U_i &= \langle u_i \rangle \\ \partial_i U_j &= \langle \partial_i u_j \rangle \\ \Rightarrow E_{ij} = \langle \varepsilon_{ij} \rangle &= \left\langle \frac{\partial_i u_j + \partial_j u_i}{2} \right\rangle = \frac{\partial_i U_j + \partial_j U_i}{2} \end{aligned}$$

where ε_{ij} and E_{ij} are the fine and coarse scale strains and $\langle \cdot \rangle$ is the volume wighted average.

For stress divergence one requires

$$\begin{aligned} S_{ij} &= \langle \sigma_{ij} \rangle \\ \Rightarrow \partial_i S_{ij} &= \partial_i \langle \sigma_{ij} \rangle = \langle \partial_i \sigma_{ij} \rangle \end{aligned}$$

where S is the effective (coarse scale) stress and σ is the fine scale stress.

It is also preferable to preserve the expression for energy,

$$E^T S = \left\langle \varepsilon^T \sigma \right\rangle .$$

Unfortunately, the expressions for energy, stress divergence and strain can not be preserved simultaneously in a general case. Numerically this over specifies the problem. However, if the model is periodic or perfectly layered, the three expressions can be upscaled simultaneously. Here the periodicity is taken care of by the boundary conditions. This will be explained in section 3.3.3.

Physically stiffness tensors for mediums in equilibrium are at least triclinic (see chapter 2). For models which are either periodic or perfectly layered, this property is preserved through the upscaling.

3.3.2 Basic equation

Many of the results in classical homogenization theory is based on a periodic medium assumption. In reservoirs, the rocks are not perfectly periodic, but often distinct regions can be approximately periodic. The derivation of the equations can be done either in a classical mathematical or in a physical approach, and these give the same result. Here a physical approach on equating the net fine-scale force is presented.

The fine scale force working on a domain with closed boundary is equal to the coarse scale force working on the same domain [15],

$$\oiint n_i \sigma_{ij} dS + \iiint b_j dV = \oiint n_i S_{ij} dS + \iiint B_j dV$$

where b_j and B_j are the fine and coarse scale body forces. Defining $B_j = \frac{1}{V} \iiint b_j dV = \langle b_j \rangle$ yields $\iiint b_j dV = \iiint B_j dV$ and

$$\oiint n_i \sigma_{ij} dS = \oiint n_i S_{ij} dS.$$

Using Gauss' integral theorem

$$\iiint_V (\nabla \cdot \mathbf{F}) = \oiint_{dV} \mathbf{F} \cdot \mathbf{n} dS$$

yields

$$\iiint_V \partial_i \sigma_{ij} dV = \iiint_V \partial_i S_{ij} dV$$
$$\Rightarrow \partial_i \sigma_{ij} = \partial_i S_{ij}$$

For a periodic medium, $S = [S_{ij}]_{i,j=1}^3$ and $\mathbb{C} = [c_{ijmn}]_{ijkl=1}^3$ are constant with respect to the fine scale, hence according to Hooke's law (8), so is E. This means that $\partial_i S_{ij} = 0$. Substituting Hooke's law in equation (5) and equation (2) one gets

$$\partial_i \sigma_{ij} = \partial_i \left(\sum_{mn} c_{ijmn} \left(\partial_m u_n + \partial_n u_m \right) \right) = 0$$

which is the equation that has to be solved in order to determine the fine scale displacements. In addition, one needs boundary conditions.

3.3.3 Boundary conditions

Recall that the coarse scale strain $E = [E_{ij}]_{i,j=1}^3$ is constant for periodic mediums. Therefore, as one sees from (2), the coarse scale displacement U_i is linear in x, i.e.

$$\boldsymbol{U}(\boldsymbol{x}) = \boldsymbol{U}_0 + A\boldsymbol{x}$$
$$E = \frac{1}{2}(A + A^T).$$

The fine scale displacement is equal to the coarse scale displacement plus a periodic function χ with the same periodicity as the fine scale elastic modulus,

$$\boldsymbol{u}(\boldsymbol{x}) = \boldsymbol{u}_0 + A\boldsymbol{x} = \boldsymbol{U}_0 + \chi(\boldsymbol{x}) + A\boldsymbol{x},$$

i.e. the displacement difference between two corresponding points on opposite boundaries is constant.

The system that has to be solved in order to determine the fine scale displacements is thus

$$\partial_i \left(\sum_{mn} c_{ijmn} \left(\partial_m u_n + \partial_n u_m \right) \right) = 0 \tag{27}$$
$$u_i(\boldsymbol{x}) = U_{0_i} + \chi_i(\boldsymbol{x}) + \sum_j A_{ij} x_j.$$

The boundary conditions can be chosen orthogonally as 9 different load cases. Stretch (or compression) in each direction plus shear displacement in the two other directions in each direction, altogether three different displacements in each direction as shown in figure 7. Since the strain and stress are symmetric, $E_{ij} = E_{ji}$ and $S_{ij} = S_{ji}$, it is enough to compute for the 6 of these corresponding to the Voigt notation, i.e. the upscaling can be done for E_{11}, E_{22}, E_{33}, E_{23} or E_{32}, E_{31} or E_{13} and E_{12} or E_{21}.

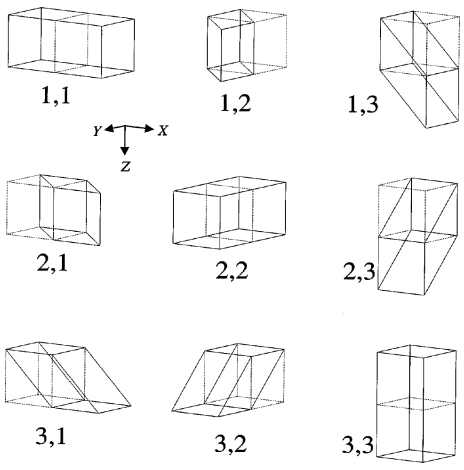

Figure 7: *The nine different load cases corresponding to orthogonal boundary conditions. Due to the symmetries in stress, strain and stiffness tensor, it is enough to compute for the three stretch cases,* $[E_{ii}]_{i=1}^{3}$ *and for example the upper half,* E_{23}*,* E_{31} *and* E_{12}*. The illustration is taken from [15].*

3.3.4 Numerical procedure

Roughly the procedure to compute the upscaled elastic modulus **C** is as follows

- Choose a load case, i.e. set one $E_{ij} \neq 0$ and $E_{kl} = 0,\ kl \neq ij$
- Compute the displacements in all cells by solving (27)
- Compute the strain ε for all cells from the displacements
- Compute the stress σ in each cell by using Hooke's law (4)
- Compute the coarse scale stress $S = \langle\sigma\rangle = \sum_{Cells} \frac{V_{Cell}}{V}\sigma_{Cell}$
- Compute the column of **C** corrsponding to the chosen load case by using Hooke's law (4). Since E has only one non-zero component, say the kth component, one gets $S_i = C_{ik}E_k$ $\Rightarrow C_{ik} = \frac{S_i}{E_k},\ i \in \{1, .., 6\}$
  (Here E and S are represented in the 6 component vector representations).

The computations in this thesis is done with a finite element based implementation of this method which is made by Sintef Applied Mathematics for StatoilHydro.

The upscaling is independent of scale, i.e. it can be used to upscale from 1 mm to 10 m and it can be used to upscale from 100 m to

$10\ \mathrm{km}$. What one should keep in mind, is that many results within homogenization theory are based on the assumption of periodicity of the medium. The applicability and validity of the result, taken the periodicity and whether both the cell sizes and the model size are representative elementary volumes (REVs) into account, are up to the user.

Chapter 4

Verification of the general upscaling method

No proper verification of the general geometry upscaling method has preveiously been done. Hence it first had to be verified with analytical cases. Different cases where the effective elastic modulus is known are used. First the method is tested on a two cell model where each cell is isotropic. The exact solution for this model can be computed by using Backus averaging, section 3.2. The next test is a simpler case, namely setting the elastic parameters equal in all cells. This test is run on several models, expecting the error to be larger the more cells there are in the model. The final test is to find the exact elastic modulus for a perfectly layered model with Backus averaging in 3.2, and then rotate the model and change the basis of the elasticity tensor accordingly. This creates a non trivial upscaling problem with an analytical solution.

4.1 A two cell model

The model shown in figure 5 has two equally thick layers. Populating these two layers with isotropic rock should yield results equal to Backus averaging since each layer is isotropic (and hence also TI). The rock properties, given by lamè parameter λ and shear modulus μ, are set equal to

$$\lambda_1 = 3,\ \mu_1 = 10$$
$$\lambda_2 = 8,\ \mu_2 = 15.$$

By Backus, the effective stiffness tensor components are

$$
\begin{aligned}
c_{11} = c_{22} &= \left\langle \frac{4\mu(\lambda+\mu)}{\lambda+2\mu} \right\rangle + \left\langle \frac{1}{\lambda+2\mu} \right\rangle^{-1} \left\langle \frac{\lambda}{\lambda+2\mu} \right\rangle^{2} = 30.295 \\
c_{33} &= \left\langle \frac{1}{\lambda+2\mu} \right\rangle^{-1} = 28.656 \\
c_{12} &= \left\langle \frac{2\mu\lambda}{\lambda+2\mu} \right\rangle + \left\langle \frac{1}{\lambda+2\mu} \right\rangle^{-1} \left\langle \frac{\lambda}{\lambda+2\mu} \right\rangle^{2} = 5.2951 \\
c_{13} = c_{23} &= \left\langle \frac{1}{\lambda+2\mu} \right\rangle^{-1} \left\langle \frac{\lambda}{\lambda+2\mu} \right\rangle = 4.8852 \\
c_{44} = c_{55} &= \left\langle \frac{1}{\mu} \right\rangle = 12 \\
c_{66} &= \langle \mu \rangle = 12.5
\end{aligned}
$$

In the upscaled result for this model,

$$
\mathbf{C}_{Upscaled} = \begin{pmatrix}
30.2951 & 5.29508 & 4.88525 & 0 & 0 & 0 \\
5.29508 & 30.2951 & 4.88525 & 0 & 0 & 0 \\
4.88525 & 4.88525 & 28.6557 & 0 & 0 & 0 \\
0 & 0 & 0 & 12 & 0 & 0 \\
0 & 0 & 0 & 0 & 12 & 0 \\
0 & 0 & 0 & 0 & 0 & 12.5
\end{pmatrix},
$$

all coefficients coinside with the theoretical values up to a factor of 10^{-3}. The errors that are present are due to rounding errors in the computations.

4.2 Homogeneous isotropic materials

If a model is populated with the same isotropic elasticity tensor in all cells, the result should be isotropic and equal to the input elasticity. This was done on several models with elasticity parameters

$$
\lambda = 5, \quad \mu = 10
$$

which corresponds to the elasticity tensor

$$
\mathbf{C}_{exact} = \begin{pmatrix}
25 & 5 & 5 & 0 & 0 & 0 \\
5 & 25 & 5 & 0 & 0 & 0 \\
5 & 5 & 25 & 0 & 0 & 0 \\
0 & 0 & 0 & 10 & 0 & 0 \\
0 & 0 & 0 & 0 & 10 & 0 \\
0 & 0 & 0 & 0 & 0 & 10
\end{pmatrix}.
$$

The relative error is given by

$$\frac{\|\mathbb{C}_{upscaled} - \mathbb{C}_{exact}\|_F}{\|\mathbb{C}_{exact}\|_F},$$

and these are given in table 2 for the different models. The first model is shown in figure 5, the second is shown in figure 8 and the lithofacies models numbered 1 to 6 are the ones in figure 24. Models 7 to 9 are also lithofacies models. The errors for the lithofacies models 1 to 6 are of order $O(10^{-2})$, while for lithofacies models 7 to 9 the errors vary more and are for example not increasing with the number of cells. This is due to the way the models are built. For the periodic model the error is of order $O(10^{-3})$ while for the simple two cell model the error is zero (up to data precision). Thus both the size and geometry of the model affect the error. The implementation is based on a finite element method to solve the differential equation for the displacements. The cells on two opposite sides are matched and if the cells do not correspond completely, this can cause numerical errors. This may be the reason why the errors are not only dependent on model sizes.

Model	*Error*	*Number of cells*
TwoCells	$3.6 \cdot 10^{-36}$	2
PeriodicTilted	$2.6 \cdot 10^{-3}$	3760
1	$1.02 \cdot 10^{-2}$	40847
2	$2.75 \cdot 10^{-2}$	149794
3	$1.98 \cdot 10^{-2}$	234156
4	$1.85 \cdot 10^{-2}$	50033
5	$1.78 \cdot 10^{-2}$	247972
6	$1.91 \cdot 10^{-2}$	209280
7	$1.5 \cdot 10^{-3}$	2217600
8	$2.2988 \cdot 10^{-5}$	45667
9	$3.13 \cdot 10^{-2}$	249298

Table 2: Relative upscaling error for isotropic populated models. Model 1 to 9 are lithofacies models, while the two first are simple test models.

4.3 Rotation of symmetric model upscaled by Backus

For a perfectly layered model with two different rock types, one in every other layer, and where each rock type is isotropic and ho-

mogeneous, the effective elasticity tensor can be found by Backus averaging (see section 3.2). An isotropic material is also TI since the set of isotropic elasticity tensors is a subset of the set of TI elasticity tensors. Then, to find the elasticity tensor of a model of the same size where the layers are rotated around the y-axis as shown in figure 8, one changes the basis of the original tensor correspondingly (see section 2.6). The model in figure 8 is made such that it is pe-

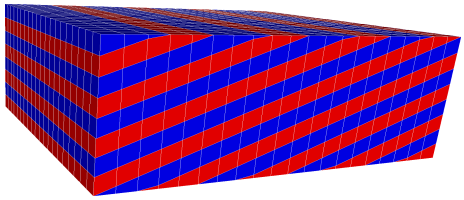

Figure 8: *A fully periodic model with two different rock types*

riodic, i.e. if one puts two of these together either in the vertical or in one of the horizontal directions, the layers are continuous also in the composition. This means that by using the general geometry upscaling method with periodic boundary conditions, the result should be equal to the rotated Backus average.

If the layers are too similar, i.e. the contrast between the elastic properties of the two layers is too small, the composition will be close to isotropy. Therefore the elastic properties of the two different layers are set such that there is a high contrast, not considering whether these numbers are realistic or not in a geological setting, but for the sake of verification only. With elastic properties of the layers equal to

$$\begin{aligned} K_1 = 5,\ \ \mu_1 = 5 \\ K_2 = 30,\ \ \mu_2 = 30, \end{aligned}$$

the elasticity tensor before rotation become

$$\mathbf{C}_{Horizontal} = \begin{pmatrix} 40.4080 & 5.4080 & 2.8570 & 0 & 0 & 0 \\ 5.4080 & 40.4080 & 2.8570 & 0 & 0 & 0 \\ 2.8570 & 2.8570 & 20.0000 & 8.5710 & 0 & 0 \\ 0 & 0 & 0 & 0 & 8.5710 & 0 \\ 0 & 0 & 0 & 0 & 0 & 17.5000 \end{pmatrix}.$$

Rotation of this tensor by 26.656° counter clock wise around the y-

direction results in

$$\mathbf{C}_{Rotated} = \begin{pmatrix} 33.0608 & 4.8978 & 6.1226 & 0 & -6.5308 & 0 \\ 4.8978 & 40.4080 & 3.3672 & 0 & -1.0204 & 0 \\ 6.1226 & 3.3672 & 20.8160 & 0 & -1.6324 & 0 \\ 0.0000 & 0 & 0 & 10.3568 & 0 & -3.5716 \\ -6.5308 & -1.0204 & -1.6324 & 0 & 11.8366 & 0 \\ 0 & 0 & 0 & -3.5716 & 0 & 15.7142 \end{pmatrix}$$

while the upscaling method gives

$$\mathbf{C}_{Upscaled} = \begin{pmatrix} 33.0655 & 4.8957 & 6.0987 & 0.0000 & -6.5343 & 0.0000 \\ 4.8957 & 40.5448 & 3.3497 & 0.0000 & -1.0204 & 0.0000 \\ 6.0987 & 3.3497 & 20.6972 & 0.0000 & -1.6290 & 0.0000 \\ 0.0000 & 0.0000 & 0.0000 & 10.3054 & 0.0000 & -3.5775 \\ -6.5343 & -1.0204 & -1.6290 & 0.0000 & 11.7807 & 0.0000 \\ 0.0000 & 0.0000 & 0.0000 & -3.5775 & 0.0000 & 15.7314 \end{pmatrix}.$$

The relative difference between upscaled and rotated Backus solution in Frobenius norm is

$$\frac{\|\mathbb{C}_{Upscaled} - \mathbb{C}_{Rotated}\|_F}{\|\mathbb{C}_{Rotated}\|_F} = 0.0033.$$

The reason why there is a difference between the upscaled and analytically computed tensor, is due to numerical truncation errors in the computations and lack of perfect periodicity in the model (visible for an observant eye in figure 8).The error is undoubtedly small enough to conclude that the upscaling method predicted the elastic tensor correctly for this model.

From these tests it is inferred that the method also will upscale more complex geometries correctly.

Chapter 5

Projection onto a higher symmetry

The outputs from the numerical implementation have in general triclinic symmetry, e.g. 21 free parameters. In some cases one may assume that the result has a higher symmetry, i.e. the elastic modulus can be described by fewer free parameters. An example of this is for a layered medium with TI or isotropic layers where the result should be TI symmetric (or close to TI symmetric for non perfect layering). In such cases, one can find the projection of the elasticity tensor onto a certain symmetry, i.e. the closest elastic tensor of arbitrary symmetry to an elasticity tensor of lower symmetry. The projections are done with respect to the Frobenius norm given in equation (17).

As shown in [10], the Frobenius norm is not invariant under inversion, i.e. $\|\mathbb{C}\|_F \neq \|\mathbb{C}^{-1}\|_F$. However, this norm is simple to work with and in this case good enough since the purpose is just to get an idea if the result is (approximately) of a higher symmetry than the seemingly triclinic. Projections with respect to other norms are for example presented in [10].

In rock physics, isotropy and transverse isotropy are widely used assumptions/approximations and projections onto these are therefore considered here.

5.1 Isotropic projection

The isotropic projection $\mathbb{C}_{Iso}$ of an arbitrary elasticity modulus $\mathbb{C}$ is given by

$$\mathbf{C}_{Iso}(\kappa,\mu) = \begin{pmatrix} \kappa+\frac{4}{3}\mu & \kappa-\frac{2}{3}\mu & \kappa-\frac{2}{3}\mu & 0 & 0 & 0 \\ \kappa-\frac{2}{3}\mu & \kappa+\frac{4}{3}\mu & \kappa-\frac{2}{3}\mu & 0 & 0 & 0 \\ \kappa-\frac{2}{3}\mu & \kappa-\frac{2}{3}\mu & \kappa+\frac{4}{3}\mu & 0 & 0 & 0 \\ 0 & 0 & 0 & \mu & 0 & 0 \\ 0 & 0 & 0 & 0 & \mu & 0 \\ 0 & 0 & 0 & 0 & 0 & \mu \end{pmatrix}$$

with $\mathbf{C}_{Iso}$ being the 6×6 matrix representation of $\mathbb{C}_{Iso}$ and where κ and μ minimize

$$\|\mathbb{C} - \mathbb{C}_{Iso}(\kappa,\mu)\|_F,$$

where $\|\cdot\|_F$ is the Frobenius norm (17).

Given an elastic modulus $\mathbb{C}$ with 6×6 representation $\mathbf{C}$ of arbitrary symmetry, κ and μ are found by setting the derivatives of

$$\|\mathbb{C} - \mathbb{C}_{Iso}(\kappa,\mu)\|_F \tag{28}$$

with respect to κ and μ equal to zero

$$\begin{aligned} \frac{\partial}{\partial\kappa}\|\mathbb{C} - \mathbb{C}_{Iso}(\kappa,\mu)\|_F &= 0 \\ \frac{\partial}{\partial\mu}\|\mathbb{C} - \mathbb{C}_{Iso}(\kappa,\mu)\|_F &= 0. \end{aligned}$$

to find the extremal points. In terms of a_1, a_2 and a_3 defined as

$$\begin{aligned} a_1 &= C_{11} + C_{22} + C_{33} \\ a_2 &= C_{12} + C_{13} + C_{23} \\ a_3 &= C_{44} + C_{55} + C_{66}. \end{aligned}$$

where $[C_{ij}]_{i,j=1}^{3}$ are the entries of $\mathbf{C}$,

$$\begin{aligned} \frac{\partial}{\partial\kappa}\|\mathbb{C} - \mathbb{C}_{Iso}(\kappa,\mu)\|_F &= -2\,(a_1 - 3\kappa - 4\mu) - 4\,(a_2 - 3\kappa + 2\mu) \\ \frac{\partial}{\partial\mu}\|\mathbb{C} - \mathbb{C}_{Iso}(\kappa,\mu)\|_F &= -\frac{8}{3}\,(a_1 - 3\kappa - 4\mu) + \frac{8}{3}\,(a_2 - 3\kappa + 2\mu) \\ &\quad - 8\,(a_3 - 3\mu) \end{aligned}$$

and the extremal points are given by the equations

$$\begin{aligned} -2\left(a_1 - 3\kappa - 4\mu\right) - 4\left(a_2 - 3\kappa + 2\mu\right) &= 0 \\ -\frac{8}{3}\left(a_1 - 3\kappa - 4\mu\right) + \frac{8}{3}\left(a_2 - 3\kappa + 2\mu\right) - 8\left(a_3 - 3\mu\right) &= 0. \end{aligned}$$

Solving these yields

$$\begin{aligned} \kappa &= \frac{C_{11} + C_{22} + C_{33} + 2\left(C_{23} + C_{13} + C_{12}\right)}{9} \\ \mu &= \frac{C_{11} + C_{22} + C_{33} - C_{23} - C_{13} - C_{12}}{15} + \frac{C_{44} + C_{55} + C_{66}}{5}. \end{aligned} \tag{29}$$

Given an elasticity tensor $\mathbf{C}$, $\|\mathbb{C} - \mathbb{C}_{Iso}(\kappa, \mu)\|_F$ is continuous in both κ and μ. It is obvious from equation (17) that

$$\begin{aligned} \lim_{\kappa \to \infty} \|\mathbb{C} - \mathbb{C}_{Iso}(\kappa, \mu)\|_F &= \infty \\ \lim_{\mu \to \infty} \|\mathbb{C} - \mathbb{C}_{Iso}(\kappa, \mu)\|_F &= \infty, \end{aligned}$$

hence the values for κ and μ found above are the global minima of (28) and represent an isotropic projection of $\mathbb{C}$.

The wave velocities corresponding to $\mathbb{C}$ are given by the Christoffel equation (10) and are in general direction dependant. The velocities corresponding to the isotropic projection $\mathbb{C}_{Iso}$ of $\mathbb{C}$ are given by

$$\begin{aligned} V_{P_{Iso}} &= \sqrt{\frac{\kappa + \frac{4}{3}\mu}{\rho}} \\ &= \sqrt{\frac{\frac{1}{15}\left[3(C_{11} + C_{22} + C_{33}) + 2(C_{23} + C_{31} + C_{12}) + 4(C_{44} + C_{55} + C_{66})\right]}{\rho}} \\ V_{S_{Iso}} &= \sqrt{\frac{\mu}{\rho}} \\ &= \sqrt{\frac{\frac{1}{15}\left[C_{11} + C_{22} + C_{33} - C_{23} - C_{31} - C_{12} + 3(C_{44} + C_{55} + C_{66})\right]}{\rho}}. \end{aligned}$$

Another possibility could be projection with respect to minimizing the mean square difference in velocities, i.e. minimizing the distances between the Christoffel matrices for $\mathbb{C}$ and $\mathbb{C}_{Iso}$. This has been done by Fedorov [10] and the resulting velocities are equal to those one gets by averaging the velocities over all directions. These are also exactly equal to those found here by Euclidean projection of the stiffness tensor.

5.2 TI projection

The transversely isotropic projection $\mathbf{C}_{TI}$ of an arbitrary $\mathbf{C}$ can be expressed in terms of 5 independent components

$$\mathbf{C}_{TI}(A,B,C,D,E) = \begin{pmatrix} A & A-2E & B & 0 & 0 & 0 \\ A-2E & A & B & 0 & 0 & 0 \\ B & B & C & 0 & 0 & 0 \\ 0 & 0 & 0 & D & 0 & 0 \\ 0 & 0 & 0 & 0 & D & 0 \\ 0 & 0 & 0 & 0 & 0 & E \end{pmatrix}$$

where A, B, C, D and E are such that

$$\|\mathbb{C} - \mathbb{C}_{TI}(A,B,C,D,E)\|_F \tag{30}$$

is minimized, $\|\cdot\|_F$ being the Frobenius norm and the connection between this to the 6×6 representation $\mathbf{C}$ is given in equation (17).

As for the isotropic projection, one wants to find the extremal points of $\|\mathbb{C} - \mathbb{C}_{TI}(A,B,C,D,E)\|_F$ in order to determine the parameters A to E.

Differentiating $\|\mathbb{C} - \mathbb{C}_{TI}(A,B,C,D,E)\|_F$ with respect to A, B, C, D and E and setting these to zero yields

$$\begin{aligned}
0 &= \frac{\partial}{\partial A}\|\mathbb{C} - \mathbb{C}_{TI}(A,B,C,D,E)\|_F \\
\Rightarrow 0 &= -2(C_{11} - A) - 4(C_{12} - A + 2E) - 2(C_{22} - A) \\
0 &= \frac{\partial}{\partial B}\|\mathbb{C} - \mathbb{C}_{TI}(A,B,C,D,E)\|_F \\
\Rightarrow 0 &= -4(C_{13} - B) - 4(C_{23} - B)) \\
0 &= \frac{\partial}{\partial C}\|\mathbb{C} - \mathbb{C}_{TI}(A,B,C,D,E)\|_F \\
\Rightarrow 0 &= -2(C_{33} - C) \\
0 &= \frac{\partial}{\partial D}\|\mathbb{C} - \mathbb{C}_{TI}(A,B,C,D,E)\|_F \\
\Rightarrow 0 &= 4\left(-2(C_{44} - D) - 2(C_{55} - D)\right) \\
0 &= \frac{\partial}{\partial E}\|\mathbb{C} - \mathbb{C}_{TI}(A,B,C,D,E)\|_F \\
\Rightarrow 0 &= 8(C_{12} - A + 2E) - 8(C_{66} - E).
\end{aligned}$$

Solving these yields the extremal points A to E

$$\begin{aligned}
A &= \frac{1}{2}c_{66} + \frac{1}{4}C_{12} + \frac{3}{8}(C_{11} + C_{22}) \\
B &= \frac{C_{13} + C_{23}}{2} \\
C &= C_{33} \\
D &= \frac{c_{44} + C_{55}}{2} \\
E &= \frac{1}{2}c_{66} + \frac{1}{4}C_{12} + \frac{1}{8}(C_{11} + C_{22}).
\end{aligned}$$

As for the isotropic case, the same argument yields according to whether the found TI constants correspond to the global minimum of $\|\mathbb{C} - \mathbb{C}_{TI}(A, B, C, D, E)\|_F$. For a given elastic tensor $\mathbf{C}$, the distance in (30) is continuous in A, B, C, D and E respectively (when keeping the others fixed) and (30) tends to infinity when either one of A to E tends to infinity. Hence one knows that the constants found minimize the Euclidean distance between the original triclinic tensor $\mathbb{C}$ and the TI projection $\mathbb{C}_{TI}$.

The velocities corresponding to the TI projection become

$$\begin{aligned}
V_P(\theta) &= \sqrt{\frac{A\sin^2(\theta) + C\cos^2(\theta) + D + \sqrt{M(\theta)}}{2\rho}} \\
V_{SV}(\theta) &= \sqrt{\frac{A\sin^2(\theta) + C\cos^2(\theta) + D - \sqrt{M(\theta)}}{2\rho}} \\
V_{SH} &= \sqrt{\frac{E\sin^2(\theta) + D\cos^2(\theta)}{\rho}} \\
M(\theta) &= \left[(A - D)\sin^2(\theta) - (C - D)\cos^2(\theta)\right]^2 + (B + D)\sin^2(2\theta).
\end{aligned}$$

A generalization of Fedorov's approach by minimizing with respect to the average for all propagation directions of the Christoffel equations is identical to the Euclidean minimization [10].

5.3 Basis dependent projection

The projections above are for elasticity tensors $\mathbb{C}$ in their original basis. One could imagine that there is another basis that would give a smaller $\|\mathbb{C} - \mathbb{C}_{Proj}\|_F$, i.e. one could minimize

$$\|\mathbb{C}(\mathrm{d}) - \mathbb{C}_{Proj}(\mathrm{d}, \mathbf{X})\|_F$$

with respect to d and $\mathbf{X}$ where d is the basis in which $\mathbb{C}$ and $\mathbb{C}_{Proj}$ are given and $\mathbf{X}$ represents the free parameters of the projection, i.e. κ and μ for isotropic projection and A to E for TI projection. In Voigt notation this is eqivalent to minimize

$$\|K\mathbf{C}K^T - K\mathbf{C}_{Proj}(\mathbf{X})K^T\|_F = \|K\mathbf{C}K^T - \mathbf{C}^*_{Proj}(\mathbf{X})\|_F \tag{31}$$

with respect to K and $\mathbf{X}$, where K is the rotation matrix defined in (20). The projection $\mathbf{C}^*_{Proj}$ then has to be rotated back to the original basis to obtain $\mathbf{C}_{Proj}$ which will alter the initial form of the tensor, but it will have the same number of free parameters.

5.3.1 Isotropic projection is independent of basis

For the isotropic case,

$$K\mathbf{C}_{Iso}(\mathbf{X})K^T = \mathbf{C}_{Iso}(\mathbf{X}),\ \forall K,$$

i.e. the isotropic projection is invariant under rotation. Euclidean minimization of the Christoffel matrix is equivalent to Euclidean projection of the elastic modulus [10], i.e.

$$\mathbf{C}_{Iso} = \hat{\rho}\begin{pmatrix} V_{P_{avg}}^2 & V_{P_{avg}}^2 - 2V_{S_{avg}}^2 & V_{P_{avg}}^2 - 2V_{S_{avg}}^2 & 0 & 0 & 0 \\ V_{P_{avg}}^2 - 2V_{S_{avg}}^2 & V_{P_{avg}}^2 & V_{P_{avg}}^2 - 2V_{S_{avg}}^2 & 0 & 0 & 0 \\ V_{P_{avg}}^2 - 2V_{S_{avg}}^2 & V_{P_{avg}}^2 - 2V_{S_{avg}}^2 & V_{P_{avg}}^2 & 0 & 0 & 0 \\ 0 & 0 & 0 & V_{S_{avg}}^2 & 0 & 0 \\ 0 & 0 & 0 & 0 & V_{S_{avg}}^2 & 0 \\ 0 & 0 & 0 & 0 & 0 & V_{S_{avg}}^2 \end{pmatrix}$$

where $V_{P_{avg}}$ and $V_{S_{avg}}$ are the average wave velocities over all directions ($V_{S_{avg}}$ being the average of the two S waves). Since the average is over all directions, $V_{P_{avg}}$ and $V_{S_{avg}}$ are invariant under rotation of $\mathbb{C}$, i.e.

$$\underset{K,\mu}{\operatorname{argmin}}\|K\mathbf{C}K^T - \mathbf{C}_{Iso}(K,\mu)\|_F^2 = \underset{K,\mu}{\operatorname{argmin}}\|\mathbf{C} - \mathbf{C}_{Iso}(K,\mu)\|_F^2$$

for all possible rotation matrices K.

A perhaps easier way to see this, is by realizing that changing the propagation direction and rotating the tensor is invariant. Keeping the tensor fixed and changing the propagation direction is relatively the same thing as keeping the propagation direction fixed and rotating the tensor (physically rotating the medium). Then since Euclidean isotropic projection is equal to averaging velocity over all orientations, this must be invariant under tensor rotation.

5.3.2 A basis dependent TI projection

The analytical procedure to find the minimum of (31) with respect to both direction K and projection variables X, would be to differentiate (31) with respect to all the variables in K and X and set these to zero in order to determine the extremal points. Then one could compare the value of (31) for all these extremal points to find the global maximum and minimum.

It is however easier to do this numerically by discretizing with respect to space. First one finds the TI projection described in section 5.2 for a discrete set of rotations of $\mathbb{C}$. The projection from the rotation that yields the closest $\mathbb{C}_{TI}$ is then chosen as the final projection.

The set of rotated elasticity tensors $K\mathbf{C}K^T$ can be seen in light of the set of rotation matrices A (18). A rotation matrix can alternatively be described in terms of three angles (for example Euler angles) [8]. A regular "grid" of rotations is therefore defined by a regular grid in the space of the three Euler angles.

Since TI symmetric elasticity tensors have a symmetry axis, here $\boldsymbol{n}_3$, a basis change with fixed $\boldsymbol{n}_3$ will not change the projected $\mathbb{C}_{TI}$. Thus it is enough to look at a discrete set of $\boldsymbol{n}_3$ basis vectors.

To find this set, one can discretize the surface of a unit sphere and let the set of $\boldsymbol{n}_3$ vectors be equal to the set vectors from the origin to the nodes on the discrete sphere surface. Here the sphere surface was discretized into triangles by starting with a icosahedron and then subdivide each triangle face by a factor of 4 a suitable number of times. A discritization of the unit sphere is shown in figure 9.

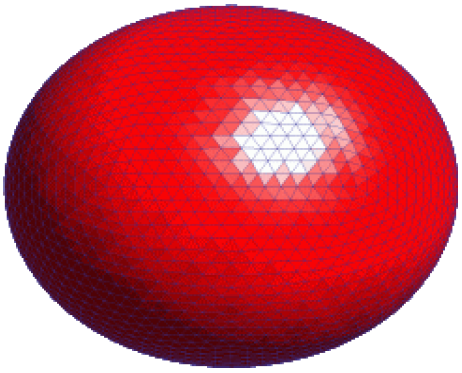

Figure 9: *Discretization of the surface of a unit sphere.*

Chapter 6

Elastic moduli visualization

From the Christoffel equation (10) one can see that there is a close relationship between the elasticity tensor and the wave speeds. The elastic moduli can therefore be visualized through their corresponding wave velocities. A 3D visualization of the wave speeds for the periodic model where the layers are isotropic with bulk and shear moduli

$$K_{\text{Blue layer}} = 5,\ \mu_{\text{Blue layer}} = 5$$
$$K_{\text{Red layer}} = 30,\ \mu_{\text{Red layer}} = 30,$$

is shown in figure 10. The blue surface is the P-wave velocities at the different directions, while the green and red surfaces are the S-wave velocities. In this case it is easy to see the connection between the shape of the surfaces in figure 10a and the orientation of the layers in the model 10b.

On paper, a projection (in for instance the xz or yz plane) of the $3D$ surfaces in figure 10a can be easier to interpret. An example of this for the periodic model is shown in figure 11 with and without the corresponding Voigt and Reuss bounds in the background. Here both rock types are isotropic so the bounds are valid (see section 3.1.1), and one sees that the velocities are always between the bounds. Vertically the P wave velocitiy is equal to the Reuss bound while horizontally in the xz projection, i.e. for propagation direction $\begin{pmatrix}1 & 0 & 0\end{pmatrix}$, it is equal to the Voigt bound. For propagation direction $\begin{pmatrix}1 & 0 & 0\end{pmatrix}$ one of the S waves are equal to the Voigt bound while the other is equal to the Reuss bound. In the yz plane at an angle $\sim \frac{\pi}{4}$ one of the S waves is equal to the Reuss bound while the other is

equal to the Voigt bound and for an angle $\sim \frac{3\pi}{4}$ both S waves are equal to the Reuss bound.

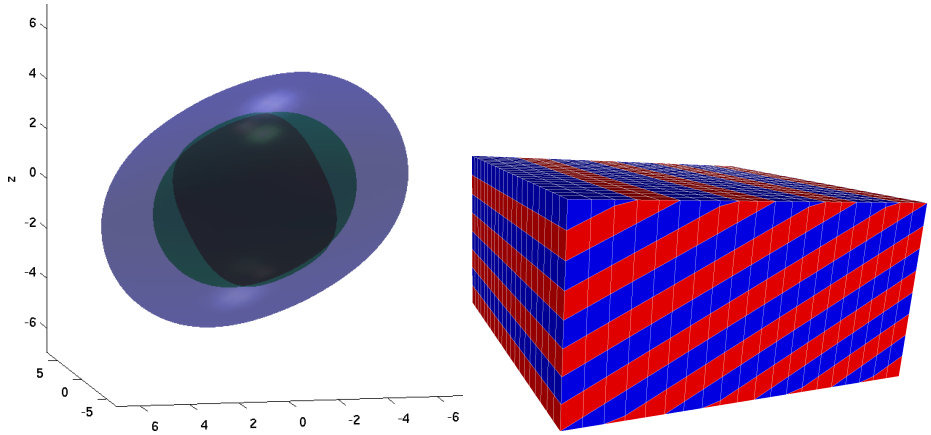

(a) *The blue surface is V_P, the red and green are the two S waves.*

(b) *Periodic model*

Figure 10: *3D visualization (a) of the wave velocities for the model in (b).*

In both the 2D and 3D visualizations, it may seem like the S wave velocities are not always smooth. This is purely a plotting artifact as the surfaces should cross, not just touch. In the plotting routine the velocities are found by finding the eigenvalues of the Christoffel matrix for discrete directions. The method to separate the different waves is by sorting the eigenvalues by size. V_P is always the fastest while it changes which of the S waves is the fastest.

For a TI medium with symmetry axis in the vertical direction (z), the projection in any hz plane, where h is an axis lying in the xy plane, is equal. For approximately TI symmetric models, the visualization is done by averaging over the azimuth angle. (This would be identical to computing the velocity for the TI projection). An example of this is shown in figure 12. This kind of plot shows the vertical versus horizontal anisotropy. Note that the plots in figure 12 are with a different model and with different microscopic elasticity data than the previous plots.

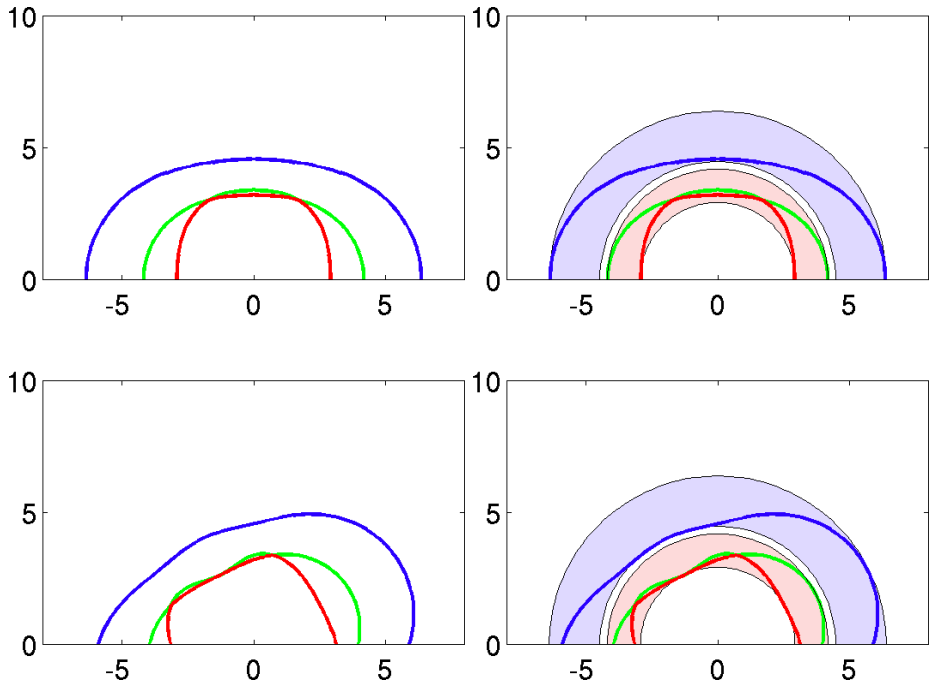

(a) xz *(uppermost) and* yz *projections* **(b)** *Same as figure* (a) *but with the Voigt and Reuss bounds in the background.*

Figure 11: *2D projections of figure 10a in the* xz *and* yz *planes. In (b) these are shown together with the Voigt and Reuss bounds. The blue graph is* V_P *while the two others are the two* S *wave velocities.*

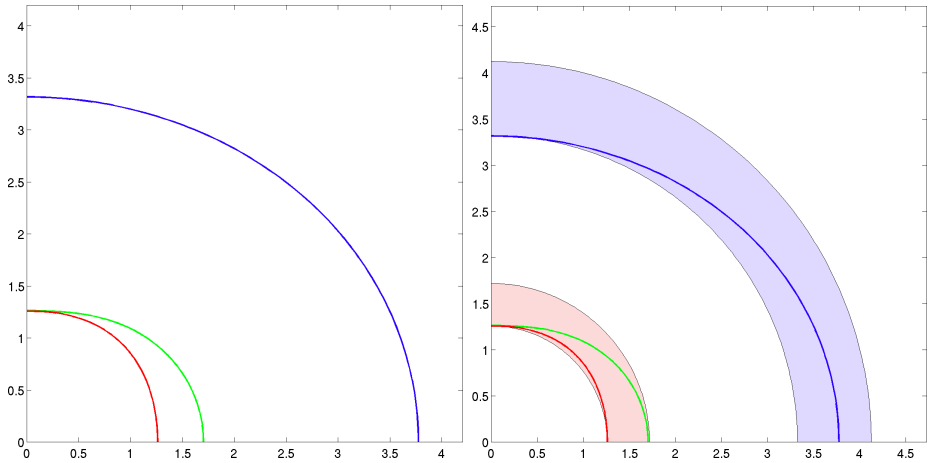

(a) *Wave velocities as a funciton of dip angle*

(b) *Same as in* (a) *but with Voigt and Reuss bounds.*

Figure 12: *Example of wave velocity in the hz plane, i.e. in the vertical vs an average in the horizontal plane. Blue graph is P wave velocity, the other two are S wave velocities.*

Chapter 7

Geometrical effects

For permeability, geometrical effects play an important role in the upscaled result [5], i.e. if a low permeable shale layer with no holes goes through an entire model, the model is close to impermeable across the layer, while if the shale is scattered throughout the model in non-connected patches, fluids can easiliy flow around the shale. Mathematically permeability upscaling is a corner case of elasticity upscaling when all components but the upper left 3×3 submatrix are 0. Analogue to Hooke's law (4) one has Darcy's law

$$u = -\mathbf{K}\nabla P$$

where u is the phase filtration velocity and ∇P is the pressure gradient for permeability. With strain ε analogue to pressure gradient ∇P and stress σ analogue to phase filtration velocity, the elasticity modulus $\mathbf{C}$ is analogue to permeability K. Therefore it is interesting whether the same geometrical effects make similar impact for elasticity. Mathematically the answer is yes, but there is a question whether the realistic magnitudes are important, and if there exists additional effects due to the generalization from permeability to elasticity.

First in this section, three models with the same shale amount (50%) but different geometries are compared. The first model is an imitation of the rock formation created by tides shown in figure 13b. The second is a model with two layers, all the shale on top and all the sand at the bottom illustrated in figure 13a. The last one is a model with regular cells and where each cell has a probability of 50% to contain shale. The last model is highly unrealistic, but it is interesting to compare the results on this model with realistic ones.

Next the ratio between shale versus sand is investigated by determining the anisotropy as function of shale content. This is also done for three different geometry types, imitation of tidal composition, perfectly layered and random.

7.1 Comparing three different geometries

Three models with the same amount of shale (50%), but with different geometries were used to investigate the geometric effects. One model is simply two layers with equal thickness where one layer is shale and the other is sand. Another is a regular model where the shale is spread randomly, i.e. each cell has a probability of 50% to contain shale. The last is a model composed using geological "rules", i.e. the model imitates a realistic deposition caused by tides. The models are shown in figure 13.

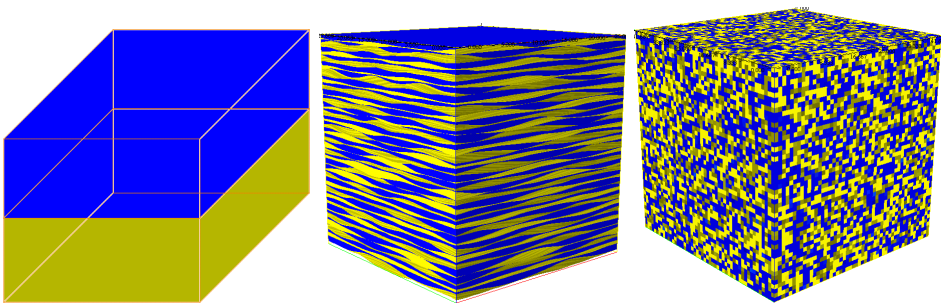

(a) *Shale layer on top of a sand layer.* **(b)** *Composition caused by tides.* **(c)** *Randomly spread shale.*

Figure 13: *Three different models which all contain* 50% *sand and* 50% *shale.*

7.1.1 Isotropic shale

First the upscaling is done on these models with isotropic input for both sand and shale with the following elasticity and density

parameters

$$\begin{aligned} K_{Sand} &= 13 \\ \mu_{Sand} &= 5 \\ \rho_{Sand} &= 2.33 \\ K_{Shale} &= 11.27 \\ \mu_{Shale} &= 9.93 \\ \rho_{Shale} &= 2.4. \end{aligned} \tag{32}$$

The relative Euclidean distances between the upscaled elasticity tensors for the geological model and the two others became

$$\begin{aligned} \frac{\|\mathbb{C}_{Geological} - \mathbb{C}_{Random}\|_F}{\|\mathbb{C}_{Geological}\|_F} &= 0.0876 \\ \frac{\|\mathbb{C}_{Geological} - \mathbb{C}_{Layered}\|_F}{\|\mathbb{C}_{Geological}\|_F} &= 0.0546, \end{aligned}$$

which is not much, but there is a difference. One sees that the elasticity for the layered model, figure 13a, is closer than for the random one, figure 13c, which is reasonable since the geological one, figure 13b, seems to have some kind of (imperfect) layering. One could expect that this result could be extrapolated to similar models, i.e. that models with a layering trend would yield similar results as a perfectly layered model, i.e. one can get fairly good results by using Backus averaging for such models.

The wave velocities for the three models are shown in figure 14. V_P/V_S as a function of angle for the random model, figure 14d, is nearly a straight line which means that this model is almost isotropic. This is confirmed by Euclidean distance between the elastic modulus $\mathbb{C}_{Random}$ and its isotropic projection $C_{Random_{iso}}$,

$$\frac{\|\mathbb{C}_{Random} - \mathbb{C}_{Random_{iso}}\|_F}{\|\mathbb{C}_{Random}\|_F} = 0.0029.$$

which is also expected since any geometrical effect is meant to be smeared out by the randomization. For the other models, one sees a disturbance in the V_P/V_S ratio for about $40°$ dip angle. (For anisotropic mediums the V_P/V_S ratio uses the fastest of the two S waves since this is the one being recorded when measurements are conducted in the laboratory and in sonic logs). The distances for these to isotropy are

$$\begin{aligned} \frac{\|\mathbb{C}_{Geological} - \mathbb{C}_{Geological_{iso}}\|_F}{\|\mathbb{C}_{Geological}\|_F} &= 0.0187 \\ \frac{\|\mathbb{C}_{Layered} - \mathbb{C}_{Layered_{iso}}\|_F}{\|\mathbb{C}_{Layered}\|_F} &= 0.0341, \end{aligned}$$

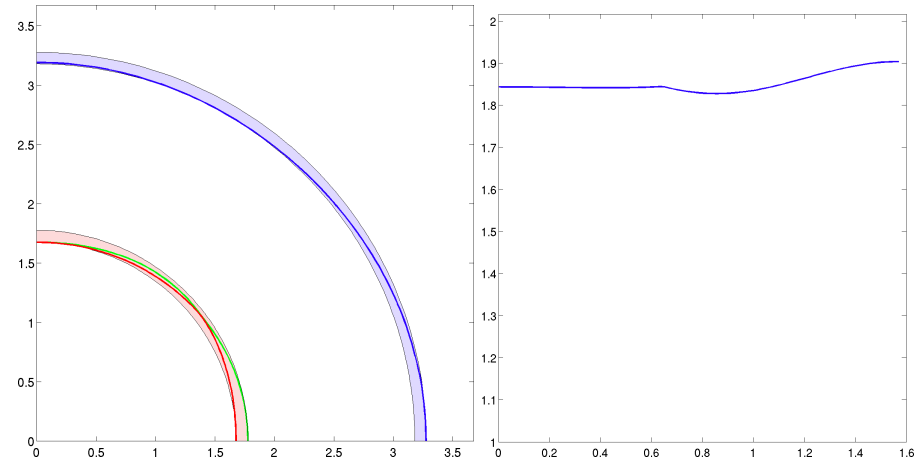

(a) *Two layer model* **(b)** V_P/V_S *versus angle*

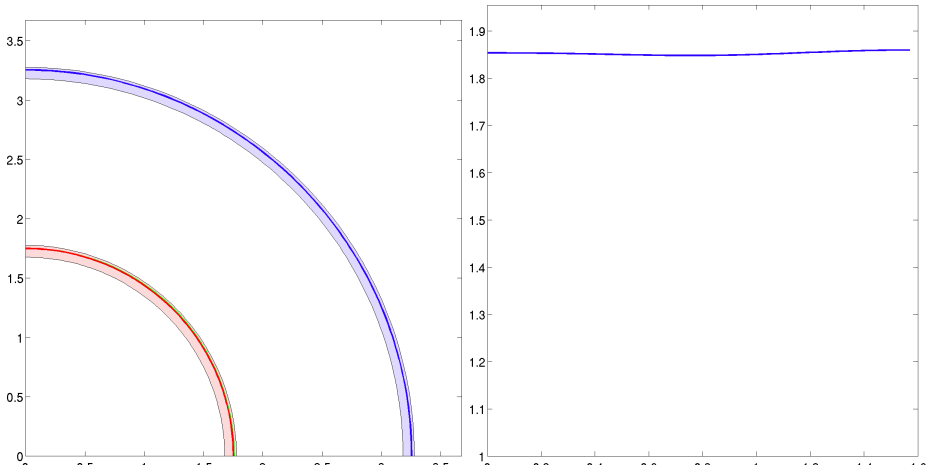

(c) *Random model* **(d)** V_P/V_S *versus angle*

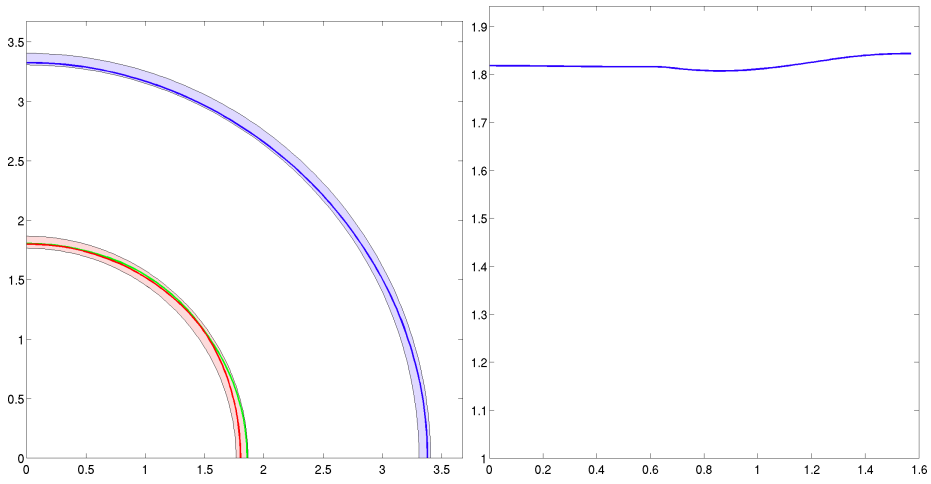

(e) *Geological model* **(f)** V_P/V_S *versus angle*

Figure 14: *Wave velocities and V_P/V_S as function of angle for the layered model in 13a, the random model in 13c and the geological model in 13b with one sand stone type and where the shale is assumed isotropic.*

thus both these models are further from isotropy than the random. The wave velocities for the random model in 14c are close to the upper bound, i.e. the Voigt average would be a good estimate for the elastic modulus in this case.

As one sees in figure 14a, the layered model reaches both bounds and the velocities are being equal to the Reuss average in the vertical direction and equal to the Voigt average for V_P and one of the S waves and equal to the Reuss average for the other in the horizontal direction. Considering V_P and the green S wave, these are exactly analogous to permeability in the vertical and horizontal direction. For permeability one has that this is equal to the arithmetic average (Voigt) along layers and to the harmonic average (Reuss) across layers.

The wave velocities for the geological model is shown in figure 14e and tend to follow the same trends as the layered model, but not as strong since V_P do not reach the upper bound at any point and none of the S wave velocities reach the lower bound.

Since the bounds are computed based on volume fractions only, these are expected to be equal in all three cases. If one looks closely at the bounds in figure 14e compared to figure 14a and 14c, one sees that these do not coincide completely. This is due to the sand fraction in the geological model not being exactly 50% but 50.17%.

The contrasts in properties for the cells is too small to cause any significant impact and for many practical purposes, all three models might be considered approximately isotropic and an averaging technique omitting geometrical differences, for example Voigt, Reuss or the average of these two; Voigt-Reuss-Hill, would often give good enough results.

7.1.2 Anisotropic shale

In reservoirs, shale is usually anisotropic. (All real rocks are usually anisotropic, but for sand for example, the anisotropy is often so weak that this is assumed isotropic). Therefore the upscaling of the three models is also done when the shale is assumed TI symmetric to see if there are any interaction effects between cell scale anisotropy and geometry that affects the upscaled result. In addition there are two different sands. The elastic and density parame-

ters are given by

$$K_1 = 13 \quad K_2 = 18$$
$$\mu_1 = 5 \quad \mu_2 = 10 \tag{33}$$
$$\rho_1 = 2.33 \quad \rho_2 = 2.11$$

(34)

for the sands and

$$\mathbf{C}_{Shale} = \begin{pmatrix} 32 & 8 & 13 & 0 & 0 & 0 \\ 8 & 32 & 13 & 0 & 0 & 0 \\ 13 & 13 & 29 & 0 & 0 & 0 \\ 0 & 0 & 0 & 9 & 0 & 0 \\ 0 & 0 & 0 & 0 & 9 & 0 \\ 0 & 0 & 0 & 0 & 0 & 12 \end{pmatrix} \tag{35}$$
$$\rho_{Shale} = 2.4,$$

for the shale. The velocities and V_P/V_S ratio for the shale are shown in figure 15. The relative Euclidean distances between the upscaled

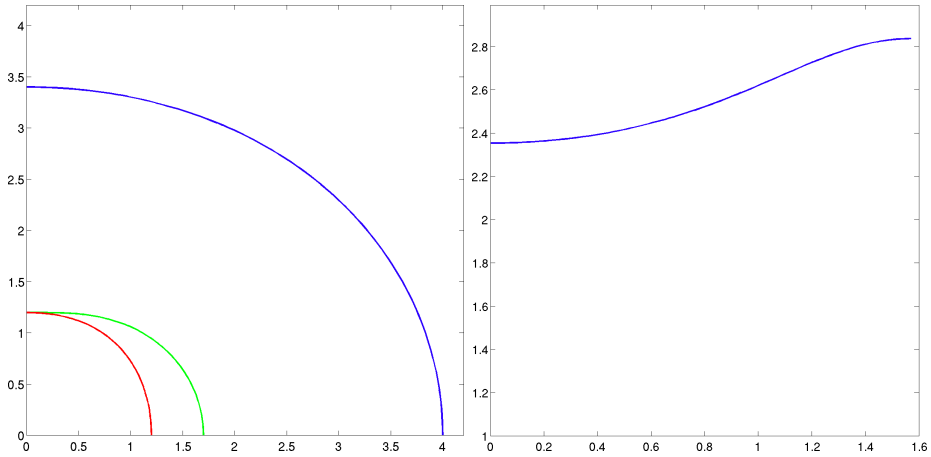

(a) *Wave velocities* **(b)** V_P/V_S *versus angle*

Figure 15: *The wave velocities (a) and V_P/V_S as function of angle (b) for the elastic modulus used as input for shale when this is assumed TI.*

elastic moduli become

$$\frac{\|\mathbb{C}_{Geological} - \mathbb{C}_{Random}\|_F}{\|\mathbb{C}_{Geological}\|_F} = 0.0273$$
$$\frac{\|\mathbb{C}_{Geological} - \mathbb{C}_{Layered}\|_F}{\|\mathbb{C}_{Geological}\|_F} = 0.0173,$$

which is smaller than for the case where the shale was assumed isotropic. It seems that the cell scale anisotropy overshadows the geometrical effects. One can still see that the layered model is closer than the random one. The wave speeds for the different models are shown in figure 16. Even though there is a small difference in the wave speeds, this will in many applications be much smaller than the uncertainty in the input data. The V_P/V_S ratio versus angle plots all shows anisotropy, although, as expected, the anisotropy seems smaller for the random model. V_P/V_S ratio versus angle for the shale is shown in figure 15b. By comparing V_P/V_S for shale in figure 15b and V_P/V_S for the three models in 16a, 16c and 16e, it is evident that the anisotropy introduced on cell level has a strong effect on the upscaled result.

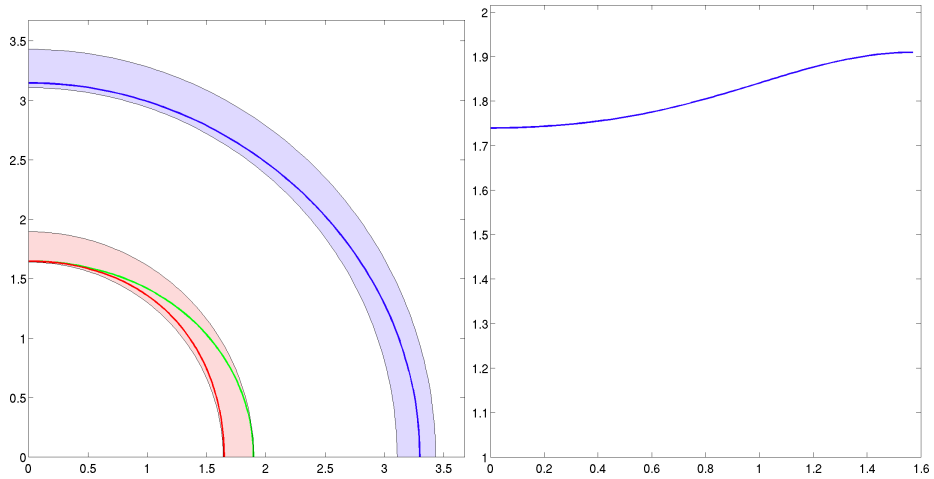

(a) *Two layer model* **(b)** V_P/V_S *versus angle*

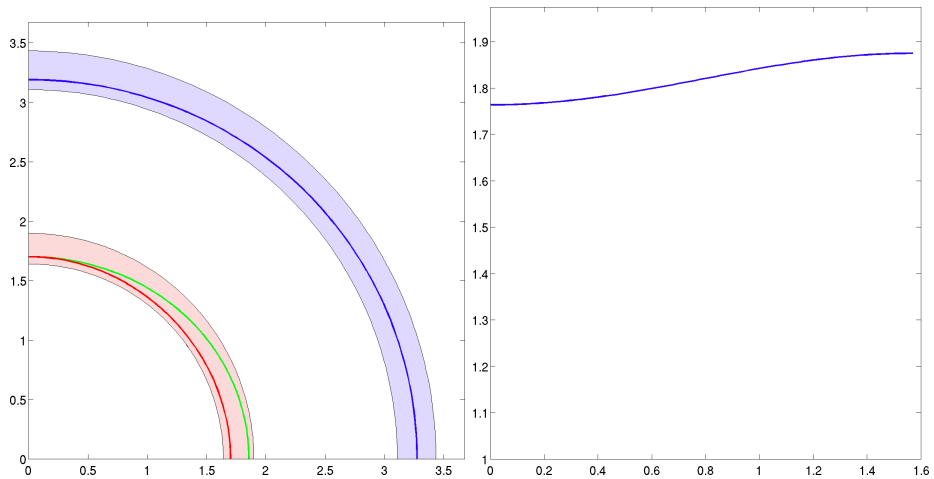

(c) *Random model* **(d)** V_P/V_S *versus angle*

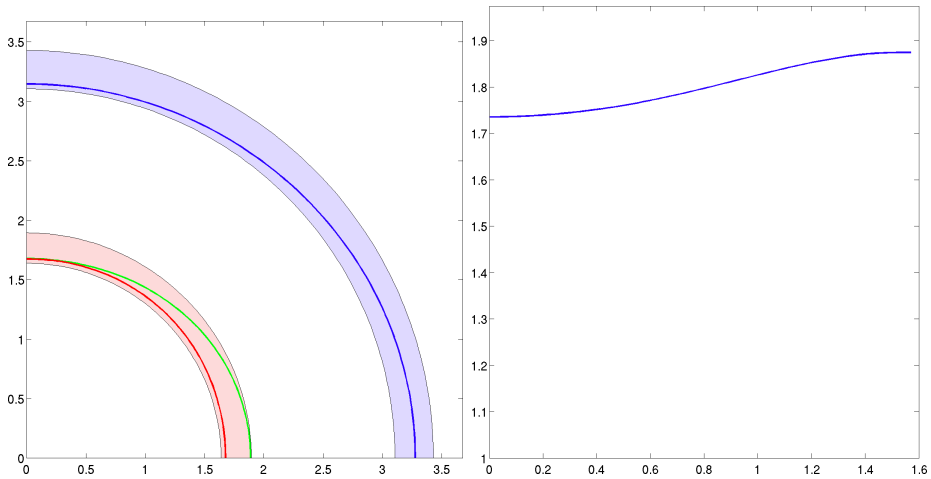

(e) *Geological model* **(f)** V_P/V_S *versus angle*

Figure 16: *Wave velocities and* V_P/V_S *as function of angle for the layered model in 13a, a random model and the geological model in 13b with two different sands and where the shale is assumed* TI*.*

7.2 Shale sensitivity

In section 7.1 one saw that with 50% shale, there were geometrical effects, but that these were not significant enough for many practical objectives. One may want to know if this is the case for all amounts of shale or if this occurs at a certain amount of shale. It would also be interesting to investigate the relationship between anisotropy and shale amount, i.e. the relationship between effective anisotropy and anisotropy of input rock types.

In this section, upscaling on 11 different geological models, 11 layered models and 11 regular models with randomly distributed shale is done with both isotropic and anisotropic shale on cell level. The geological models are shown in figure 17. For the layered models, Backus averaging is used by adjusting the thickness of each layer corresponding to the amount of shale. In the case where the shale is assumed isotropic, there is only one sand type (i.e. the parameters of the two sand types are set equal) and the elastic parameters are those given in (32). When the shale is assumed TI, the two sand types differ and the physical parameters for the rock types in this case are given in (33) and (35).

One common measure for anistotropy is the Thomsen's parameters (26). These can however only be used on TI symmetric elasticity tensors. Another and perhaps more general, suggestion is to measure anisotropy by

$$\frac{\max(\frac{V_P}{V_S}) - \min(\frac{V_P}{V_S})}{\frac{1}{2}\left(\max(\frac{V_P}{V_S}) + \min(\frac{V_P}{V_S})\right)}, \tag{36}$$

i.e. the biggest V_P/V_S ratio discrepancy divided by the average of the maximum and minimum V_P/V_S ratio. The $\max$ and $\min$ are over all directions. Here the distance from isotropy, i.e. $\frac{\|\mathbb{C}-\mathbb{C}_{\text{iso}}\|_F}{\|\mathbb{C}\|_F}$, (36) and Thomsen parameters of the TI projection of the elasticity tensor are used as measures of anisotropy. The reason for introducing both distance from isotropy and the measure in equation (36) is because the V_P/V_S ratio is something that geophysisits is familiar with, while mathematicians are more familiar with norms.

7.2.1 Isotropic shale

For the random models with isotropic shale, figure 18 shows the anisotropy as function of sand percentage. Maximum anisotropy

occurs when there is 60% sand and 40% shale. If the sand and shale have had equal elastic parameters, the maximum would have occurred at 50%, but since shale is stiffer, the maximum is at a lower shale ratio. All anisotropy parameters are small which is reasonable since the models are randomly composed.

Figure 19 shows anisotropy as function of sand percentage for the geological composed models when the shale is assumed isotropic. In this case the anisotropy is in general largest for about 10% sand and 90% shale. γ, which considers shear anisotropy, is largest for about 70% sand and 30% shale. While the anisotropy only depends on volume fractions of the different rock types for random models, there seems to be additional effects in the geological models. Thus, geometry has an impact on anisotropy. It is also interesting to see if the geological models are similar to perfect layered volume equivalents. The anisotropy measures as function of sand percentage for these are shown in figure 20. Also for these it seems that the anisotropy only depend on volume fractions. The anisotropy magnitudes for the layered and geological models are of order $O(10^{-2})$ while for the random models these are of order $O(10^{-3})$.

For the geological model, one may notice that the anisotropy is not zero for 100% sandstone even though the sandstones are equal and isotropic. The divergence from zero is of the same order as the errors found in chapter 4.2, thus this happens because of numerical erros due to non matching cells at the boundaries. The random model has regular cells and the layered has perfect layers, hence these have matching cells at the boundaries and there are no errors due to non periodicity on these.

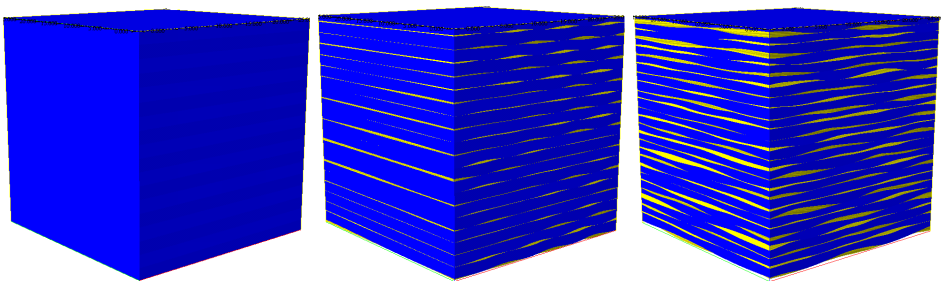

(a) 0% *sand* **(b)** 10% *sand* **(c)** 20% *sand*

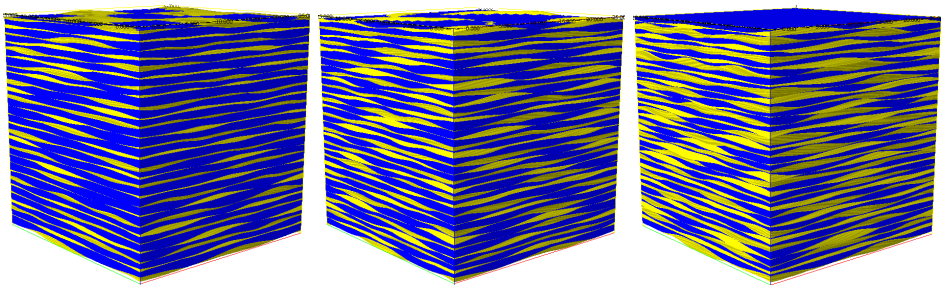

(d) 30% *sand* **(e)** 40% *sand* **(f)** 50% *sand*

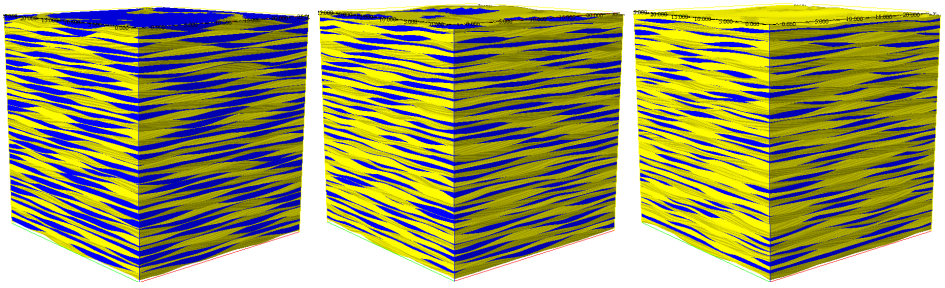

(g) 60% *sand* **(h)** 70% *sand* **(i)** 80% *sand*

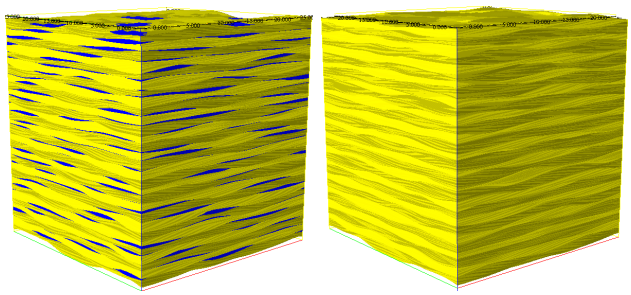

(j) 90% *sand* **(k)** 100% *sand*

Figure 17: *The geolocical tide models for the different amounts of shale.*

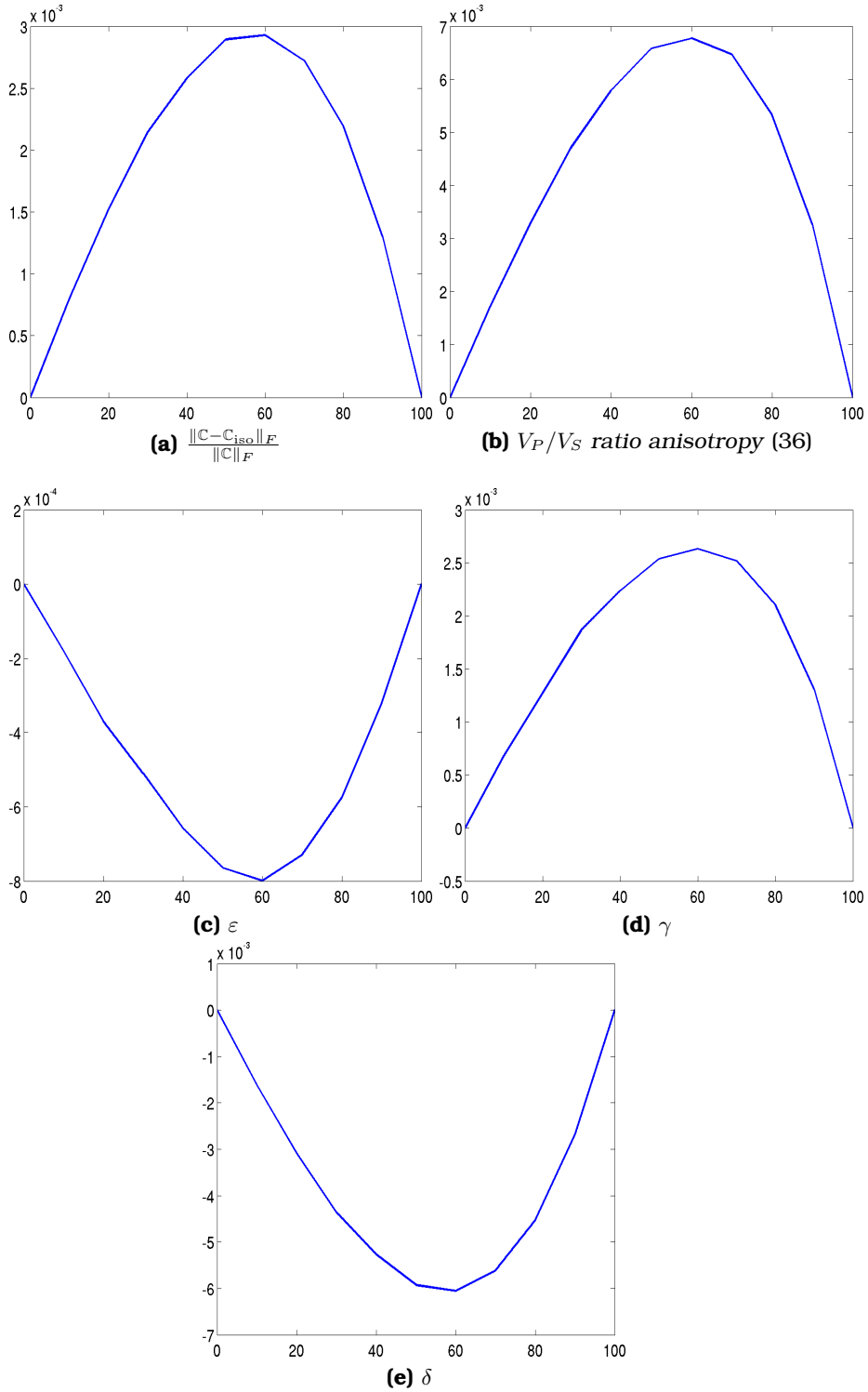

Figure 18: *Anisotropy as function of sand fraction for random distributed shale when this is assumed isotropic. (a) is the distance from isotropy, (b) is the measure in* (36) *while (c), (d), and (e) are the Thomsen parameters for the TI projection.*

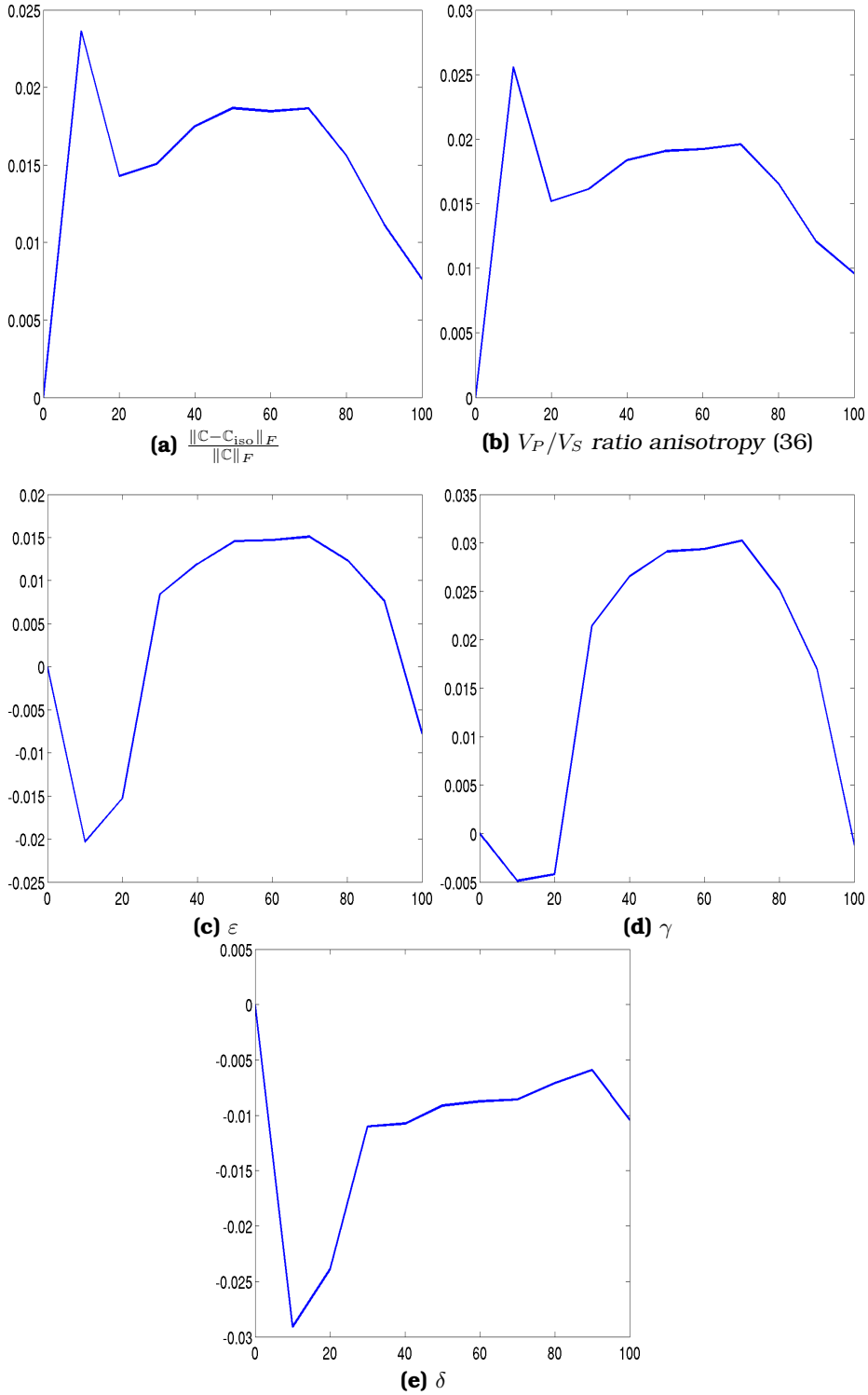

Figure 19: *Anisotropy as function of sand fraction for geological distributed shale, figure 17, when this is assumed isotropic. (a) is the distance from isotropy, (b) is the measure in* (36) *while (c), (d) and (e) are the Thomsen parameters for the* TI *projection.*

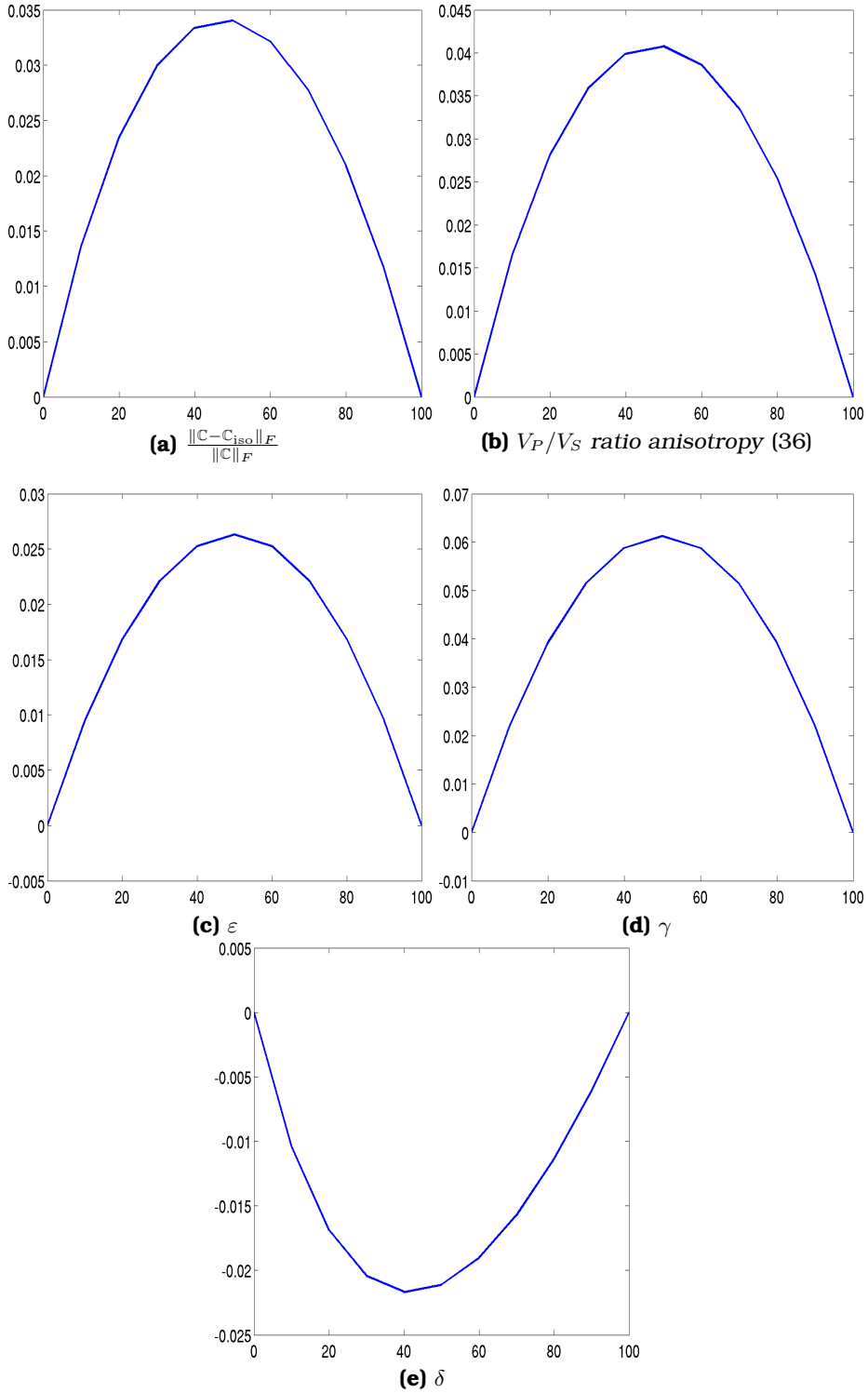

Figure 20: *Anisotropy as function of sand fraction for perfectly layered shale and sand layers when the shale is assumed isotropic. (a) is the distance from isotropy, (b) is the measure in* (36) *while (c), (d) and (e) are the Thomsen parameters for the TI projection.*

7.2.2 Anisotropic shale

Figures 21, 22 and 23 show the anisotropy as function of sand fraction when there are two different sand types and the shale is assumed TI. For the random model, the Thomsen parameters in figures 21c, 21d and 21e are approximately linear while the relative V_P/V_S ratio (36) has a little curvature. This means that the anisotropy is approximately linearly dependent of shale contents in this case and there exists no distinguished shale amount above which the general geometry upscaling is more needed than for example Voigt averaging. The opposite would have been if the anisotropy made a jump at some shale content point, making the geometrical impact more influental above this point.

For the geological model, the anisotropy as function of sand content is shown in figure 22. In all these plots one sees that there is something happening for 90% shale and 10% sand. The maximal V_P/V_S discrepancy is largest for this amount of sand, γ and δ are almost constant for 10% and 20% sand while ε increases from 10% to 20% sand. This behavior may be due to the whole block being TI for 0% sand while when sand is introduced, the elastic modulus is triclinic. From 20% to 100% sand, relative V_PV_S, γ and δ are approximately linear.

For the perfectly layered models, with results shown in figure 23, the anisotropy looks smooth and monotonic. When the amount of sand increases, the effective elasticity tensor comes closer to isotropy. V_P/V_S, ε and γ decrease faster when the amount of sand increases, δ decreases slower when the sand amount increas, while the Frobenius distance between the elasticity tensors is approximately linear. The elastic modulus is however always (at least) TI (see section 3.2) which means that one does not get the same disturbances as for the geological model when the elastic modulus goes from TI to triclinic when sand is added.

By comparing the results from the case when the shale was assumed isotropic and the sands where equal with the case where there where two different sands and the shale was TI, i.e. comparing figures 18, 19 and 20 with figures 21, 22 and 23, one sees that the anisotropy is much larger for the second case and that the shapes of the anisotropy measures are completely different. For the geological model it looks like the geometrical effects one sees in figure 19 could be added to some linear decreasing function to get figure 22. Thus the small scale anisotropy has much larger significance than geometrical differences, at least in this particular case.

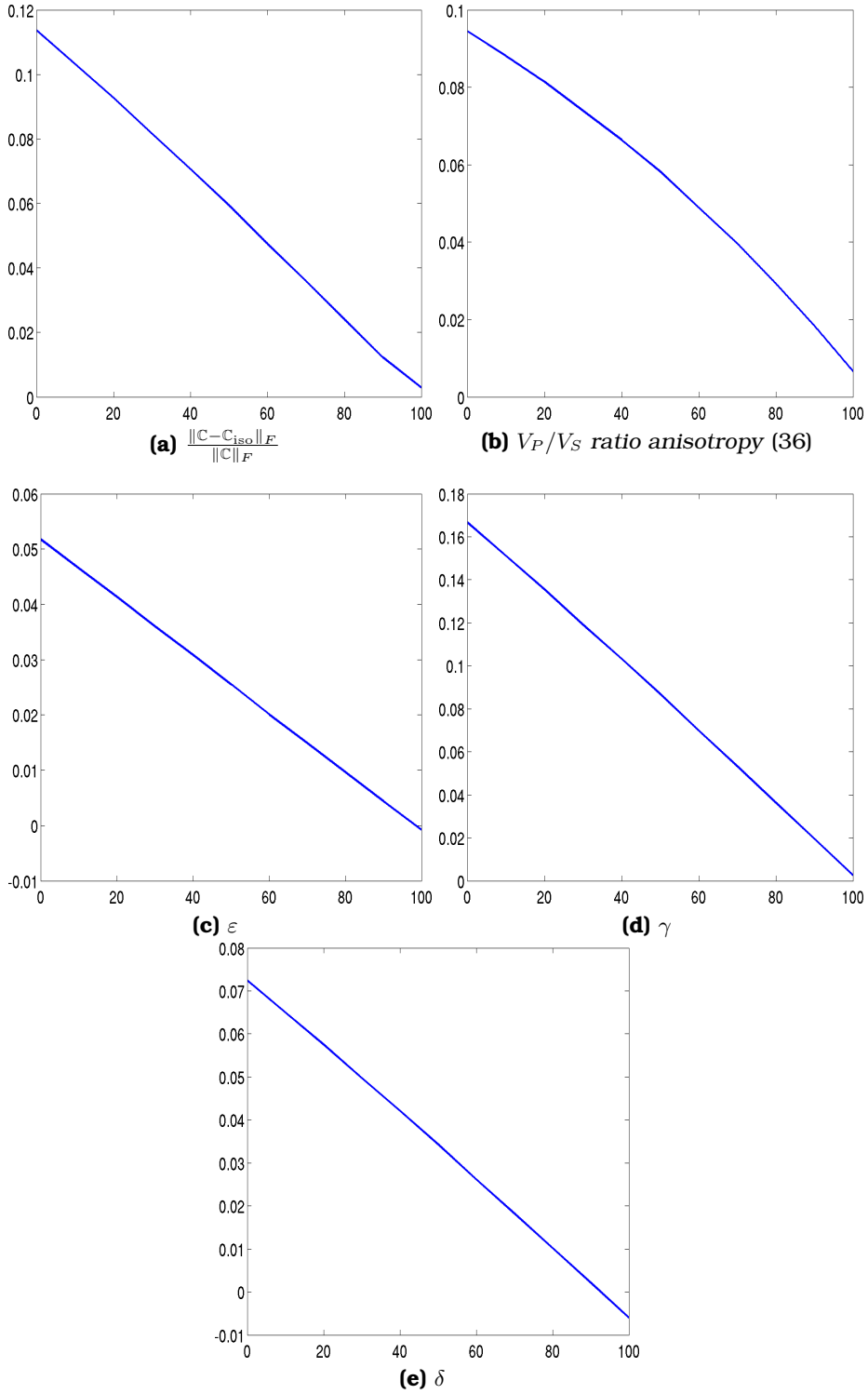

Figure 21: *Anisotropy as function of sand fraction for random distributed shale when the shale is assumed anisotropic. (a) is the distance from isotropy, (b) is the measure in* (36) *while (c), (d) and (e) are the Thomsen parameters for the* TI *projection.*

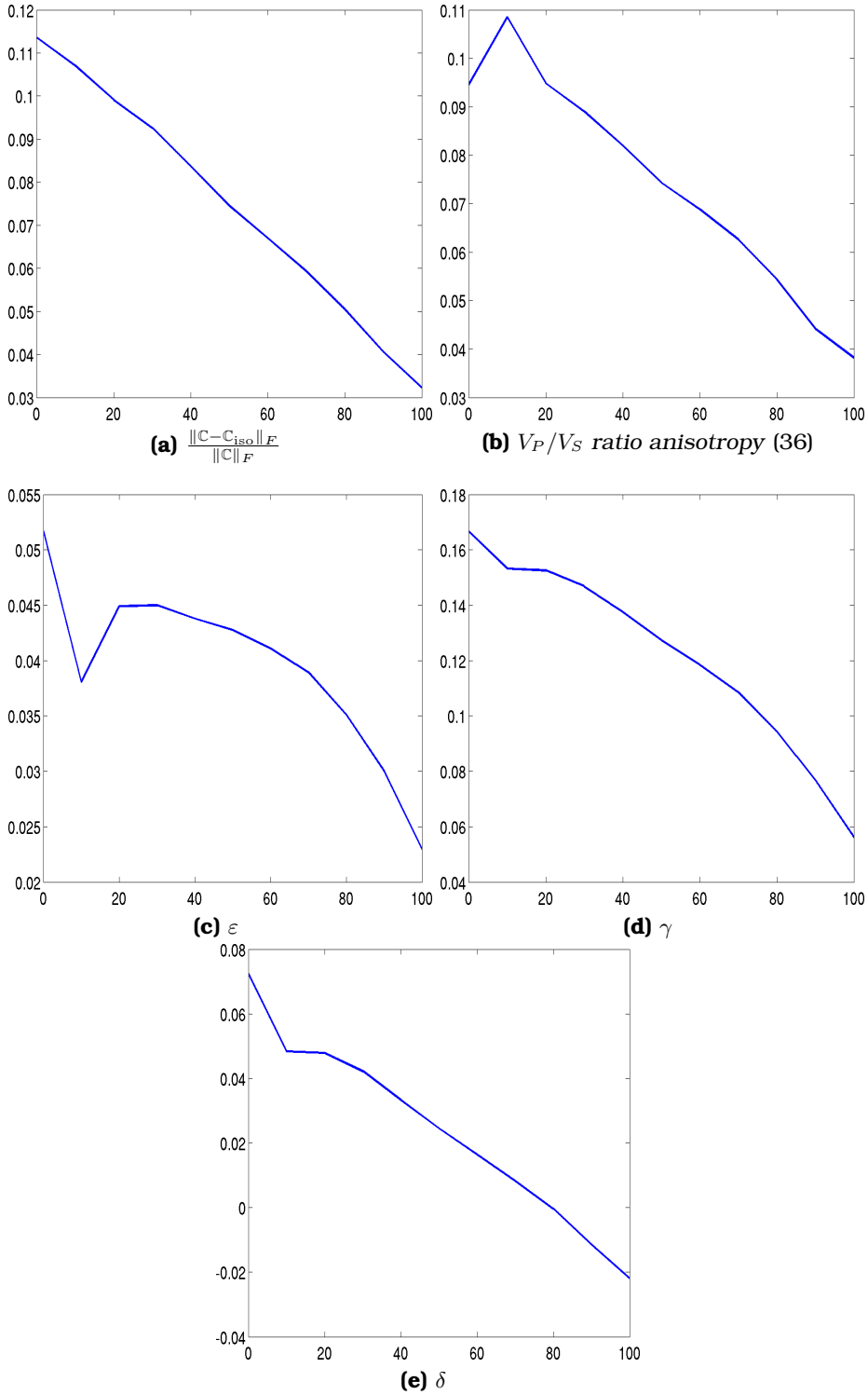

Figure 22: *Anisotropy as function of sand fraction for geological distributed shale, figure 17, when this is assumed anisotropic. (a) is the distance from isotropy, (b) is the measure in* (36) *while (c), (d) and (e) are the Thomsen parameters for the TI projection.*

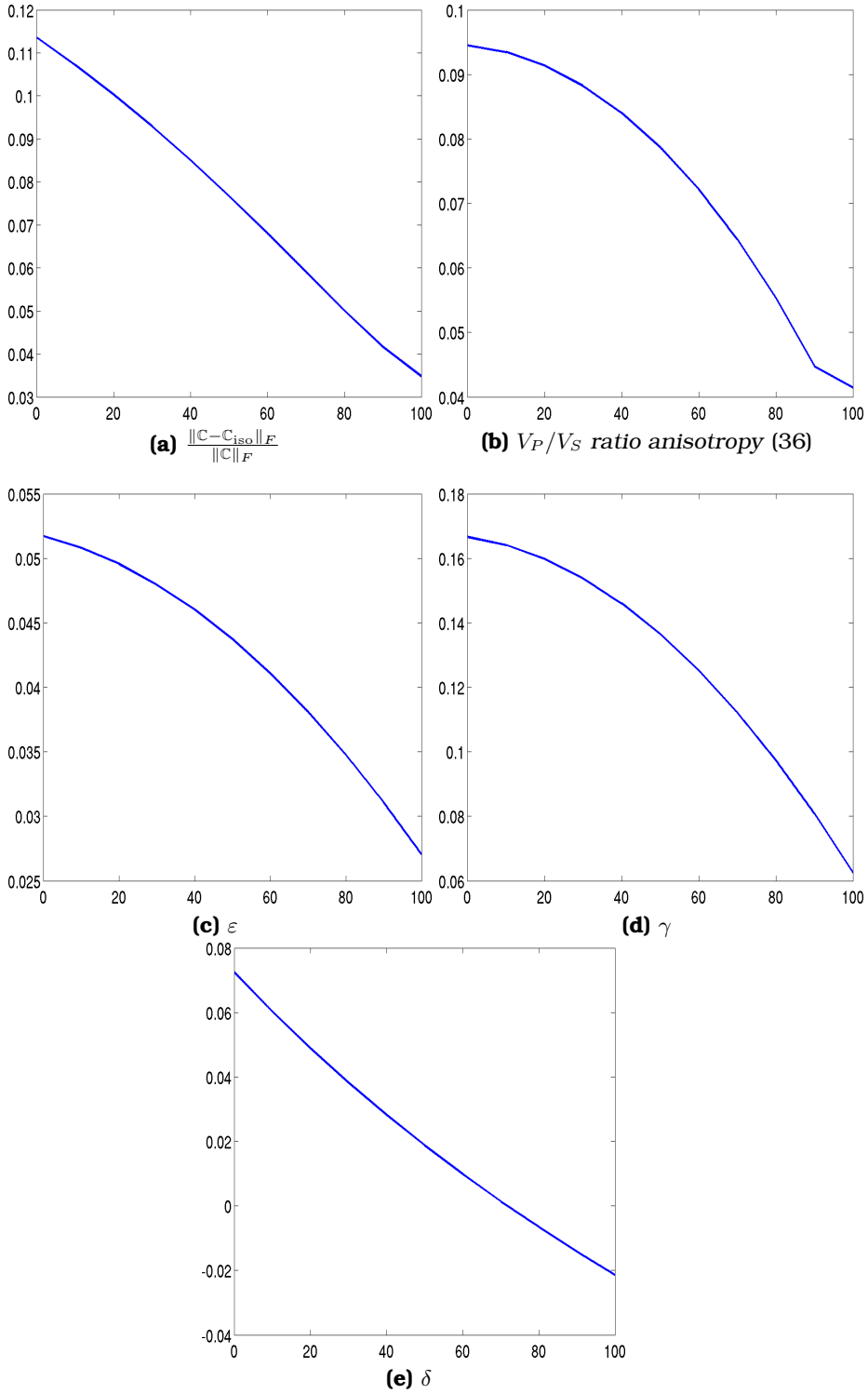

Figure 23: *Anisotropy as function of sand fraction for perfectly layered shale and sand layers when the shale is assumed anisotropic. (a) is the distance from isotropy, (b) is the measure in* (36) *while (c), (d) and (e) are the Thomsen parameters for the TI projection.*

Chapter 8

Upscaling from lamina to lithofacies

In this chapter, the upscaling method is utilized on real reservoir models with realistic input data to get a hint of how large the magnitudes of the geometrical effects are in real reservoirs.

Six lithofacies models from a reservoir at a scale which extends from 20 to 60 cm horizontally from 10 to 30 cm vertically are considered. These models are shown in figure 24 and with data given in table 3.

Model	*Area* (cm^2)	*Height* (cm)	*Sand1* (%)	*Sand2* (%)	*Shale* (%)	*Cells*
1	1600	20	46.5	53.5	0	40847
2	400	30	49.7	47.9	2.4	149794
3	1600	14	31.46	66.88	1.66	234156
4	400	9.8	50.03	48.76	1.21	50033
5	3600	15	13.73	75.17	11.10	247972
6	1600	10	8.12	7.97	83.91	209280

Table 3: Properties of the lithofacies models in figure 24

In these models there are three different rock types, two sands and one shale type. In absence of rock data that origin from laboratory measurements or logs, synthetic data are used. These are data that in a geophysicist opinion could occur in a reservoir. Since this is not a field study of a special production field, it does not matter if the data comes from measurements of the rock compositions that was used to build the models, as long as the data are realistic enough to imitate a real reservoir.

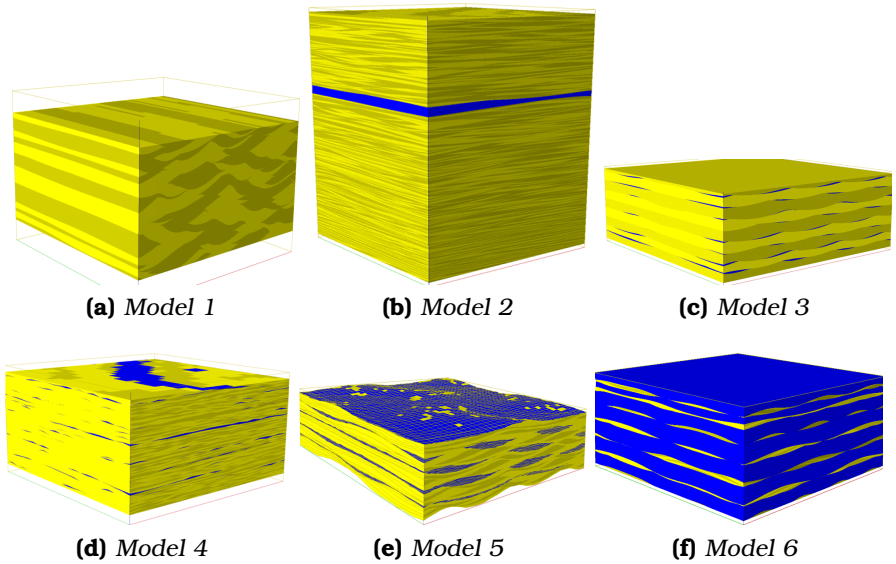

(a) *Model 1* **(b)** *Model 2* **(c)** *Model 3*

(d) *Model 4* **(e)** *Model 5* **(f)** *Model 6*

Figure 24: *6 lithofacies models. Blue color indicates shale, while the light and dark yellow indicates two different sand stones.*

Often sands are very close to isotropy [8] and they are assumed isotropic here. Shales are in general anisotropic to some degree and determining the anisotropy of these has been a problem for many years [6]. In lack of general elasticity data for the shale, this is frequently assumed isotropic in applications. However, there is reason to believe that micro scale heterogeneity in shale causes anisotropy which may have impact on wave velocities. Here shale is assumed TI symmetric. The rock properties chosen are grounded on statistical data on realistic rocks and are given by equations (33) and (35). ρ denotes the densities given in $\mathrm{g/cm^3}$ while the elastic constants are given in GPa (10^9 Pascal). Since the sands are isotropic they have constant P velocities, constant and congruent S wave velocities and hence the V_P/V_S ratio is constant. For $Sand1$ these are

$$\begin{aligned} V_{P_1} &= 2905.3\mathrm{m/s} \\ V_{S_1} &= 1464.9\mathrm{m/s} \\ \left(\frac{V_P}{V_S}\right)_1 &= 1.9833, \end{aligned}$$

for $Sand2$

$$V_{P_2} = 3853.6\text{m/s}$$
$$V_{S_2} = 2177.0\text{m/s}$$
$$\left(\frac{V_P}{V_S}\right)_2 = 1.7701$$

and for $Shale$ these vary with angle between propagation direction and vertical axis (TI symmetry axis). Plots of the wave velocities and V_P/V_S ratios for the three input rock types are shown in figures 25, 26 and 27. For anisotropic materials, the V_P/V_S ratio is defined by $\frac{V_P}{\max(V_{S_1},V_{S_2})}$ since it is the fastest S wave that is recorded in sonic logs and laboratory measurements.

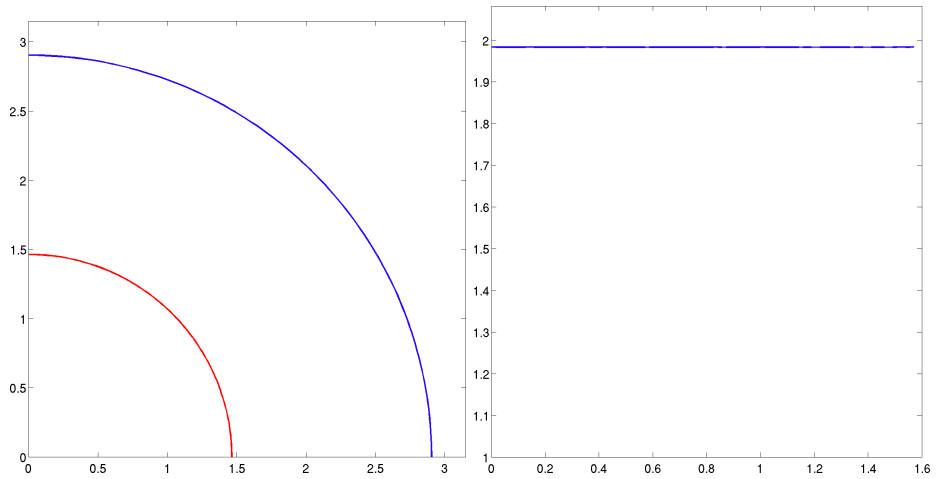

(a) *Blue* $= V_P$, *red* $= V_S$ **(b)** V_P/V_S *versus angle*

Figure 25: *Wave velocities as radius for different propagation directions in (a) and* V_P/V_S *ratio as a function of angle (b) for* $Sand1$. *As one sees there is no angular dependence since the sand is assumed isotropic.*

For model 1, which only consists of sandstone, the resulting wave velocities are shown in figure 28. In figure 28a one sees that the wave velocities lie within the upper and lower bounds indicated by the light blue and pink sectors. This should also be the case since these bounds are valid, i.e. no approximation is done since there are only isotropic components (only sands) in this model. The V_P/V_S ratio shown in figure 28b is nearly a straight line which means that the result is close to isotropic. The Eulidean distance to the

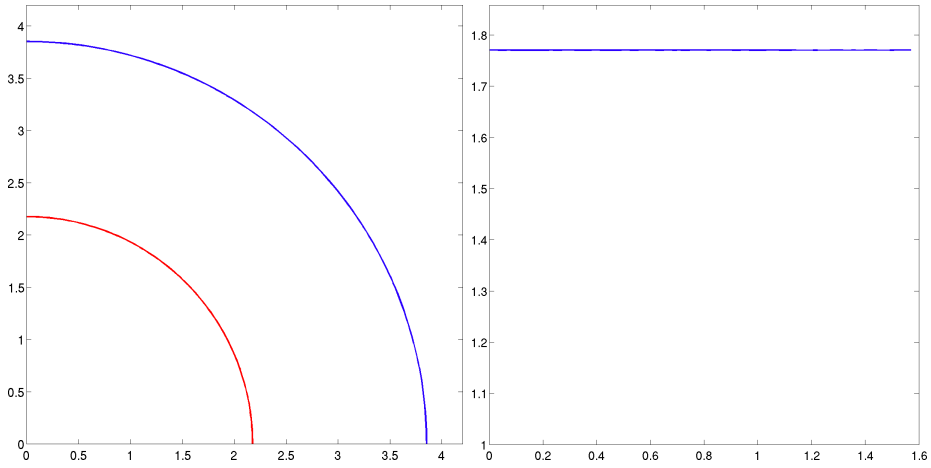

(a) *Blue* $= V_P$*, red* $= V_S$*.* **(b)** V_P/V_S *versus angle*

Figure 26: *Wave velocities as radius for different propagation directions in (a) and* V_P/V_S *ratio as a function of angle (b) for* $Sand2$*. The velocities are independent of angle since the elastic modulus is isotropic.*

isotropic projection is $2.52 \cdot 10^{-2}$ and the velocities for the projection are $V_P = 3.3547$ km/s and $V_S = 1.8095$ km/s. Since the results are close to isotropic and the upper and lower bounds are not too separated, one could discuss whether it is necessary to do time and computer consuming upscaling which take geometry into account, or if a volume weighted average upscaling is good enough.

Model 2, 3 and 4 have more or less the same amount of clay, but have very different geometries. Model 2 have few thick horizontal shale layers with mixed sandstone in-between, model 3 have shale drapes and model 4 has thin shale layers with wholes and sand in between. From the upscaled results for these models shown in figure 29, 30 and 31, one sees that the velocities are very similar in these models and also very similar to the velocities in model 1 which have no shale at all. This indicates that for low shale contents, geological effects are not significant. This is an interesting phenomenon since this is opposite of what is the case for permeability.

Model 5 has about ten times more shale than the previous discussed models, but as seen from figure 32, the result is still very close to isotropy. The Euclidean distance form isotropy is 0.0215. One difference from the above models is that the (estimated) bounds are now wider.

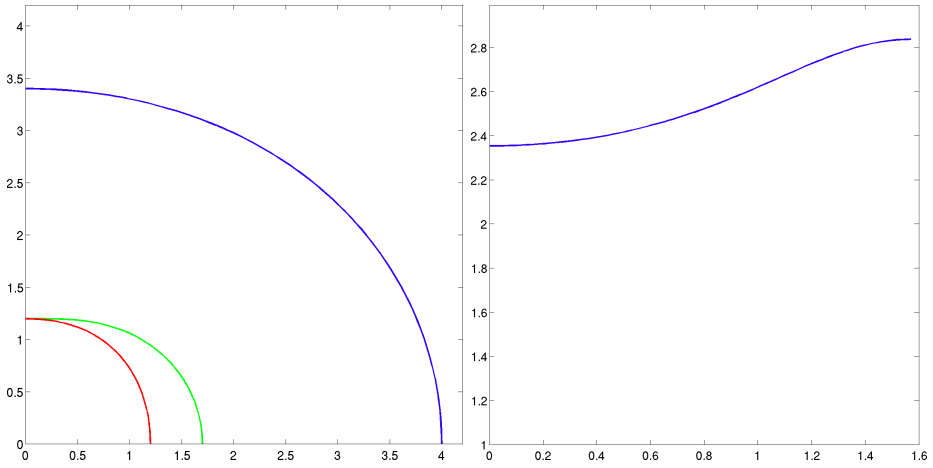

(a) *Blue* $= V_P$*, green* $= V_{S_2}$*, red* $= V_{S_1}$*.* **(b)** V_P/V_S *versus angle*

Figure 27: *Wave velocities as radius for different propagation directions in (a) and* V_P/V_S *ratio as a function of angle between propagation direction and vertical axis (b) for the input shale. Since the shale is assumed anisotropic, there are two* S *waves.*

Figure 33 shows the upscaled results for model 6, which mainly consists of shale. Here one sees a significant anisotropy. The relative Euclidean distance from isotropy for this model is 0.1081, i.e. over 10%, while the same distance from TI symmetry is only 0.0131.

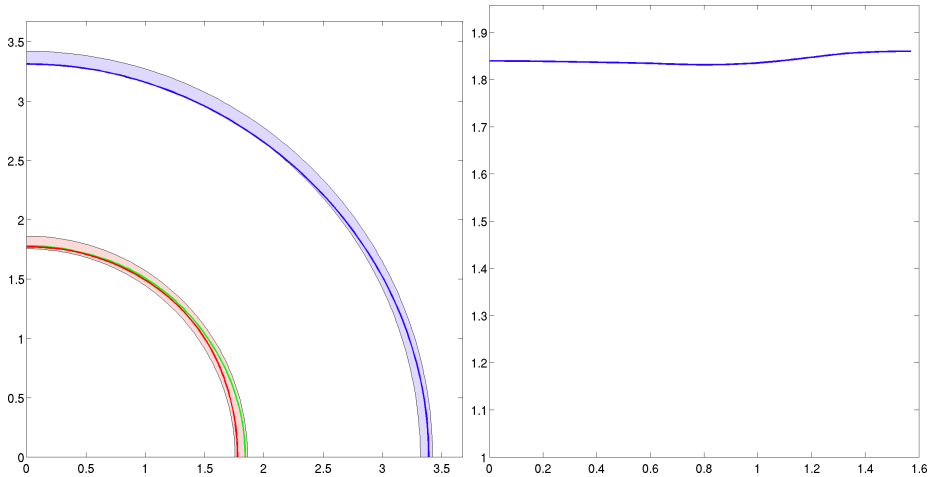

(a) *Wave velocities with upper and lower bounds.*

(b) V_P/V_S *vs. dip angle.*

Figure 28: *Wave velocities (in* $\mathrm{km/s}$*) corresponding to upscaled result for model* 1 *given in table 3. Figure (a) shows the three velocities on top with the corresponding upper and lower bounds for these in the background. Figure (b) is the* V_P/V_S *ratio versus dip angle (angle between propagation direction and vertical axis).*

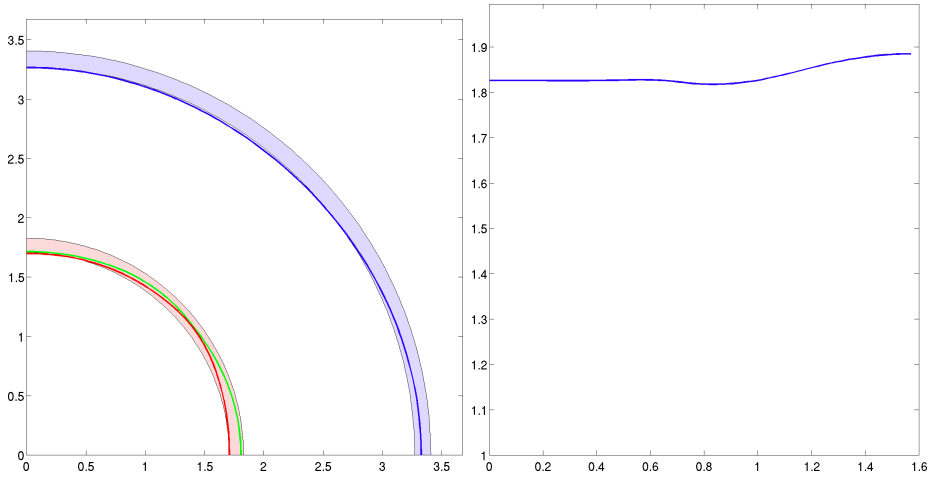

(a) *Wave velocities with upper and lower bounds.*

(b) V_P/V_S *vs. dip angle.*

Figure 29: *Wave velocities (in* $\mathrm{km/s}$*) corresponding to upscaled result for model* 2 *given in table 3. Figure (a) shows the three velocities on top with the corresponding upper and lower bounds for these in the background. Figure (b) is the* V_P/V_S *ratio versus dip angle (angle between propagation direction and vertical axis).*

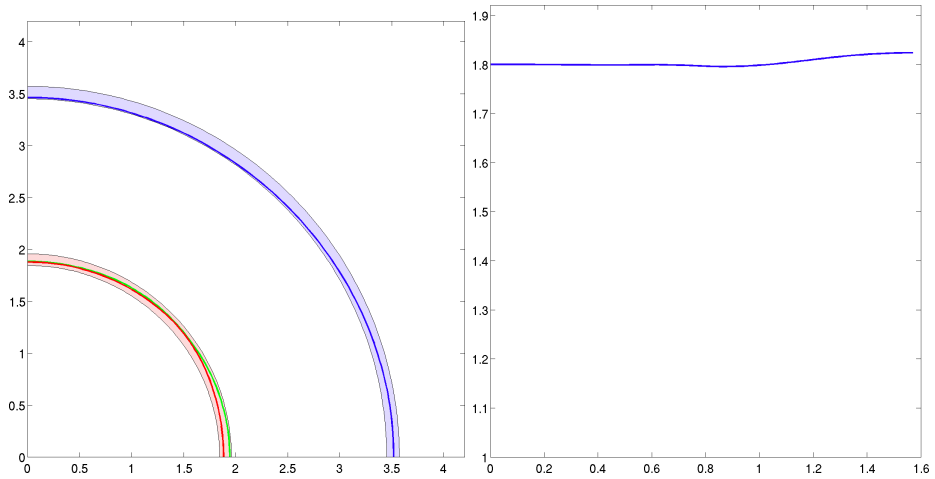

(a) *Wave velocities with upper and lower bounds.*

(b) V_P/V_S *vs. dip angle.*

Figure 30: *Wave velocities (in* $\mathrm{km/s}$*) corresponding to upscaled result for model* 3 *given in table 3. Figure (a) shows the three velocities on top with the corresponding upper and lower bounds for these in the background. Figure (b) is the* V_P/V_S *ratio versus dip angle (angle between propagation direction and vertical axis).*

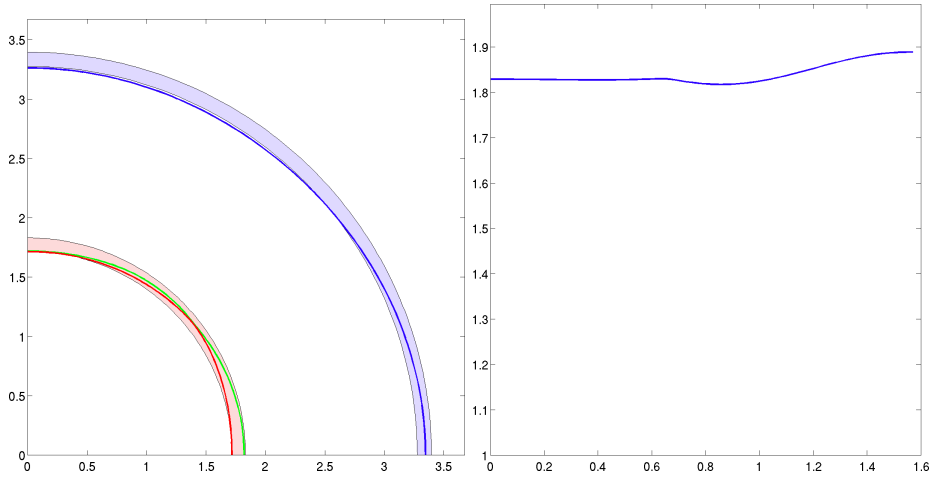

(a) *Wave velocities with upper and lower bounds.*

(b) V_P/V_S *vs. dip angle.*

Figure 31: *Wave velocities (in* $\mathrm{km/s}$*) corresponding to upscaled result for model* 4 *given in table 3. Figure (a) shows the three velocities on top with the corresponding upper and lower bounds for these in the background. Figure (b) is the* V_P/V_S *ratio versus dip angle (angle between propagation direction and vertical axis).*

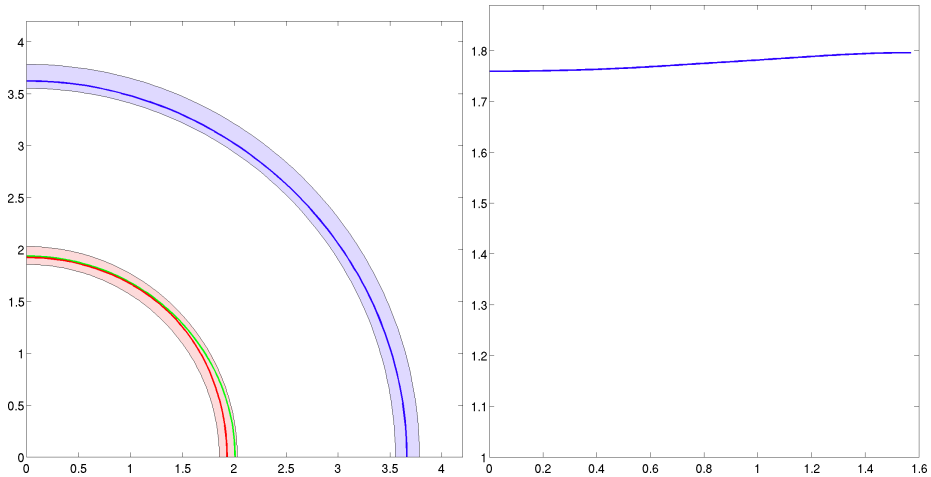

(a) *Wave velocities with upper and lower bounds.*

(b) V_P/V_S *vs. dip angle.*

Figure 32: *Wave velocities (in* $\mathrm{km/s}$*) corresponding to upscaled result for model* 5 *given in table 3. Figure (a) shows the three velocities on top with the corresponding upper and lower bounds for these in the background. Figure (b) is the* V_P/V_S *ratio versus dip angle (angle between propagation direction and vertical axis).*

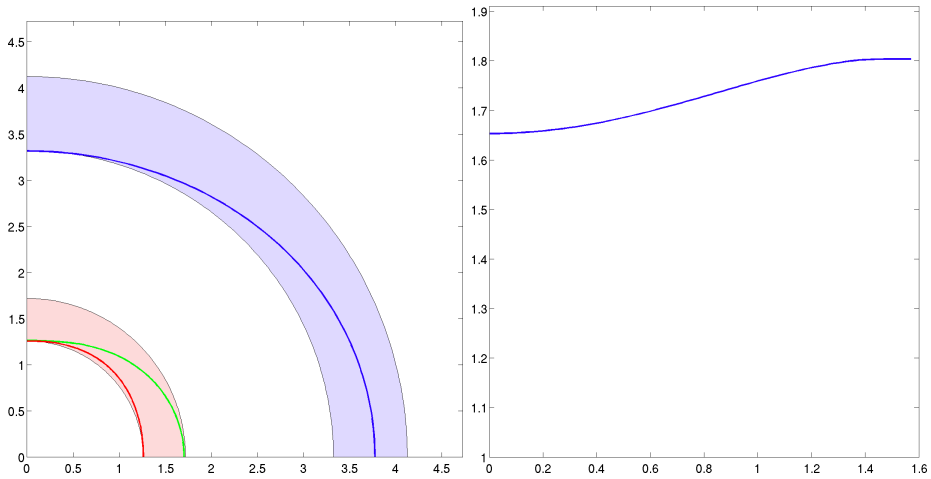

(a) *Wave velocities with upper and lower bounds.*

(b) V_P/V_S *vs. dip angle.*

Figure 33: *Wave velocities (in* $\mathrm{km/s}$*) corresponding to upscaled result for model* 6 *given in table 3. Figure (a) shows the three velocities on top with the corresponding upper and lower bounds for these in the background. Figure (b) is the* V_P/V_S *ratio versus dip angle (angle between propagation direction and vertical axis).*

Chapter 9

Upscaling from lithofacies to channel infill facies

The previous computations have been on models with characteristic lengths from 15 to 35 cm which represent small pieces of a reservoir. Since the method is scale independent, it can also be used on facies models that try to model geology at a larger scale. Here two such models, channel infill facies, are considered and these are shown in figures 34 and 35. Model 34 is an idealized model of a river, while model 35 is more realistic and imitates several rivers that have existed at different times. The cells in these models are at the same scale as the models in chapter 8, thus input in the models here could have origined from a lamina to lithofacies upscaling.

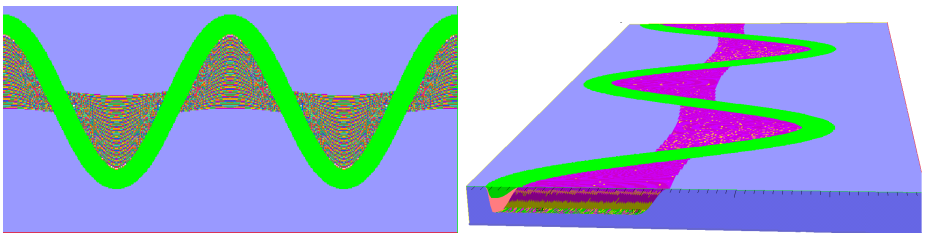

(a) *Horizontal cut* **(b)** *3D model*

Figure 34: *Model* 1 *which models a river channel. The colors represent different rock types, the blue background color representing "background" shale.*

Here, the elasticity and density data for each rock type origin from sonic logs and they are all assumed isotropic (also the "background" shale due to lack of enough data to estimate the anisotropy). There are 7 different rock types in addition to the "background" shale and

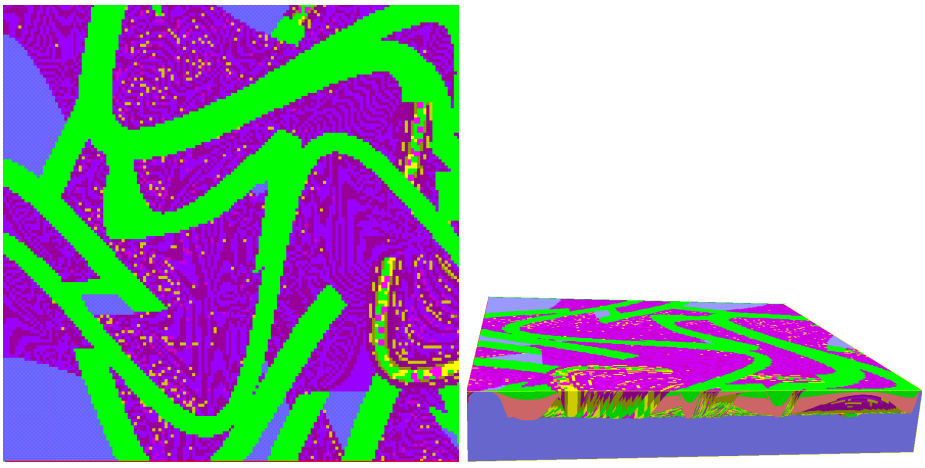

(a) *Horizontal cut* **(b)** *3D model*

Figure 35: *Model* 2*. The colors represent the different rock types where the blue represent "background" shale, i.e. shale that is not part of, but surrounds, the actual reservoir.*

the physical properties for these are given in table 4. Note that the "background" shale is what lies around the structures that defines the actual reservoir and must not be confused with shale and clay deposits in for example the models in figure 24. The upscaled result

Rock type	*Bulk moduli,* K (GPa)	*Shear moduli,* μ (GPa)	*Density,* ρ ($\mathrm{g/cm^3}$)
1	13.96	5.73	2.42
2	18.57	6.38	2.40
3	11.00	8.67	2.42
4	19.97	9.19	2.44
5	16.54	7.61	2.41
6	11.24	6.21	2.29
7	11.97	6.59	2.30
8	13.39	6.16	2.42

Table 4: Elasticity and density data for the different rock types in the two facies models in figures 34 and 35. Rock type 1 is the "background" shale.

for the first model is shown in figure 36. The V_P/V_S ratio as function of angle is very close to constant which means that the upscaled result is very close to isotropy, again confirmed by the isotropic

projection and the distance from this to the original tensor,

$$\frac{\|\mathbb{C} - \mathbb{C}_{iso}\|_F}{\|\mathbb{C}\|_F} = 0.0020.$$

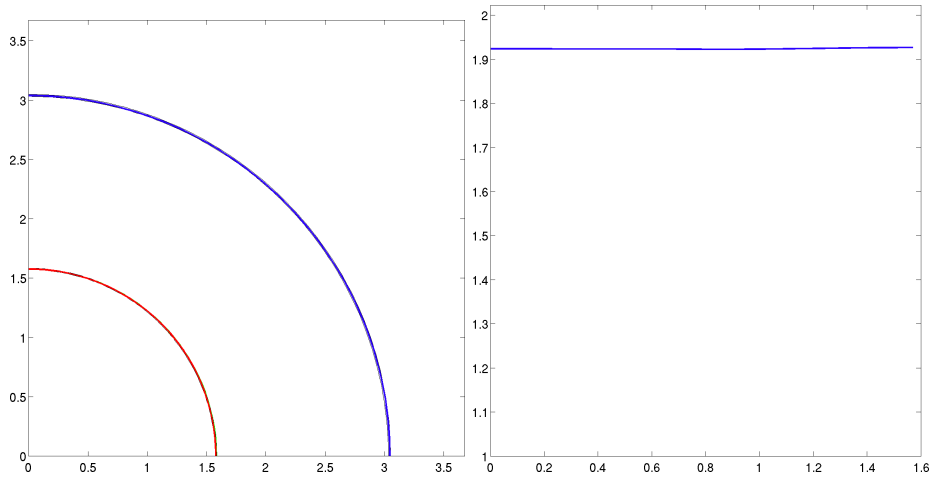

(a) *Wave velocities with upper and lower bounds.*

(b) V_P/V_S *vs. dip angle.*

Figure 36: *Wave velocities with upper and lower bounds in (a) and* V_P/V_S *as function of angle in (b) for the model in figure 34. As one sees, by for example comparing with figure 11b, the bounds are so close that they are almost invisible.*

From the velocities with the corresponding bounds in figure 36a one also sees that the Voigt and Reuss bounds are very close together, indicating that volume weighted upscaling is sufficient and geological modelling of elastic properties is unnecessary in this case. Since all rock types are assumed isotropic, the bounds are exact in this case (see section 3.1.1). For the second model in figure 35, the resulting velocities and V_P/V_S are shown in figure 37. Here the V_P/V_S has slightly more variation than for the first model, but still very close to constant. The Voigt and Reuss bounds are a little, but almost invisibly, more separated than for the other model. The discrepancy that this represent in for example V_P velocity is

$$V_{P_{\text{Voigt}}} - V_{P_{\text{Reuss}}} = 0.0361 \text{ km/sec}$$

which in most practical applications will be much smaller than the uncertainty in for example seismic data.

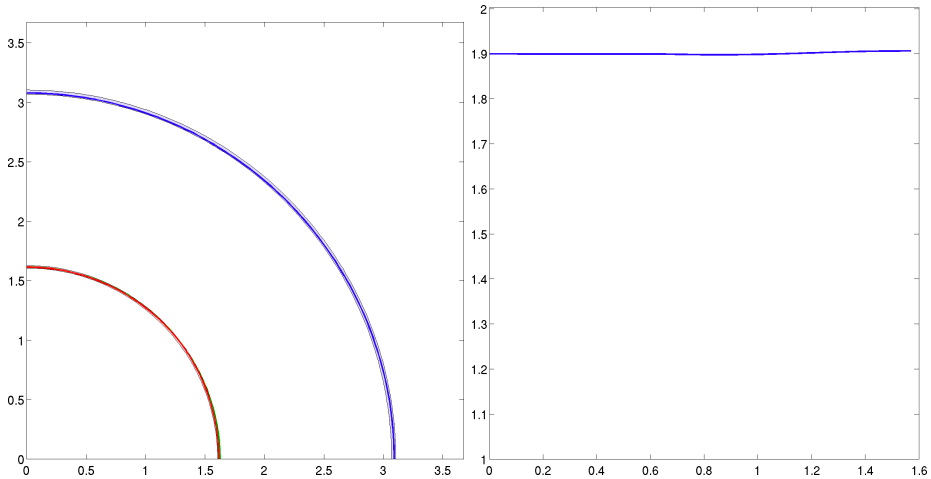

(a) *Wave velocities with upper and lower bounds.*

(b) V_P/V_S *vs. dip angle.*

Figure 37: *Wave velocities with upper and lower bounds in (a) and* V_P/V_S *as funciton of angle in (b) for the model in figure 35.*

The models considered here are made for fluid flow simulations and from the elasticity results obtained here one may question whether modelling as fine as this is necessary for elasticity. From the input data, which origin from sonic logs and are given in table 4, one sees that the contrasts between the different rock types are very small. In addition the background shale is modelled isotropic which is probably incorrect. By getting input to these models from lamina to lithofacies upscalings instead, one may capture the lithofacies scale anisotropy and maybe also get larger contrasts between the different rocks. From the previous chapters, there is reason to believe that the cell level anisotropy will have the most significant impact of these two.

Chapter 10

Elasticity upscaling in 4D seismic

In order to model seismic velocities as function on fluid saturations, one should preferably start at the smallest scale on which geological features have effects. A future goal in reservoir simulation could then be a "bottom-up" approach where one has information about elasticity as function of fluid saturations at the smallest scale at which modelling currently seems possible and then upscale this information up to seismic resolution scale. Further, the upscaled elasticity as function of fluid saturations could be used to compute wave velocities as function of fluid saturations and compare these to seismic data in order to determine the amount of hydrocarbon reserves.

Since all the data needed to do this are not currently available, one step in this procedure, going from lamina to lithofacies scale, is demonstrated here for two phases, water and oil. The input elastic parameters at lamina scale are therefore synthetic but one could pretend that these origin from some upscaling or modelling technique from for example pore scale. The purpose of this chapter is to test a possible workflow for one single step in a forward seismic modelling procedure.

For each cell, the upscaling method only does not require information about the fluid compound in the cell, only a stiffness tensor which should represent the effective stiffness given all other physical conditions. If the model is populated with elasticity data for a certain fluid compound, the result is valid under the same conditions. Thus to upscale effective elasticity as function of fluid saturations, one needs stiffness tensors as function of fluid saturation for

each cell. One could for example have effective elastic parameters as a function of fluid saturations directly, coming from a previous upscaling step, or one could model the rock and the fluid filled pore space separately and use a model that combines the properties of these two to find the effective elasticity for the rock and fluid together. The latter is used to produce the input data used in this case.

The rock is assumed to have certain elastic properties that are independent of fluid saturations. K_{fr} is the bulk modulus of the rock structure when the pores are empty (or approximately air filled), K_{s} is the bulk modulus of the solid rock, i.e. the bulk modulus the rock structure would have if it had no pores, μ_{fr} is the shear modulus of the empty rock, ϕ is the porosity, i.e. the volume fraction of the rock structure that is not solid rock and ρ_{s} is the density of the solid rock.

The effective properties of the fluid varies with the proportion of the different fluids. If the fluid consists of pure oil, the elastic properties are equal to those of oil et.c. The effective bulk modulus of the fluid, K_{fl} is dependent on at which scale the different fluids are mixed. Under the infinite wave length assumption, the fluid can be seen as completely mixed (no patchiness) and the effective modulus in this case is given by the Reuss average [9]

$$K_{\text{fl}} = \frac{1}{\sum_i \frac{S_i}{K_i}}. \tag{37}$$

where K_i and S_i are the bulk modulus and saturation of fluid i. Physically this denote that the fluids are in a suspension and each fluid particle will experience the same stress. For relatively non-viscous fluids, the shear modulus is zero as shear waves cannot travel through such fluids. The effective density is trivial to compute and is given by

$$\rho_{\text{fl}} = \sum_i \rho_i S_i \tag{38}$$

where ρ_i is the density of fluid i.

Given the fluid saturations, the effective elastic moudlus of each cell is computed by utilizing the Biot–Gassmanns relations,

$$\begin{aligned} K_{\text{eff}} &= K_{\text{fr}} + \frac{\left(1 - \frac{K_{\text{fr}}}{K_{\text{s}}}\right)^2}{\frac{\phi}{K_{\text{fl}}} + \frac{1-\phi}{K_{\text{s}}} - \frac{K_{\text{fr}}}{K_{\text{s}}^2}} \\ \mu_{\text{eff}} &= \mu_{\text{fr}}. \end{aligned} \tag{39}$$

As one can see, the shear modulus is constant for all saturations, i.e. not dependent on fluid saturations which is reasonable since the fluids have zero shear modulus and do not contribute to make the effective medium more torsion resistant.

Combining equations (39) and (37) yields the following relationship between effective bulk modulus and water saturation, S_w,

$$K_{\text{eff}}(S_w) = K_{\text{fr}} + \frac{\left(1 - \frac{K_{\text{fr}}}{K_{\text{s}}}\right)^2}{\phi\left(\frac{S_w}{K_w} + \frac{1-S_w}{K_o}\right) + \frac{1-\phi}{K_{\text{s}}} - \frac{K_{\text{fr}}}{K_{\text{s}}^2}} \tag{40}$$

where K_w and K_o are the bulk moduli for water and oil and these are the only fluid phases present. Note that there exist more complex relationships for effective bulk modulus as function of saturations. Here however this relationship only serve as a function to generate synthetic input and not as a model to describe the actual conditions.

The fluid distributions in a reservoir are determined by several factors. In a steady-state situation, i.e. when the physical parameters are not time dependent, there are a finite set of forces acting on the fluids to keep the saturations constant. In many fluid simulations models, such as the black-oil model, three such forces are considered, capillary forces, gravitational forces and viscous forces. The balance between these is sensible to scale and other reservoir properties and different balances give rise to different steady-state methods to determine the fluid distributions [1].

In this example a capillary equilibrium method is used, i.e. the capillary forces are assumed to dominate the viscous and gravitational forces. Now to find upscaled elasticity, one starts by choosing a capillary pressure, p_C, which is constant in all cells due to the capillary equilibrium assumption. For each rock type, one needs a relation between fluid saturations and pressure in order to determine the fluid saturations in each cell. This is obtained by providing laboratory data for a Leverett J-function as function of water saturation to each rock type. These lab data are for real rocks, but used here only as example input data. The Leverett J-function is a scaling of saturation-dependent capillary pressure. Now with the saturations in each cell, the elastic parameters can be computed by Biot–Gassmanns equations (39), (40). A more detailed description of this procedure is presented in [5].

The upscaling as function of water saturation was done on the

model shown in figure 24e with sand and shale properties

$$\begin{aligned} K_{fr_{Sand}} &= 5.14 \text{ GPa} \quad K_{fr_{Shale}} = 10.0 \text{ GPa} \\ K_{s_{Sand}} &= 26.5 \text{ GPa} \quad K_{s_{Shale}} = 11.31 \text{ GPa} \\ \mu_{fr_{Sand}} &= 3.15 \text{ GPa} \quad \mu_{fr_{Shale}} = 2.3 \text{ GPa} \\ \phi_{sand} &= 0.3 \quad \phi_{Shale} = 0.05 \end{aligned}$$

where ϕ is the porosity. The elastic properties for the fluids are set to

$$\begin{aligned} K_w &= 2.25 \text{ GPa} \quad K_o = 1 \text{ GPa} \\ \mu_w &= 0 \text{ GPa} \quad \mu_o = 0 \text{ GPa} \end{aligned}$$

for water and oil. Note that the shear moduli are set to zero, which is the valid for non viscous fluids. The densities of the different materials in question are

$$\begin{aligned} \rho_s &= 2.3 \text{ g/cm}^3 \\ \rho_w &= 1.0 \text{ g/cm}^3 \\ \rho_o &= 0.9 \text{ g/cm}^3 \end{aligned}$$

for the solid rock, water and oil respectively. Thus upscaled density become

$$\hat{\rho} = \phi(S_w\rho_w + (1 - S_w)\rho_o) + (1 - \phi)\rho_s$$

where ϕ is the porosity and S_w is the water saturation.

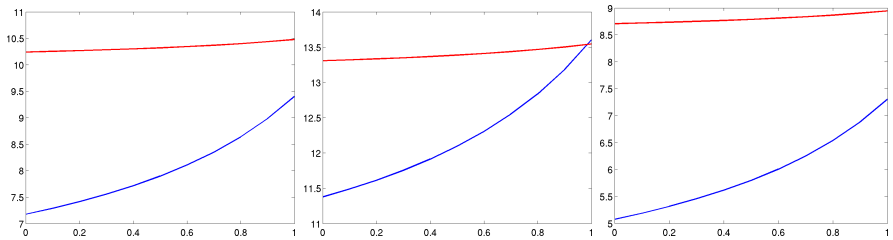

(a) $K_{\text{eff}(S_w)}$ **(b)** $(\lambda + 2\mu)(S_w)$ **(c)** $\lambda(S_w)$

Figure 38: *Elasticity as function of water saturation. The blue graphs are for sand, while the red graphs are for shale. (a) is the effective bulk modulus* K_{eff} *while (b) and (c) are* $K + \frac{4}{3}\mu$ *and* $K - \frac{2}{3}\mu$*, i.e. the components corresponding to* P *wave modulus* $\lambda + 2\mu$ *and* λ *in equation* (12) *on page 12.*

Effective input bulk modulus K as function of water saturation is shown in figure 38a where the red graph corresponds to shale and the blue graph corresponds to sand stone. Figure 38 also shows the components corresponding to $[C_{ii}]_{i=1}^{3}$ and $[C_{ij}]_{\substack{i,j=1 \\ i \neq j}}^{3}$ in the stiffness matrix for comparison with the upscaled result.

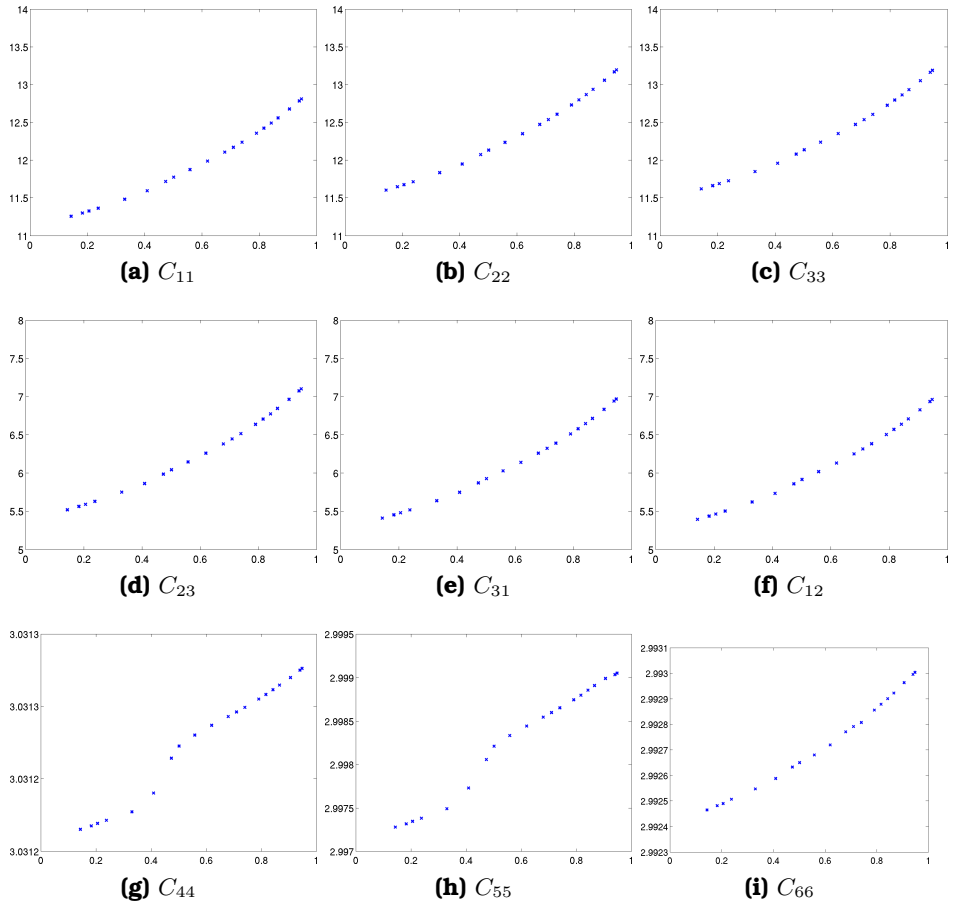

(a) C_{11} **(b)** C_{22} **(c)** C_{33}

(d) C_{23} **(e)** C_{31} **(f)** C_{12}

(g) C_{44} **(h)** C_{55} **(i)** C_{66}

Figure 39: *The coefficients of the elastic modulus with magnitude greater than* 10^{-2} *as function of water saturation. The components are related to those in the isotropic elastic modulus in* (12) *on page 12 where (a) to (c) corresponds to* $\lambda + 2\mu$*, (d) to (f) corresponds to* λ *and (d) to (f) corresponds to* μ*. The input values for* $\lambda + 2\mu$ *and* λ *are shown in figure 38b and 38c. The variation in (g) to (i) are probably due to numerical errors.*

Figure 39 shows the elasticity tensor components that are larger than 10^{-2} in magnitude, as function of water saturation. One can see that the components which depend on the bulk modulus, shown

in figures 39a to 39f, vary with water saturation, while those that only dependent of shear modulus, shown in figures 39g to 39i, are almost constant. Figures 39a to 39c represent $\lambda + 2\mu$ in (12) on page 12 and the shape and magnitude of these are obviously closer to those for sand stone than for shale in figure 38b. The same yields for the off diagonals in the upper 3×3 part of the elastic moduli which correspond to λ, i.e. the shape and magnitude of the components in figures 39d to 39f are more similar to the sand stone input than the shale input in figure 38c. For the components corresponding to the shear modulus in figures 39g to 39i, it seems like these vary with water saturation. However, the magnitudes of these variations are smaller than the upscaling error found in section 4.2 and they are therefore attributed to numerical errors.

The components of the effective elastic modulus as functions of water saturation are a lot closer to the input for sand stone than to the input for shale. This is reasonable since the model consists of approximately 90% sand stone and 10% shale, moreover it shows that fluid saturations have an significant impact on the upscaled result. It is reasonable to believe that if the input shear moduli were also dependant on fluid saturations, the effective shear parameters would also be fluid dependant.

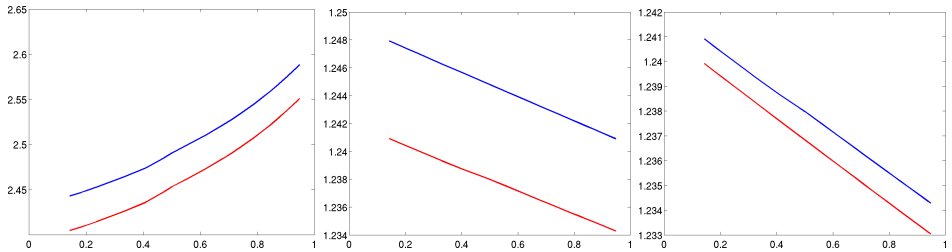

(a) V_P **(b)** V_{S_1} **(c)** V_{S_2}

Figure 40: *Velocities as function of water saturation for the model in figure 24e. The blue graphs is for horizontal propagation while the red corresponds to vertical propagation.*

From equation (13), one sees that the velocities decrease for increasing density and increase for increasing stiffness. Since the shear modulus is independent of water saturation and the density increases with water saturation, the S wave velocities should decrease with increased water amount. From figures 40b and 40c, which show the S wave velocities in the horizontal direction (blue graph) and vertical direction (red graph), one sees that this is correct. Note however that this is because the input shear moduli at

cell scale are assumed independent of water saturation. This may not always be the case.

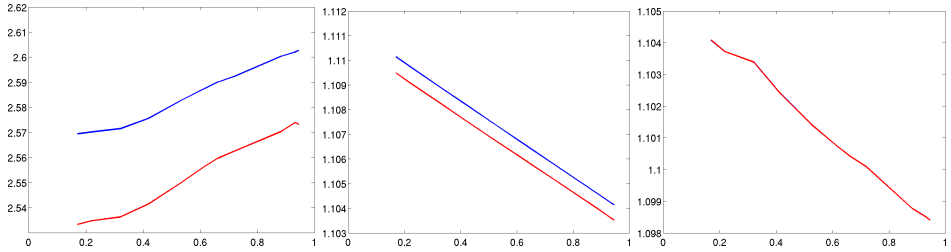

(a) V_P **(b)** V_{S_1} **(c)** V_{S_2}

Figure 41: *Velocities as function of water saturation for the model in figure 24f. The blue graphs is for horizontal propagation while the red corresponds to vertical propagation. In (c) the wave velocities are approximately equal in the horizontal and vertical direction.*

V_P as function of water saturation, which is shown in figure 40a, increase with water saturation. This means that the increase in bulk modulus is stronger than the increase in density when the pore space goes from oil filled to water filled.

The model has some kind of imperfect layering (see figure 24e) which can be approximated by perfect layering (chapter 7). One saw that for perfect layering, the velocity trends corresponded to permeability (chapter 7) which is largest along the layers. Here one sees that in all cases, the velocities are higher in the horizontal direction, i.e. along the layers, than in the vertical (across the layers) for all saturations.

Since the model considered here contains a lot more sand stone than shale, the upscaling is also run on the model in figure 24f which contain about 84% shale and 16% sand stone to see if the saturation effects have an impact here. The rock data used is the same as above. The effective velocities for this model in shown in 41 and as one can see that fluid saturation variations is much less significant in this case. While the horizontal wave velocity for the model in figure 24e spans from about 2.44 to 2.59 km/s, it spans from 2.57 to 2.60 km/s for model 24f.

In permeability upscaling, one can distinguish between single phase effects and multiphase effects, i.e. one can see geometrical effects on the anisotropy of the upscaled relative permeability which is not visible on the single phase permeability [5]. For the P wave velocity in figure 40a, one sees that the differences between horizontal and

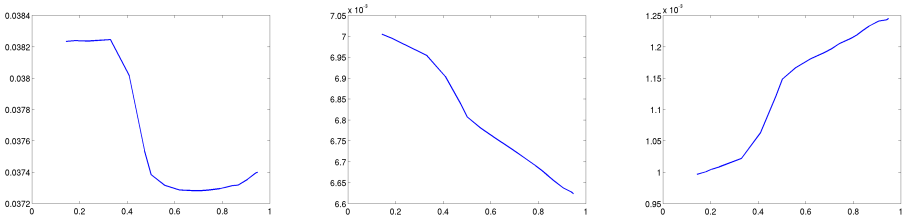

(a) $V_{P_{\text{Horizontal}}} - V_{P_{\text{Vertical}}}$ **(b)** $V_{S_1{\text{Horizontal}}} - V_{S_1{\text{Vertical}}}$ **(c)** $V_{S_2{\text{Horizontal}}} - V_2 S_{\text{Vertical}}$

Figure 42: *Differences between horizontal and vertical wave velocities.*

vertical wave propagation seem to be constant as function of water saturation. These differences, i.e. horizontal wave velocity minus vertical wave velocity, are shown in figure 42. Because one knows that the shear moduli are constant as functions of saturations in this case and the magnitudes of the differences for the S waves are very small, these are not investigated further here.

The difference between horizontal and vertical velocity for the P wave is bigger than those for the S waves in magnitude and it has, yet not monotonic, some similarities to relative permeability as function of water saturation (see e.g. [5]). To see if this really is a trend, difference in P wave velocity as function of water saturation is computed for the geological models shown in figure 17. These are shown in figure 43 and one sees that for all sand stone fractions, the difference between horizontal and vertical P wave velocity, i.e. the anisotropy, is decreasing for increasing water saturation. As one can see on the input values in figure 38, shale is stiffer than the sand stone for all water saturations. Since water is stiffer than oil, the sand stone, which is the most porous rock and therefore most sensitive to fluid saturation variations, gets stiffer with increased water saturation and the contrast between the sand stone and shale decrease. This contrast decrease results in a less anisotropic effective stiffness modulus, thus the anisotropy decrease as function of water saturation.

In addition to the fluid saturation dependence, figure 43 also show that the anisotropy is dependent on sand and shale fractions. Figure 44 shows the difference as function of sand fraction for water saturation equal to 0.1, 0.5 and 0.9. As the plot shows, the rock type fractions are more important than the saturation variations. When analyzing figure 42, 43 and 44, one should keep in mind that the magnitude of the velocity differences are small (for exam-

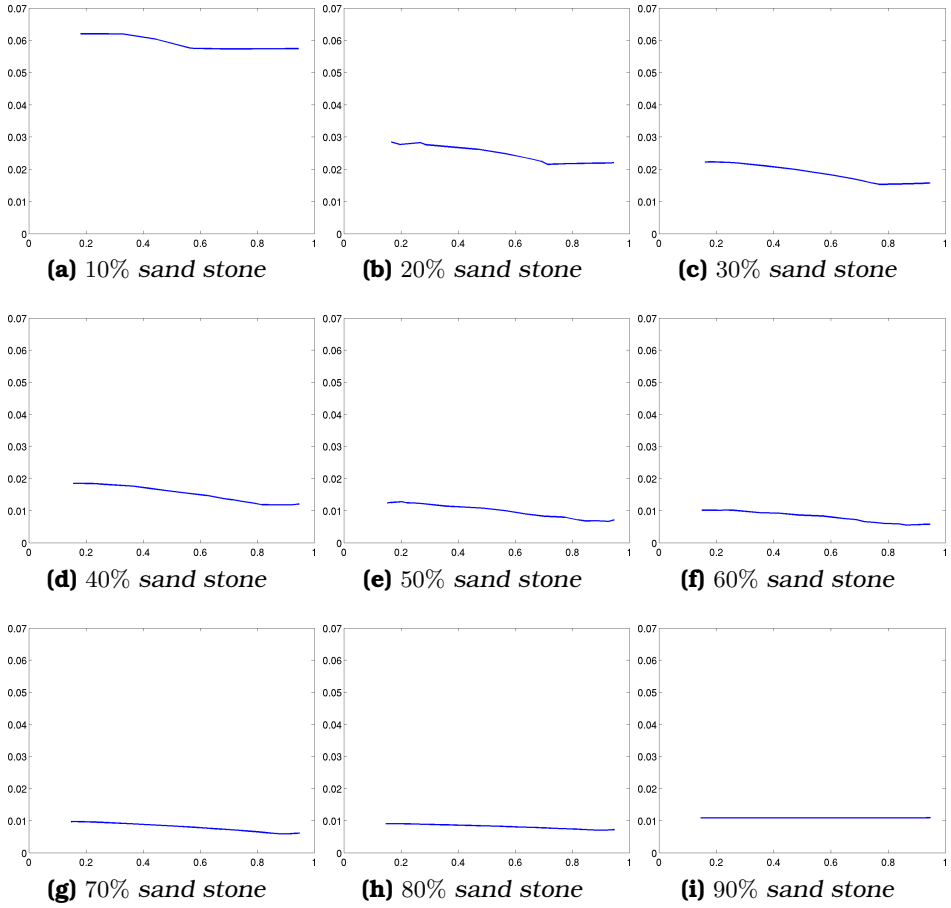

(a) 10% *sand stone* **(b)** 20% *sand stone* **(c)** 30% *sand stone*

(d) 40% *sand stone* **(e)** 50% *sand stone* **(f)** 60% *sand stone*

(g) 70% *sand stone* **(h)** 80% *sand stone* **(i)** 90% *sand stone*

Figure 43: *Differences between horizontal and vertical P wave velocity for the geological models in figure 17.*

ple compared to the errors found in chapter 4) and may therefore be strongly influenced by numerical errors. Therefore, these should only be used to look for trends, not to extract numeric values.

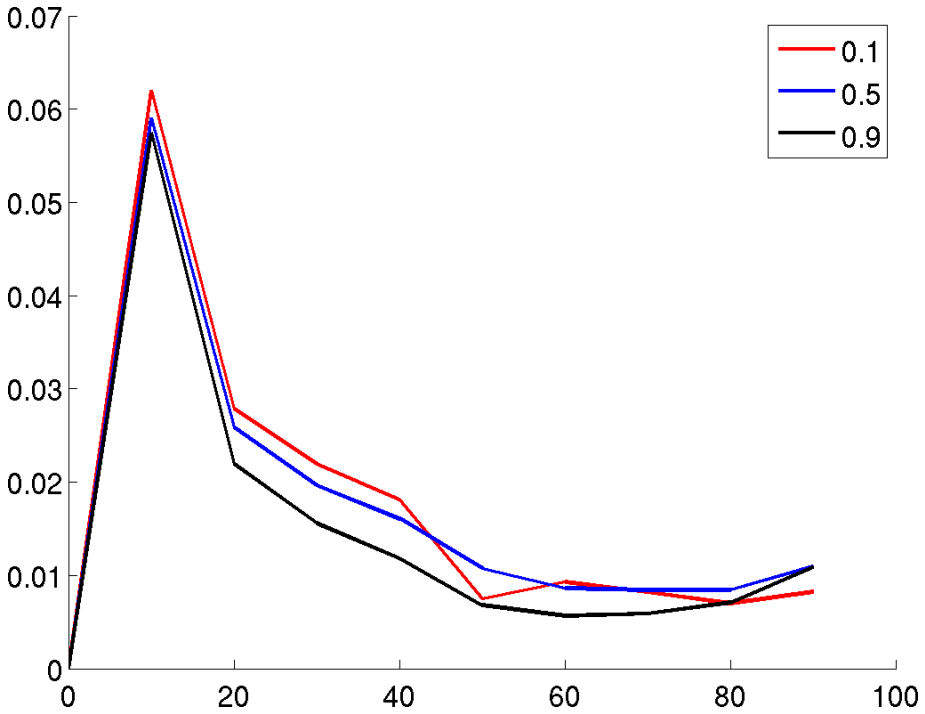

Figure 44: *Difference in horizontal and vertical P wave velocity as function of sand fraction for water saturation equal to 0.1 (red graph), 0.5 (blue graph) and 0.9 (black graph).*

Chapter 11

Concluding remarks

The composition of the different rock types has an influence on the effective elastic moduli, i.e. the results depend on the geometry of the rock. Volume weighted averages, which constitute the upscaling methods for elasticity today, do not account for these effects as they do not incorporate all information about how the different rock types are arranged relatively to each other. The geometrical effects, which here represents different geological features, show similar trends on elasticity as they do on permeability, but the magnitude of the deflections from volume averaging are much smaller for elasticity than for permeability upscaling. In some cases the geometric effects are seemingly very small.

The contrast between the different rock types determine the magnitude of the deflections one sees between simple volume averaging methods and the general geometry upscaling method used here. As elastic parameters are commonly used in seismics, it is natural to evaluate the findings by comparing the results to what is visible in seismics. A typical contrast seen in seismics, is between sandstones and shales. For water saturated sandstones the P wave velocity can be around $\sim 4\ \mathrm{km/s}$, while for shale it can be $\sim 3.5\ \mathrm{km/s}$, thus one can expect that contrasts of $\sim 0.5\ \mathrm{km/s}$ are visible on seismics.

In chapter 7.1 the effective velocities differ up to $\sim 0.1\ \mathrm{km/s}$ between three compositions with different geometries when all rock types are assumed isotropic. When the shale in the same compositions was assumed anisotropic, the velocity deviations between the estimated bounds go up to $\sim 0.3\ \mathrm{km/s}$. (In theory there exists a model with the same volumetric amounts of rocks that reaches these bounds. To obtain this geometry the different rock types may have to be rearranged and rotated.) These deviations are of the same order as

the difference in wave velocity between sandstone and shale, thus it is probable that the influence due to geometry is visible on seismics. Also, these differences being of the same order as the velocity contrast between sandstones and shales support the significance of geometrical impact on the effective elasticity.

In the upscaling from lamina to lithofacies in chapter 8, where the input parameters are based on actual measurements but chosen deliberately with a fairly high contrast, the fluctuations from volume averaging are of the same order as the velocity contrast between sandstone and shale and thus has an impact on seismic. From lithofacies scale to channel infill scale in chapter 9 however, where the input comes from logs, the difference from volume averaging is barely visible in the velocity plots. Even though this indicates that geometry is not important for the effective elastic parameters at this scale, one should notice that the models used here are built for fluid flow simulations and dominated by background shale. Therefore geometrical effects are not to be discounted at this scale despite of the results shown here.

For the lithofacies scale the geometrical effects seem to be overshadowed by other effects for example effects due to modelling the rock isotropic instead of anisotropic at cell scale. The input elasticity data on cell level are very uncertain, especially on anisotropic rock types. The upscaling result is highly dependent on the anisotropy within each cell, i.e. the resulting anisotropy when the shale is assumed anisotropic is completely different from when it is assumed isotropic. This result should encourage more research on getting accurate elastic input of the different rock types, both when it comes to magnitude of the different parameters and on anisotropy.

The input rock types have here been assumed either isotropic or transversely anisotropic with vertical symmetry axis and the results in these two cases differ significantly. Other anisotropy symmetries representing different rock types with varying orientations should therefore be investigated as these may show other effects. A scenario one could imagine is local compressions of the earth's upper crust causing originally horizontal layers to merge together and become tilted. If these layers are for example transversely isotropic with symmetry axis perpendicular to the layer, this would yield non vertical symmetry axes with different orientations for each layer. Thus geometry, which captures the orientation of each layer, would perhaps have a profound effect in this case.

When upscaling elasticity for different fluid saturations in chapter 10, it seems like the volumetric amounts of the different rock

types play a more important role than the fluid saturations. However, given a specific model with a relatively large fraction of porous rocks, the wave velocity has a significant dependence on fluid saturations. To get a consistent bottom-up approach for use in 4D seismic, one should start modelling elasticity (preferably as function of fluid saturations), at the smallest modelling scale and bring these data up to seismic scale. Thus research and modelling at pore scale, which is currently the smallest modelling scale in this context, should be prioritized.

In all applications of the general geometry upscaling method, the end user must carefully assess the uncertainties, and use this information when evaluating the upscaled results. Even though some of the geometrical effects seen here is large enough to influence seismic results, these seem to be small compared to the differences when the elasticity is modelled differently at cell level. Geometry is thus to be regarded as a second order effect.

Up until now, the tools available to upscale elastic moduli have been methods which take only limited or no geological information into consideration. Examples of such are Voigt, Reuss, Backus, Hashin–Shtrikman and others. In the future, geology will be modelled finer and finer, and an upscaling tool which also considers geology is a must-have tool in workflows modelling rock physics in a bottom-up approach. The value in the general geometry upscaling method lies in being able to tell precisely when geology is important, and also being able to handle anisotropic input.

Bibliography

[1] Jørg E. Aarnes, Vegard Kippe, Knut-Andreas Lie, and Alf Birger Rustad. *Geometric Modelling, Numerical Simulation, and Optimization: Applied Mathematics at SINTEF*, chapter Modelling of Multiscale Structures in Flow Simulations for Petroleum Reservoirs. Springer-Verlag, 2007.

[2] B.A. Auld. *Acoustic fields and waves in solids*. Krieger Publishing Company, 1990.

[3] J. F. W. Bishop and R. Hill. A theoretical derivation of the plastic properties of a polycrystalline center-faced metal. *Philosophical Magazine*, 1951.

[4] E.J. Borowski and J.M. Borwein. *Collins reference dictionary of mathematics*.

[5] Kari Børset. Reconsiling Scales in Reservoir Modelling. Norwegian University of Science and Technology, 2007.

[6] D.N. Dewhurst, A.F. Siggins, U. Kuila, M.B. Clennell, M.D. Raven, and H.M. Nordgard-Bolas. Elastic, Geomechanical and Petrophysical Properties of Shales. 2008.

[7] R. Hill. The elastic behavior of a crystalline aggregate. *Proceedings of the Physical Society A*, 65:349–354, may 1952.

[8] Luc T. Ikelle and Lasse Amundsen. *Introduction to petroleum seismology*. Society of Exploration Geophysics, Tulsa, Oklahoma, USA, 2005.

[9] Gary Mavko, Tapan Mukerji, and Jack Dvorkin. *The rock physics handbook*. Canbridge University Press, 1998.

[10] Maher Moakher and Andrew N. Norris. The closest elastic tensor of arbitrary symmetry to an elasticity tensor of lower symmetry. *Not published yet*, 2008.

[11] Wikipedia: Plate tectonics. `http://en.wikipedia.org/w/index.php?title=Plate_tectonics&oldid=2092544%99`.

[12] Ivar B. Ramberg, Inge Bryhni, and Arvid Nøttvedt, editors. *Landet blir til, Norges Geologi*. Norsk Geologisk Forening, 2007.

[13] Wikipedia: Stress. `http://en.wikipedia.org/w/index.php?title=Stress_%28physics%29&oldid=18%2169993`.

[14] Wikipedia: Voigt notation. `http://en.wikipedia.org/w/index.php?title=Voigt_notation&oldid=18744766%3`.

[15] Wouter Zijl, Max A. N. Hendriks, and C. Marcel P. Hart. Numerical Homogenization of the Rigidity Tensor in Hooke's Law Using the Node-Based Finite Element Method. *Mathematical Geology*, 34, 2002.